

**FOCUSED ELECTRON BEAM INDUCED PROCESSING (FEBIP) IN
AMMONIA-BASED LIQUID FILMS**

A Dissertation
Presented to
The Academic Faculty

by

Auwais Ahmed

In Partial Fulfillment
of the Requirements for the Degree
DOCTOR OF PHILOSOPHY in the
GEORGE W. WOODRUFF SCHOOL OF MECHANICAL ENGINEERING

Georgia Institute of Technology
December 2025

COPYRIGHT © 2025 BY AUWAIS AHMED

FOCUSED ELECTRON BEAM INDUCED PROCESSING (FEBIP) IN AMMONIA-BASED LIQUID FILMS

Approved by:

Dr. Andrei G. Fedorov, Advisor
George W. Woodruff School of Mechanical
Engineering
Georgia Institute of Technology

Dr. Faisal Alamgir
School of Materials Science and
Engineering
Georgia Institute of Technology

Dr. Matthew McDowell
George W. Woodruff School of
Mechanical Engineering and the School of
Materials Science and Engineering
Georgia Institute of Technology

Dr. Ryan Lively
*School of Chemical and Biomolecular
Engineering*
Georgia Institute of Technology

Dr. Sourabh Saha
George W. Woodruff School of Mechanical
Engineering
Georgia Institute of Technology

Dr. Frances M. Ross
Department of Materials Science and
Engineering
Massachusetts Institute of Technology

Date Approved: [July 31, 2025]

To my family

Whose love, courage, and sacrifice allowed me to begin, continue, and complete this
journey

ACKNOWLEDGEMENTS

I want to thank my PhD advisor, Prof. Andrei G. Fedorov, for his support throughout this journey. I have been lucky to work with someone so kind, smart, compassionate, and fundamentally good-hearted during my PhD. I also extend my gratitude to Peter Kottke for his kindness and humanity. My weekly meetings with both were intellectually stimulating experiences I will treasure for the rest of my life. I owe thanks to my lab mates, past and present, whose camaraderie and support proved invaluable. I am also grateful to my PhD committee for their generous time and guidance.

I acknowledge the Fulbright Fellowship for enabling me to embark on this journey; without the opportunity they provided, this endeavor would not have been possible. I also thank the U.S. Department of Energy, whose grant supported my research and discoveries.

I am thankful to the city of Atlanta, whose vibrant community and intellectual nourishment enriched this journey. I am equally indebted to the United States for fostering an environment of innovation and discovery, which has transformed me profoundly since the start of this path.

I thank the administration and maintenance staff of the Mechanical Engineering Department at Georgia Tech for ensuring the facilities we researchers depend on remained operational. I also appreciate the staff of the Materials Characterization Facility (MCF) at Georgia Tech, whose expertise advanced my research.

Finally, I thank my family. My wife, whose unwavering support and sacrifices made this journey possible; my children, whose understanding and good humor gave me strength; and my parents, who nurtured my curiosity and shaped who I am today.

LIST OF FIGURES

- Figure 1.1 Schematic of gas-phase FEBID: Volatile precursor molecules are introduced to the substrate via a gas injection nozzle, where they adsorb onto the surface. The focused electron beam dissociates these adsorbates, generating a localized solid-phase deposit, while the remaining molecular fragments desorb and are removed under vacuum. 4
- Figure 1.2 NESA-FEBIP (a) Schematic of the nanoelectrospray process. The liquid precursor is electrohydrodynamically delivered from an emitter onto the substrate, where it spreads into a thin film suitable for electron beam exposure. (b) Experimental setup for NESA-FEBID in an FEI Quanta 200 SEM. The substrate is mounted on the microscope stage and sits below a nanoelectrospray emitter that delivers the liquid precursor under vacuum conditions. (c) High-vacuum SEM micrograph of the nanoelectrospray jet emerging from the emitter under -600 V bias in the FEI Quattro S SEM. 8
- Figure 2.1 Overview of deposition process. Important radiolysis products and their roles as oxidizing and reducing species involved in Ag deposition from an AgNO_3 precursor in (a) water and (d) water-ammonia solvents. In the presence of NH_3 , Ag^+ ions can form the diamine silver complex $\text{Ag}(\text{NH}_3)_2^+$, enabling additional reduction pathways. The role of H_2O_2 is altered from purely oxidizing in water to both oxidizing Ag and reducing $\text{Ag}(\text{NH}_3)_2^+$ in water-ammonia. Furthermore, reactions with NH_3 and NH_2^{\cdot} deplete OH^{\cdot} and O_2 , suppressing the oxidation rate of Ag. A schematic of the deposition process in (b) water and (c) water-ammonia, showing the broadening of the central pillar deposit and the appearance of a ring deposit in water-ammonia. ... 15
- Figure 2.2 Deposition results. Deposition in “spot” mode, (a-d) 1 mM AgNO_3 , 30% NH_3 aqueous solution, (e-f) 1mM AgNO_3 aqueous solution. (a) 10 keV, (b) 15 keV, (c) 20 keV, and (d) 30 keV beam energy. A central deposit and small ring are formed. Ring diameter increases with increasing beam energy. At 10 and 15 keV, dendritic structures are formed on ring. (e) 30 keV, neutral pH and (f) 30 keV, pH 12: Deposit created only at the irradiation site. Exposure time is 30 s for all cases. Imaging is performed with a 30 keV, 2 nA electron beam and an Everhart-Thornley secondary electron detector. 21
- Figure 2.3. Comparison of deposits after (a) 5 s, (b) 23 s, (b) 38 s, and (d) 60 s of imaging exposure using a 30 keV, 2 nA scanning electron beam after deposition. Focused electron beam irradiation is 30 keV for 30 s in all cases. 1 mM $\text{Ag}(\text{NH}_3)_2^+$ in 30% NH_3 . Scale bar is 30 μm . Note that there is no noticeable difference in the deposits due to the imaging. 23
- Figure 2.4. Comparison of deposits formed with (a) 10 s, (b) 20 s, and (c) 30 s of irradiation. A central deposit is already recognizable at 10 s. The ring is faintly visible at 20 s and more prominent at 30 s. This confirms our simulated results that ring formation occurs over time scales much longer than the central deposit. 23

- Figure 2.5 (a) Mesh on an axisymmetric domain in COMSOL, electron beam is focused at $r = 0, z = 0$. (b) Dose rate extracted from CASINO for interpolation onto COMSOL mesh for a 30 keV electron beam. 31
- Figure 2.6 Electron beam dose rates. The spatial distribution of dose rate is a function of electron beam energy, with a higher beam energy resulting in a larger region of interaction. 2D-axisymmetric plots of dose rate for beam energies of (a) 30 keV, (b) 15 keV, and (c) 10 keV in 30% NH_3 aqueous solution. (d) Electron trajectories extracted from a Monte-Carlo simulation (30 keV shown) used to calculate dose rates. 33
- Figure 2.7 E-Beam Irradiation of Water-Ammonia. (a) Dose rate distribution at the membrane for a 30 keV electron beam in 30% aqueous solution. There are two length scales of interest. The first is associated with the region directly irradiated by the electron beam and the second with the extent of electron penetration inside the solution. (b) The concentration profile of H_2O_2 initially follows the dose rate profile. In the beam region, a quasi-steady state concentration is achieved by 10^{-5} s. After attaining its quasi-steady state concentration in the beam region, H_2O_2 continues diffusing into the envelope region, where it reaches a quasi-steady state concentration by around 1 s. (c) The concentration of e_{sol}^- increases at short times and these high concentrations drive the creation of a central pillar. After 10^{-7} s the concentration of e_{sol}^- in the beam region begins falling. 35
- Figure 2.8 Water and Water-Ammonia Deposition Outcomes. (a) Comparison of most important reduction pathways in the creation of Ag in a 30% aqueous solution. At short times, reduction of $\text{Ag}(\text{NH}_3)_2^+$ by e_{sol}^- is dominant, but H_2O_2 becomes dominant at longer times. (b) Net rate of Ag creation at membrane by all pathways in a 30% NH_3 aqueous solution. Two distinct regions of production are seen—one at the center before 10^{-5} s, and one around $15 \mu\text{m}$ which persists until times >1 s. The shading highlights the region where ring formation is predicted to occur. (c) Net rate of Ag creation at membrane by all pathways in a purely aqueous solution. No production occurs in the bulk beyond 10^{-5} s. A 30 keV electron beam and 1 mM AgNO_3 are used for all cases. 38
- Figure 2.9 Suppression of Oxidizing Species by Ammonia. Concentrations of OH^\bullet and O_2 are suppressed in water-ammonia in comparison to pure water due to their scavenging by NH_2^\bullet and NH_3 . This creates a highly reducing environment, promoting Ag nanomaterial synthesis in the water-ammonia solution. 41
- Figure 2.10 Regions of Ag Production in Water-Ammonia. Net rate of creation of Ag (difference between reduction and oxidation rates) with irradiation of a 1mM AgNO_3 , 30% NH_3 aqueous solution by a 30 keV electron beam at 1 s shown in a 2D axisymmetric domain. There is a positive rate of Ag production at the point of irradiation and in an approximately hemispherical region of the bulk. The small region of a negative creation rate indicates that at this instant and this location, Ag is being consumed by oxidation at a greater rate than it is being produced by reduction of Ag^+

or $\text{Ag}(\text{NH}_3)_2^+$. In a water system, only the central deposition region of high net Ag production rate is present. The membrane surface provides a preferential location for solid phase nucleation, which manifests in the creation of a 2D ring as observed in experiments rather than a 3D shell seen in simulations for the water-ammonia system. 43

Figure 2.11 Experimental and Computational Ring Sizes. Comparison between the experimental observations for the inner and outer diameters of rings and predictions of ring sizes from simulations of the water-ammonia system. For simulated results, the ranges represent the estimated minimum and maximum radii at which the net rate of solid Ag creation exceeds a nominal value— $1 \text{ mol/m}^3\cdot\text{s}$ —at times of 10 ms or greater. This represents the range of positions over which ring deposition is predicted to occur. The size of the ring grows as the beam energy increases. The disagreement arises from the overprediction of stopping power at low electron energies by the Joy-Luo stopping power model used in the simulations. 44

Figure 2.12 Temperature in aqueous environment after 30 s of heating with a 30 keV, 2 nA electron beam. All electron beam energy is assumed to be converted into thermal energy, using a volumetric heat generation rate equal to the spatial dose rate of electron energy loss shown in Figure 2.5 (b). 48

Figure 2.13 Comparison of net Ag creation rates at radial positions $r = 7 \text{ }\mu\text{m}$, in the intermediate region between the central pillar and the ring, and $r = 14 \text{ }\mu\text{m}$, at the ring location, in a 30 keV beam simulation in water-ammonia. Note that the rate at $7 \text{ }\mu\text{m}$ falls off to near zero within milliseconds, while at $14 \text{ }\mu\text{m}$ it is appreciable for much longer times. 50

Figure 3.1. The solution of water and ammonia as solvent containing Ag^+ and $\text{Ag}(\text{NH}_3)_2^+$ precursor is nanoelectrosprayed onto the substrate and forms a film. As the solution is supplied to the substrate, the film size increases. Water and ammonia evaporate from the film surface slowing the growth of the film. The film reaches a quasi-steady state size and ammonia concentration as the evaporation balances the addition of solution via nanoelectrospray. The concentrations of non-volatile Ag^+ and $\text{Ag}(\text{NH}_3)_2^+$ precursors increase continuously (i.e., do not achieve a steady state value). The presence of $\text{Ag}(\text{NH}_3)_2^+$ provides an additional source of stored ammonia, as a single $\text{Ag}(\text{NH}_3)_2^+$ ion-complex releases two ammonia molecules if reduced to Ag. 56

Figure 3.2 Important chemical pathways for silver production in LP-FEBID with an ammonia-water solvent and metal salt precursors (shown in green). The reducing species are illustrated in red and oxidizing species in blue. In the absence of NH_3 (a), the precursor Ag^+ is converted to Ag via reduction by solvated electrons. The Ag can then be reverted to Ag^+ via oxidation. The addition of ammonia to the solution (b) leads to partial conversion of Ag^+ to $\text{Ag}(\text{NH}_3)_2^+$. This adds an additional silver formation pathway as $\text{Ag}(\text{NH}_3)_2^+$ can be reduced to Ag by H_2O_2 . The role of H_2O_2 is shifted from purely an oxidizer of Ag to both an oxidizer and reducer. Presence of NH_3 also depletes the concentrations of oxidizing species O_2 and OH^\bullet , making the environment more reducing. Further addition of NH_3 (c) amplifies this effect, leading

to the environment becoming even more reducing. The size of each species oval indicates their relative concentrations. At intermediate ammonia concentrations (b) yields the relative amounts of the two precursor species and the oxidizers that provide the optimum condition for high growth/ high resolution deposition, i.e., electrochemical lensing. 57

Figure 3.3 Monte-Carlo simulation is used to calculate the dose rate distribution due to a 30 kV, 3 nA electron beam irradiation. (a) The simulation domain - a 1 μm thick liquid film is overlaid on a 0.1 μm gold layer, which is placed on a thick (treated as semi-infinite) silicon substrate. (b) The axisymmetric dose rate distribution within the liquid film. The origin (0,0) is the point of electron beam irradiation, and the axis of symmetry is the vertical line passing through this point. Due to negligible axial variation in dose rate, the problem can be simplified to 1D axisymmetric. 61

Figure 3.4 (a) Nanostructure deposition in water-ammonia solvents. In pure water or low ammonia, minimal nanostructure formation occurs due to oxidizing conditions. Optimal ammonia concentrations for electrochemical lensing result in focused and rapid nanostructure growth with high resolution, as reducing conditions prevail in the near-field and oxidizing conditions prevent nanostructure formation in the far-field. High ammonia concentrations lead to rapid growth of solid phase throughout the domain with loss of resolution. Panel (b) shows the simulated axisymmetric (mirrored around y-axis) Ag concentration profiles, after 1 second electron beam irradiation across different NH_3 -water solution concentrations Ag concentration profile in a 26.5 mM AgNO_3 film, highlighting optimal NH_3 concentration for electrochemical lensing at 0.25 M NH_3 Panel (c) illustrates the 265 mM AgNO_3 scenario, where increased precursor availability leads to substantial far-field deposition even at very small NH_3 concentrations in the film, resulting in broadening growth and diminished resolution. 66

Figure 3.5 Key reaction rates and concentrations in the near-field (center) for a 26.5 mM AgNO_3 solution at NH_3 concentrations of 0.1, 0.25, 1, and 3 M post 1 sec electron beam irradiation. Panel (a) illustrates the net instantaneous rate of silver deposition showing peak Ag creation in the near-field at 0.25 M NH_3 . The net Ag silver deposition is the sum of all the reduction and oxidation pathways for precursors and Ag, respectively (b). Concentrations of key oxidizing and reducing species are shown in (c). Concentrations of Ag and the precursor ions are shown in (d), which indicates a partial conversion of Ag^+ to $\text{Ag}(\text{NH}_3)_2^+$ contributing to a negligible Ag creation at 0.1 M NH_3 (a). Additionally, decreasing precursor concentrations from 0.25 M to 3 M NH_3 in (d) is responsible for the drop in Ag creation..... 70

Figure 3.6 Key reaction rates and concentrations for far-field (4.5 μm from the center) silver deposition dynamics under varying NH_3 concentrations in a 26.5 mM AgNO_3 solution following electron beam exposure of 1 sec are shown. The net rate of Ag deposition (a) shows the increase in the rate of Ag creation in the far-field with higher NH_3 concentrations - this rate is the sum of all the reduction and oxidation reaction rates shown in (b). Concentrations of reducing and oxidizing species participating in creation or consumption of Ag is showing in (c). The Ag and precursor ions

concentrations (d) show an increase in far-field Ag creation with increased NH₃, as well as a corresponding drop in the precursor ion concentrations..... 72

Figure 3.7 Impact of NH₃ concentration on Ag⁺/Ag(NH₃)₂⁺ precursor diffusion and Ag creation. (a-d) schematically illustrate the effect of increasing ammonia concentrations on diffusion of precursor in the domain and resulting Ag creation. In low NH₃ or pure aqueous conditions (a), oxidizing conditions inhibit Ag formation, with minimal precursor diffusion. At optimal NH₃ concentration (b), a reducing environment in the near-field promotes precursor cations Ag⁺ and Ag(NH₃)₂⁺ conversion to Ag, while maintaining oxidizing conditions in the far-field, promoting precursor cation diffusion towards the near-field. Higher NH₃ concentrations (c-d) lead to Ag⁺ and Ag(NH₃)₂⁺ conversion in both the near-field and far-field, decreasing precursor cations available for diffusion towards near-field and slowing Ag growth. Panel (e) shows the simulated diffusive flux profiles for the precursor over the domain for various NH₃ concentrations under a 30 kV electron beam for 1 second. Panel (f) depicts the total diffusion of Ag⁺ and Ag(NH₃)₂⁺ towards the near-field at a distance of 0.2 μm from the center over a time of 1 s..... 75

Figure 3.8 AFM images of nanostructures from NESA-FEBID using water-ammonia solutions with 250 μM AgNO₃ at 30%, 25%, and 15% NH₃ concentrations in top-view 2D (a-c) and 3D (d-f) radial profiles (g-i). Nanostructures are created with 1s 30 kV electron beam in 'spot' mode. Ag growth varies with NH₃ concentration, showing focused near-field growth at 15% NH₃ and increased far-field growth at 25% and 30% NH₃. Normalized experimentally determined pillar profiles (j) are compared to simulated Ag concentration profiles at varying NH₃ levels (k), showing qualitative agreement and presence of an optimal NH₃ concentrations for focused near-field Ag growth, the signature of the electrochemical lensing..... 78

Figure 4.1 Chemical-kinetic pathways illustrating how varying the ammonia concentration affects copper etching or deposition. The relative sizes of each species “balloons” (e.g., ammonia, copper ions/ion-complexes, oxidizing species, reducing species) in the schematic reflect their approximate concentrations. At high ammonia concentration (left), copper-amine complexation is more pronounced and radiolytic reducing species outcompete radiolytic oxidizers, driving copper redeposition. At low ammonia concentration right, less copper-amine complexes form while the radiolytic oxidizing species predominate, leading to net copper etching..... 86

Figure 4.2 Simulations reveal the competition between reduction (deposition) and oxidation (etching) pathways under varying conditions. (a) Monte Carlo simulations are performed to calculate the dose rate for a 20 kV electron beam. A 1 μm water-ammonia film is analyzed atop a 200 nm copper layer, on a thick silicon substrate (treated as semi-infinite). (b) Effect of ammonia concentration at the beam center (2.5 s exposure, 0.1 mM initial deposition precursor copper ion/ion-complexes). Fractional reaction yields for oxidation (proportional to H₂O₂ and OH[•] concentrations) and reduction (proportional to the product of precursor cations and solvated electrons concentration) are normalized to the 0.1 mM ammonia case. Increasing ammonia lowers radiolytic production of oxidizing species (reducing the rate of etching). There

is a spike in reduction rates due to higher precursor availability at lower ammonia concentration. However, with an increase in ammonia concentration >1000 mM, rapid precursor cation depletion, caused by accelerated initial consumption from high reduction rates, ultimately inhibits reduction and deposition. (c) Reaction yields normalized to 0.01 mM precursor concentration (1000 mM ammonia, 2.5 s exposure). Higher precursor availability increases reduction yields, while oxidation remains unaffected. (d) High ammonia concentration (10,000 mM NH₃, 1 mM initial concentration of precursor cations). High ammonia creates a strongly reducing environment, driving rapid copper deposition initially. However, prolonged electron beam exposure depletes precursor cations through reduction reactions, weakening the reducing effect over time and slowing down deposit growth. (e) Low ammonia concentration (100 mM NH₃, 0.01 mM initial concentration of precursor cations). Low ammonia fosters an oxidizing regime, etching copper initially. With extended exposure, reduction yield rises faster than oxidation yield, slowing etching for longer e-beam exposures..... 89

Figure 4.3 Visualization of electron-beam-mediated deposition/etching via SEM imaging and EDS analysis. (a) Zoomed-out SEM image of 2x2 ‘spot’ patterns formed by focused electron beam exposure (20 kV, 2.5 nA) of water-ammonia film. Locations of liquid films are seen as light gray shade domains. (b) Zoomed-in SEM image of a single etched ‘spot’ in 5% ammonia film and 0.5 s exposure time. (c-d) EDS elemental maps: (c) copper signal (green) decreases at etched site, (d) elevated silicon signal (yellow) from the substrate at etch site. 97

Figure 4.4 AFM images and their corresponding angularly averaged height profiles show the evolution of copper nanostructures under different ammonia concentrations and electron-beam irradiation times. (a,b) At low ammonia (5%) and short irradiation (0.5 s), a predominantly oxidizing environment leads to net copper etching. (c,d) Increasing the irradiation time to 1.5 s under the same low ammonia conditions causes widening of the etch via oxidation. The copper ions/ion-complexes formed due to prior oxidation diffuse towards and redeposit in the center at the e-beam impingement spot, forming the characteristic “peak-in-valley” structure. (e,f) A 2.5 s e-beam exposure at same (5%) ammonia concentration further widens the etched region and grows the redeposited peak. (g,h) At higher ammonia concentration (25%), copper is rapidly deposited even at short (0.5 s) irradiation time from the precursor cations released to the solution from the substrate on contact with ammonia, forming a nanopillar (i,j) At 1.5 s e-beam irradiation exposure, stronger reducing conditions and more copper-amine ion complexation drive rapid copper deposition at the center, but with an additional off-center ring formation. (j,k) Extending the irradiation to 2.5 s under high ammonia results in a plateau of the deposit height due to local depletion of copper ions/ion-complexes, slowing further pillar growth..... 99

Figure 4.5 Schematic of key mechanisms underlying the process outcomes and deposit/etch evolution at varying ammonia concentrations and irradiation times. (a) At low ammonia and short times, oxidizing species dominate, leading to net copper etching. (b) As irradiation continues under low ammonia, the local concentration of copper ions/ion-complexes rises due to initial copper oxidation, causing redeposition and

“peak-in-valley” nanostructure formation. (c) At high ammonia and short times, increased rate of copper-amine complexation and a reducing environment favor rapid copper redeposition at the beam impingement site. (d) With prolonged exposure under high ammonia, the availability of copper ions/ion-complexes near the center diminishes with deposit growth, while diffusion of precursor cations from the surrounding to the e-beam irradiation site and diffusion of the reducing species outwards from the center drives ring-like structure formation. 102

Figure 4.6 Line nanostructures on a copper substrate created with 5% ammonia-water NESA film, using 20 kV, 2.5 nA electron beam. (a) Backscattered-electron SEM image (3 kV imaging) of a line “written” with 3 spots per μm (0.5 s dwell each). (b) AFM height profile of etched pattern (a), showing a sequence of discrete etch pits that do not fully merge. (c) Backscattered-electron SEM image of a line “written” with 10 spots per μm (0.15 s dwell each). (d) AFM profile of etched pattern (c), illustrating the etch morphology and producing an interconnected etched line..... 105

TABLE OF CONTENTS

ACKNOWLEDGEMENTS	iv
LIST OF FIGURES	vi
SUMMARY	xv
BACKGROUND AND SCOPE	1
1.1 Overview	1
1.2 FEBIP precursor phase	2
1.2.1 Gas Phase Focused Electron Beam Induced Processing (GP-FEBIP)	3
1.2.2 Liquid Phase Focused Electron Beam Induced Processing (LP-FEBIP)	5
1.3 Use of Ammonia-Based LP-FEBIP systems: Motivation	9
The Role of Ammonia in Radiolytic Redox Dynamics and Silver Deposition Morphologies	12
1.4 Introduction	12
1.5 Experiments	19
1.5.1 Experimental Sample Preparation	19
1.5.2 Deposition Results	19
1.5.3 Imaging-Induced Ag Growth	22
1.6 Simulations	24
1.6.1 Model Formulation	24
1.6.2 Theoretical Predictions	32
1.6.3 Consideration of Thermal Effects	46
1.6.4 Time Evolution of Deposition Rates	49
1.7 Concluding Remarks	51
Electrochemical Lensing for High-Resolution Nanostructure Synthesis	53
1.8 Introduction	53
1.8.1 FEBID Synthesis in NESA Films	55
1.8.2 Reaction Pathways Essential to Nanomaterial Synthesis	58
1.9 Simulations	59
1.9.1 Reaction and Transport Model	59
1.9.2 Electrochemical Lensing: Insights from Simulations	65
1.10 Experiments	76
1.10.1 Experimental Sample Preparation	76
1.10.2 Electrochemical Lensing - Corroborating Experiments	76
1.11 Concluding Remarks	79
E-Beam-Guided Redox-Controlled Etching and Deposition	81
1.12 Introduction	81
1.13 Theoretical Analysis	87
1.13.1 Simulating Redox Dynamics	87
1.13.2 Ammonia Concentration Effects	91
1.13.3 Release of Cations from Metal Substrate	92

1.13.4 Electron Beam Exposure Time Effects	93
1.14 Experiments	94
1.14.1 Experimental Sample Preparation	94
1.14.2 Redox-Mediated Etching and Deposition Interplay: Experimental Validation	94
1.15 Concluding Remarks	106
Conclusions	108
1.16 Major Contributions and Publications	108
1.17 Beam-Driven Effects: Key Considerations and Future Directions	110
1.17.1 Liquid Heating via E-Beam	110
1.17.2 Solid Deposit Heating via E-Beam	111
1.17.3 Axial (Across the Film) Temperature Gradients in the Liquid Film	112
1.17.4 Electric Field Effects	113
1.17.5 Effects of the solid deposit presence	114
1.17.6 Soret (Thermophoresis) Effect	114
1.17.7 Temperature Dependent Kinetics and Transport	115
1.17.8 Growth-Rate and Deposit Crystallinity	116
1.18 Recommendations for future work	117
APPENDIX A. Kinetic Rate Constants	119
APPENDIX B. G-Values	123
APPENDIX C. Diffusion Coefficients	125
REFERENCES	127

SUMMARY

In this dissertation, a focused electron-beam-mediated approach to nanoscale synthesis and modification is presented, spanning from fundamental redox studies to the extension of these studies towards unique fabrication strategies in water-ammonia environments. The document comprises three core chapters that collectively investigate how water-ammonia solvents can be harnessed for direct-write nanostructure synthesis via focused electron beam-induced processes. The overarching theme is that the radiolytic chemistry of water-ammonia solutions fundamentally reshapes how reducing and oxidizing pathways compete to form or remove solid material at the nanoscale.

Chapter 2 discusses the influence of introducing ammonia in an aqueous silver nitrate solution on the oxidation-reduction processes under electron beam irradiation. Ammonia preferentially scavenges oxidizing radiolysis products, thereby suppressing the oxidation of metallic silver. At the same time, it changes the role of hydrogen peroxide from an oxidizer of silver in pure water to a dual role as both an oxidizer of silver and a reducer of the silver–ammine complexes. This fundamental shift in chemical pathways makes the environment more reducing, enabling silver deposition at a faster rate but over an extended region around the primary beam spot, rather than being limited to the immediate site of irradiation.

Chapter 3 shows how leveraging the water-ammonia solvent and silver nitrate-based chemistry, a highly reducing environment is created at the point of focused electron beam. At the same time, the environment in the farfield stays oxidizing, avoiding unwanted deposition. This ‘electrochemical lensing’ enhances growth rate in the near-field of the

beam without sacrificing lateral resolution, offering high resolution and rapid nanofabrication.

Chapter 4 applies the ammonia-based solvent approach to precursor-free electron-beam patterning of copper, revealing that adjusting ammonia concentration can lead to net oxidation (etching) or reduction (deposition). At lower ammonia concentrations, the oxidizing environment leads to etching of copper at short electron beam exposure times. Over longer beam exposures, the copper ions/ion-complexes released by this initial oxidation are reduced and deposited back into the etched locations, forming peak-in-valley structures. Higher ammonia concentrations result in a high rate of copper–ammine complexation and suppression of oxidizing species, creating a strongly reducing environment that enables copper deposition even at short beam exposures.

Collectively, this dissertation advances the fundamental understanding of electron-beam-induced radiolytic chemistry in water-ammonia solutions and applies these advances to liquid phase Focused Electron Beam Induced Processing of nanomaterials.

BACKGROUND AND SCOPE

1.1 Overview

Synthesis of structures at the nano- to the micro-scale has become an area of great importance in nanoengineering. To enable direct-write 3D fabrication of topologically complex nanostructures, Focused Electron Beam Induced Processing (FEBIP) method has been developed [1-3]. FEBIP is a class of techniques leveraging directed delivery of energetic electrons to facilitate localized chemical reactions. FEBIP encompasses two complementary processes: Focused Electron Beam Induced Deposition (FEBID) [4, 5] and Focused Electron Beam Induced Etching (FEBIE) [6]. In addition, electron beam mediated processes have been used for doping materials such as boron nitride [7] and graphene [8]. Electron beam irradiation has also show to assist in strain lithography [9] and defect engineering [10]. Although all these FEBIP processes differ in their outcomes, they all utilize the ability of a tightly focused electron beam to locally activate reactions at an interface. The utility of FEBIP has been shown in material science applications including magnetics, plasmonics, nanoelectronics, and optics [3, 5, 11].

The FEBIP process generally takes place in the vacuum chamber of a Scanning Electron Microscope (SEM). An electron beam acts as a source of focused, high-energy electrons directed to the substrate where they interact with the substrate material and precursor molecules on the substrate surface. When beam electrons interact with matter, they undergo elastic and inelastic collisions, generating a cascade of events [12]. These can include heating and charging of matter, electron scattering, bond cleavage, ionization, generation

of secondary electrons, and the creation of reactive species. The main parameters that govern the electron-driven chemical reactions are the precursor chemistry, substrate material, energy and flux of primary e-beam and generated electrons, and the exposure time of precursor to the electrons [13]. If appropriate thermodynamic conditions are established, one can drive site-specific transformation of material, thereby offering a path to “direct-write” nanofabrication.

In FEBID, the electron beam converts suitable precursors into nonvolatile species forming deposits attached to a substrate, effectively “printing” material in place. FEBID has been exploited for repairing lithographic masks, creating high-resolution interconnects in integrated circuits, and 3D nanomanufacturing [3, 14]. The process can be used to synthesize a wide variety of nanomaterials, including metallic [15], bimetallic [16], oxide [17] and carbon-based [18] and semiconductor [19] nanostructures.

FEBIE is the counterpart to deposition where the electron beam facilitates reactions to selectively remove material from a solid surface to etch 3D nanostructures. Much like FEBID, the process depends on driving electron-induced reactions, but in a subtractive/etching mode. The byproducts are deliberately volatile or solvent soluble, thus creating the desired etch pattern in the substrate.

1.2 FEBIP precursor phase

Selection of precursor phase is an important consideration for FEBIP, as it largely dictates the rate of reaction, final material purity, and achievable spatial resolution. This section discusses common precursors used in FEBIP.

1.2.1 Gas Phase Focused Electron Beam Induced Processing (GP-FEBIP)

Due to ease of handling gases relative to liquids in vacuum environments, gas phase precursors have historically been the precursor of choice in FEBIP [20-22]. Organometallic and inorganic compounds are the most commonly used gaseous precursors [15, 23].

Gas-phase FEBID (GP-FEBID) enables the deposition of a wide spectrum of metals, including silver [24, 25], gold [26], copper [27], and ruthenium [28]. Complementary to this additive process, gas-phase FEBIE (GP-FEBIE) has been successfully employed to remove materials, for example, titanium [29], gallium arsenide [30], and silicon [31], and has also proved valuable for cleaning solid contaminants from nanostructured surfaces [1, 32, 33].

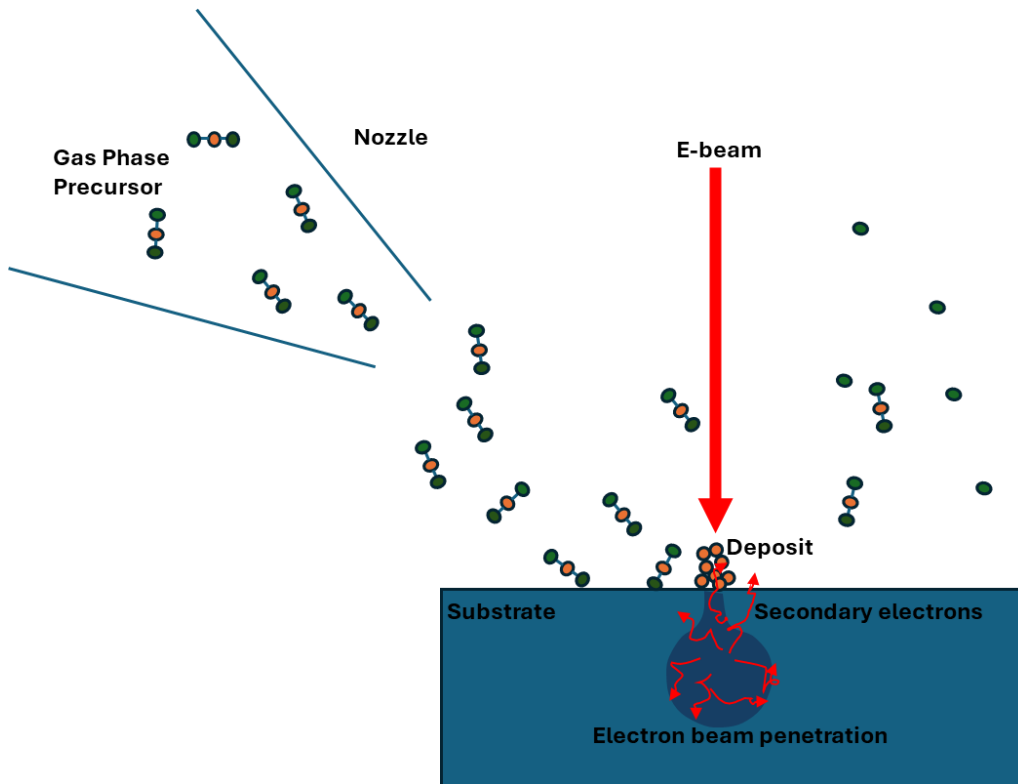


Figure 0.1 Schematic of gas-phase FEBID: Volatile precursor molecules are introduced to the substrate via a gas injection nozzle, where they adsorb onto the surface. The focused electron beam dissociates these adsorbates, generating a localized solid-phase deposit, while the remaining molecular fragments desorb and are removed under vacuum.

The general mechanism of GP-FEBIP is graphically illustrated in **Figure 1.1**. Volatile precursor molecules are delivered via a gas injection nozzle in the vicinity of the substrate. Once adsorbed on the surface, the substrate is exposed to electron beam irradiation. The electrons undergo elastic and inelastic collisions with the atoms of the substrate, with the latter leading to generation of low energy secondary electrons. The secondary electrons emerge from the surface and interact with the adsorbed molecules leading to their dissociation if their energy matches the ionization cross-section and bond energies of precursor molecules. This causes formation of localized solid deposits, while the remaining volatile fragments are removed from the system by the vacuum pumps. The GP-FEBIE follows the same principle to etch by removing atoms/molecules from the substrate via secondary-electron mediated oxidation. Despite its proven utility, gas-phase FEBIP also presents certain limitations. Challenges include carbonaceous contamination from the precursor ligands and relatively slow deposition rates [5, 34].

1.2.2 Liquid Phase Focused Electron Beam Induced Processing (LP-FEBIP)

Use of liquid phase precursors for FEBIP (LP-FEBIP) offers higher growth rates and a higher purity as compared to gas phase precursors, as well as a broader selection of material chemistries [35]. However, the use of liquid-phase precursors in FEBIP is challenging due to the inherent difficulty of handling liquids within a high-vacuum environment. Liquids are prone to evaporation, freezing, and instability under vacuum, complicating the interactions with the electron beam. Several techniques have been developed to overcome these challenges. In one approach, the liquid precursor is enclosed within a sealed compartment, isolating it from the high-vacuum surroundings [36, 37]. The electron beam enters the system via an ultra-thin electron transparent membrane, which also acts as the

substrate for deposit nucleation. This approach has been used to grow high purity metals, including gold [38], silver [39], platinum [40], and binary alloys [41]. However, it limits the substrate materials that can be used as the deposit is grown on a e-beam transparent membrane. Additionally, the electron beam may damage the membrane at higher energy and currents that are desired for high resolution and faster deposition rates [39]. Further, as deposit begins to form on the membrane/substrate, the e-beam electrons must interact with the deposit itself that impacts the shape and size of synthesized structures. These factors limit the electron energies used for deposition and the topological complexity of nanostructures that can be deposited.

For many practical applications that require a broad range of substrate options, or the ability to build complex 3D nanostructures, depositing onto a free-surface liquid film can be advantageous. One such technique involves forming a bulk liquid layer by condensation inside an environmental (low-vacuum) scanning electron microscope (ESEM) [42, 43]. In some implementations, microwells [42] and liquid injection via nanocapillaries [44] have been integrated with ESEM conditions to create liquid layers for FEBID. However, use of this technique is limited due to the poor control of thickness of liquid films obtained and the choice of solvents that could be condensed. A thicker liquid film can lead to deposition on the liquid-vacuum interface and loss of spatial control.

An alternative technique that addresses these limitations is NanoElectrospray-Assisted Focused Electron Beam Induced Processing (NESA-FEBIP). In this technique, liquid is electrohydrodynamically delivered using nanoelectrospray process, forming an ultrathin free-surface film on the substrate. Because of small film thickness, electron beam can

penetrate the film, allowing the deposit to form directly on the substrate rather than at the liquid-vacuum interface [35, 45, 46]. **Figure 1.2**, panel (a) schematically depicts the nanoelectrospray process, where the liquid precursor is ejected from the tapered capillary emitter and spreads into a thin film on the substrate. The film is exposed to an electron beam. The electrons undergo collisions with the atoms/molecules of the liquid film and the substrate, including generation of low energy solvated electrons and triggering chemical and transport processes in the liquid. Panel (b) shows the experimental setup in an FEI Quanta 200 SEM, with the substrate mounted on the grounded microscope stage beneath the nanoelectrospray emitter, ensuring precise delivery of the liquid precursor under vacuum conditions. The SEM image of an actual emitter in the process of nanoelectrospray is shown in panel (c).

Liquid-phase focused electron beam induced etching (FEBIE) extends the etching process to liquid environments. The process has been used to etch nickel [47] and copper using sulfuric acid precursor [48, 49].

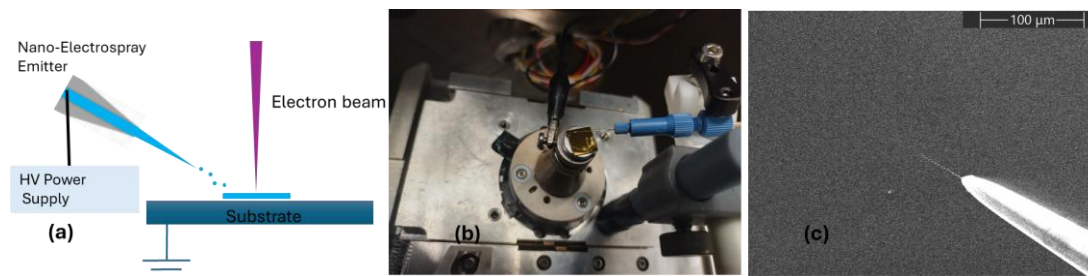


Figure 0.2 NESAFEBIP (a) Schematic of the nanoelectrospray process. The liquid precursor is electrohydrodynamically delivered from an emitter onto the substrate, where it spreads into a thin film suitable for electron beam exposure. (b) Experimental setup for NESAFEBID in an FEI Quanta 200 SEM. The substrate is mounted on the microscope stage and sits below a nanoelectrospray emitter that delivers the liquid precursor under vacuum conditions. (c) High-vacuum SEM micrograph of the nanoelectrospray jet emerging from the emitter under -600 V bias in the FEI Quattro S SEM.

LP-FEBIP processes that rely on the reduction of precursor ions for deposition or the oxidation of atoms for etching are governed by reaction involving the radiolytic species. Radiolysis is initiated when the electron beam irradiates the liquid, resulting in the formation of a range of reactive chemical species. Among these, some drive the reduction of precursor ions, while others promote the oxidation of substrate or deposited atoms. Depending on solvent, the outcome of radiolysis is either a net reducing environment that favors additive deposition or a net oxidizing environment that leads to subtractive etching.

1.3 Use of Ammonia-Based LP-FEBIP systems: Motivation

The addition of ammonia to an aqueous solution substantially increases the lifetime of solvated electrons [50, 51]. This has prompted us to investigate the effects of ammonia-based solvents on FEBIP, where solvated electrons play the role of a key radiolytic reducing species, and is the primary focus of this doctoral research.

The increase in lifetimes of solvated electrons enhances the reduction rates and deposition via FEBIP in water-ammonia solutions. In contrast, the purely aqueous solutions lead to conditions favorable for oxidation reactions for subtractive FEBIP nanomanufacturing. This is due to generation of higher concentrations of oxidizing species during radiolysis of ammonia vs water. From the processing perspective, pure water solvents lead to the creation of thicker (tens of micrometers) films due to higher surface tension. This leads to nanostructure growth initiated by the e-beam at the solution-vacuum interface with floating deposits, which cannot attach to the substrate due to limited depth of e-beam penetration into the liquid film. The addition of ammonia, on the other hand, decreases the surface

tension of the solution and increases substrate wetting. Film thinning is further enhanced by electrowetting associated with the electrospray process that delivers the charged solution via electrokinetic ion separation. When a focused e-beam penetrates through a very thin liquid layer with minimal scattering, the deposition/etching process is initiated at the substrate-solution interface via heterogeneous electrochemistry. This tight 1D confinement of the liquid phase enables precise position control of e-beam induced reactive interactions and intrinsically strong attachment of deposits to the substrate.

This PhD research establishes a comprehensive understanding of the interplay between precursor chemistry, radiolytic species dynamics, and transport phenomena in ammonia-based LP-FEBIP systems. The dissertation is structured in a series of logically connected chapters that progressively refine our understanding and control of electron-beam-driven deposition and etching processes in water-ammonia systems.

In Chapter 2, we explore the role of ammonia on silver deposition from aqueous silver nitrate. Through a combination of targeted experiments and coupled reaction-transport simulations, we demonstrate that ammonia markedly alters the balance between reduction and oxidation pathways. By extending the lifetime of solvated electrons, suppressing oxidizing species, and facilitating the formation of the diamine silver complex, we observe a distinct transition in deposit morphologies. This study establishes the fundamental foundation for use of ammonia in FEBIP deposition/etching.

Guided by these insights established in Chapter 2, Chapter 3 presents an approach how the ammonia-induced redox modulation can achieve spatially focused and highly reducing environment at the electron beam impingement site, promoting deposition of

nanostructures with high resolution and high growth rate. In parallel, the environment in the farfield can be kept oxidizing, suppressing unwanted growth around the deposit. This approach of spatially-selective competitive interplay between reduction and oxidation, which we termed ‘electrochemical lensing,’ enables nanostructure deposition with rapid growth and enhanced spatial resolution.

Finally, in Chapter 4, we extend the solvent-mediated control strategy of electron beam processing to copper surfaces. Building upon the fundamental principles of competitive interplay between reduction and oxidation developed in Chapter 3, we show that the careful manipulation of ammonia concentration not only governs the extent of etching but also drives selective copper re-deposition. This dual etch-deposit process produces unique peak-in-valley nanostructures, demonstrating the versatility of water-ammonia solvents in achieving both additive and subtractive fabrication within a unified processing environment without change of a precursor.

Together, these studies establish a progressive research trajectory where each investigation informs and refines the next, ultimately advancing our capability to harness water-ammonia solvent chemistry for precise nanofabrication using electron beams.

THE ROLE OF AMMONIA IN RADIOLYTIC REDOX DYNAMICS AND SILVER DEPOSITION MORPHOLOGIES

1.4 Introduction

In the previous chapter, the broader context for ammonia-based liquid-phase FEBIP has been introduced, noting its potential to modulate the radiolytic environment. Here, we present a comprehensive experimental and theoretical investigation using water-ammonia silver nitrate solutions. We uncover how the creation of ammonia-enabled reduction pathways, in particular the role of diamine silver complex redox chemistry, alters reduction and oxidation rates that govern the ultimate morphology of deposited Ag. These results not only provide an original demonstration of the impact of ammonia on electron beam mediated metal salt redox chemistry but also serve as a blueprint for new FEBIP nanofabrication schemes introduced in subsequent chapters.

Electron beam and matter interactions lead to very interesting chemistry on micro- and nanoscales [12]. Electron-mediated chemistry in the liquid phase is an important problem that has applications in fields like focused electron beam-induced deposition (FEBID) and nanoparticle synthesis and aggregation [52, 53]. These applications are key steps in the further development of control over matter on ever-smaller length and time scales, which is an engine for technological progress. Direct writing of nanoscale structures with FEBID is a promising route to atom-by-atom creation of complex 3D nanostructures [4]. It has the potential for exquisite control of topological structure and chemical composition in three dimensions down to atomic scales. Performing FEBID in liquid phase precursors removes

the roadblock of low deposition rates and allows the use of unique synthesis chemistries. Complementary to focused electron beam nanomaterial synthesis are plasma-based techniques which also exploit electron interactions in solutions for improved control of structure and reactivity of nanocatalysts for emerging energy conversion applications [54]. These are techniques for inducing electrochemistry without electrodes, which allow new angles from which to revisit the basics of electrochemistry and the ability to realize/accelerate reactions (e.g., formation of multi-component alloys with accurate control of composition and phase) that are difficult or impossible in conventional electrochemistry. Common to these applications is the requirement to understand and control the nature and extent of interactions between electrons, their environment, and other reacting species. The practical realization of these tantalizing possibilities requires the fundamental understanding of solvated electron-mediated redox chemistry and its interplay with reacting species transport. Despite the ability to focus an electron beam down to the nanometer scale at high energies, solid deposition occurs on the micrometer scale [55]. This length scale is dictated both by the extent of penetration of low-energy electrons and by radiolysis chemistry and transport [18, 56]. The dominant processes have been studied for several aqueous solvent systems [42, 57, 58]. The addition of ammonia has been demonstrated to provide unusual stability in holding electrons in solution [50, 59]. This stability is implicated in the ease of silver nanoparticle synthesis in water-ammonia solutions, while dramatically increasing system chemical reaction and transport complexity.

The impact of ammonia on the formation of different shapes of deposits and the spatial-temporal dependence of the deposition rate is the new insight we present in this work. In

particular, the role of solvated electrons and their interactions with other radiolytic species, as well as the transport of these species within the region of electron beam influence, is not well understood. Previously, it has been shown that Ag nanostructures can be created from irradiation of an aqueous solution of AgNO₃ with a high energy electron beam [60]. As the reducing radiolytic species reduce Ag ions and complexes, a parallel process of oxidation occurs. The interplay of these oxidizing and reducing pathways determines the size, location, and structure of the produced nanomaterials.

The morphology and deposition rates of created nanostructures are known to depend on the local pH of the solution. A higher pH leads to an increase in the ratio of reducing to oxidizing species [61]. This leads to aggregation and agglomeration of metallic nanostructures in higher pH environments and dissolution at lower pH. In addition, pH affects the crystallinity of metallic deposits, with increasing pH leading to more crystalline deposits [60].

In this work (**Figure 2.1**), we demonstrate that ammonia is useful as a mediator of the behavior of different radiolytic species, particularly in changing the role of hydrogen peroxide from a strong oxidizer (purely aqueous) to a strong reducer (water-ammonia). This results in substantially different deposit morphologies, *i.e.*, ring formation in addition to a central pillar as observed in purely aqueous solutions. We explain this behavior through complementary experiments and first-principles reaction-diffusion simulations of electron beam-induced deposition of Ag in a water-ammonia system.

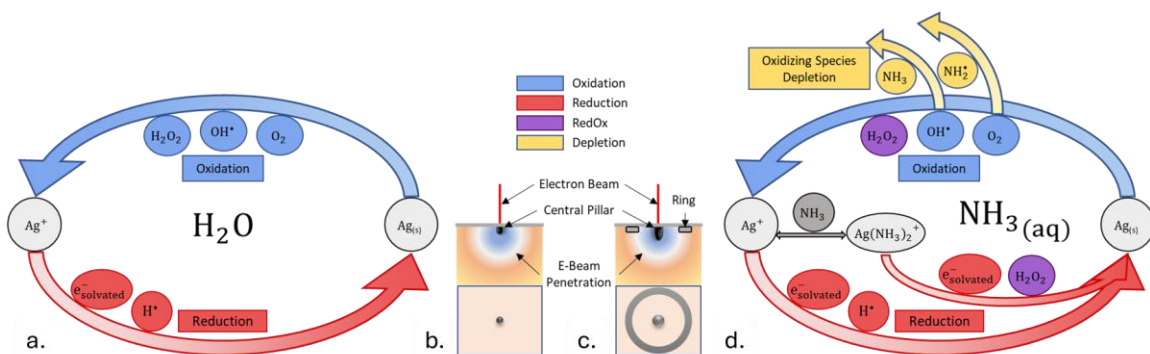
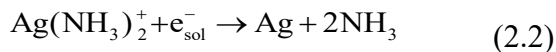
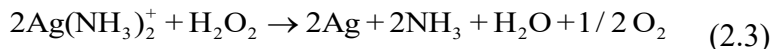


Figure 0.1 Overview of deposition process. Important radiolysis products and their roles as oxidizing and reducing species involved in Ag deposition from an AgNO_3 precursor in (a) water and (d) water-ammonia solvents. In the presence of NH_3 , Ag^+ ions can form the diamine silver complex $\text{Ag}(\text{NH}_3)_2^+$, enabling additional reduction pathways. The role of H_2O_2 is altered from purely oxidizing in water to both oxidizing Ag and reducing $\text{Ag}(\text{NH}_3)_2^+$ in water-ammonia. Furthermore, reactions with NH_3 and NH_2^\bullet deplete OH^\bullet and O_2 , suppressing the oxidation rate of Ag. A schematic of the deposition process in (b) water and (c) water-ammonia, showing the broadening of the central pillar deposit and the appearance of a ring deposit in water-ammonia.

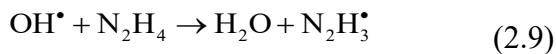
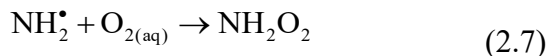
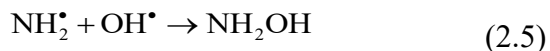
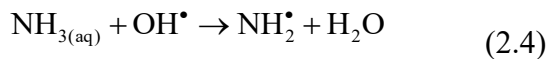
In water, AgNO_3 dissociates into Ag^+ and NO_3^- . Under electron beam irradiation, a process of radiolysis takes place, resulting in the creation of solvated electrons (e_{sol}^-), H^\bullet , H_2 , OH^\bullet , H_2O_2 , HO_3^+ , and HO_2^\bullet as primary radiolysis species [62]. These species react with one another and the solution to form secondary radiolysis species such as O_2 . The species of greatest significance for synthesis of Ag nanomaterials are the ones that either reduce Ag^+ to Ag or oxidize Ag to Ag^+ . As shown in **Figure 2.1** (a), e_{sol}^- and H^\bullet are the reducing species for Ag^+ , while H_2O_2 , O_2 and OH^\bullet are species oxidizing Ag. At any point in space and time, the creation of an Ag solid phase is only possible if the rate of reduction is higher than the rate of oxidation. In the case of the water- AgNO_3 system, a net-reducing environment exists only at the point where electron beam interacts with solution, resulting in the creation of central pillar, as shown in **Figure 2.1**. The rate of deposition is diminished by the presence of oxidizing species, such that only in a very small region near the electron beam impingement point can solid formation occur. The use of an aqueous ammonia solvent for AgNO_3 leads to a significant change in chemical behavior. The presence of ammonia in an aqueous solution triggers the formation of diamine silver ion complexes, $\text{Ag}(\text{NH}_3)_2^+$, from Ag ions, Equation (2.1). This reversible reaction strongly favors the formation of $\text{Ag}(\text{NH}_3)_2^+$, to the extent that free Ag^+ concentrations are negligibly small for sufficiently high concentrations of ammonia. $\text{Ag}(\text{NH}_3)_2^+$ can be reduced by e_{sol}^- , via Equation (2.2), to form metallic Ag.



$\text{Ag}(\text{NH}_3)_2^+$ can also be reduced by H_2O_2 to produce Ag. In the case of an AgNO_3 solution in pure water this reduction mechanism is absent, and H_2O_2 is only an oxidizer of Ag.



This means that the use of a water-ammonia solvent leads to a role reversal for H_2O_2 from solely an oxidizer to a reducer as well as an oxidizer. Consumption of H_2O_2 in the reduction of $\text{Ag}(\text{NH}_3)_2^+$ leads to a decrease in the rate of Ag oxidation. Radiolysis of aqueous ammonia also creates additional chemical pathways that mediate Ag/ Ag^+ redox chemistry through the production of species such as NH_2^\bullet and the interaction of radiolysis species with NH_3 . Specifically, this leads to consumption of oxidizing species through the following reactions:



As a result, the concentration of species oxidizing Ag is significantly suppressed in a water-ammonia solvent in comparison to a pure water solvent, making the deposition environment more reducing.

1.5 Experiments

1.5.1 Experimental Sample Preparation

Solution for experiments was prepared using Silver Nitrate (Sigma Aldrich, ReagentPlus $\geq 99.0\%$ titration) and water (Fischer Chemical, HPLC grade). For a water-ammonia solvent, ammonium hydroxide solution (Sigma Aldrich, 25-30% NH_3) was used. Solutions were placed in QuantamiX WETSEM QX-102 capsules and irradiated with electron beams of different energies in an FEI Quanta 250 FEG scanning electron microscope.

The construction of the capsules ensures a sealed and stable environment, thereby preventing sample evaporation, liquid motion, and minimizing beam scattering during electron irradiation. Prior to exposure, the prepared solutions were carefully loaded into the capsules and sealed, ensuring minimal contamination and maintaining the chemical purity of the system. This setup captures the radiolytic processes and subsequent nanomaterial deposition, as it allows for precise control of the experimental conditions.

1.5.2 Deposition Results

Figure 2.2 shows the results of experiments for both water and water-ammonia. A central pillar deposit is formed at the point of irradiation in each case. A ring is formed around the central pillar only when the water-ammonia solvent is used (**Figure 2.2** (a-d)). The ring increases in diameter with increasing beam energy. Electron beams at 10 and 15 keV energy result in the formation of dendritic structures on the outer edge of the ring. The creation of these dendritic structures can be attributed to Mullins-Sekerka instabilities [63, 64].

The addition of ammonia to an aqueous solution increases the pH as well as introducing new chemistry. To distinguish between the impacts of these two effects, we also test a water solution with its pH elevated to match the water-ammonia solution. To determine whether the deposition behavior in water-ammonia solution is attributable to its high pH, a 1mM NaOH-water solution with pH 12 was irradiated with a 30 keV electron beam. Rings were not formed in pure water regardless of pH (**Figure 2.2 (e-f)**). This shows that the unusual deposition behavior in the water-ammonia solvent is not due to its elevated pH and requires an alternative explanation. Simulations of the coupled interplay between species transport and the local reaction rates provide a tool to uncover and define the dominant chemical interactions in space and time.

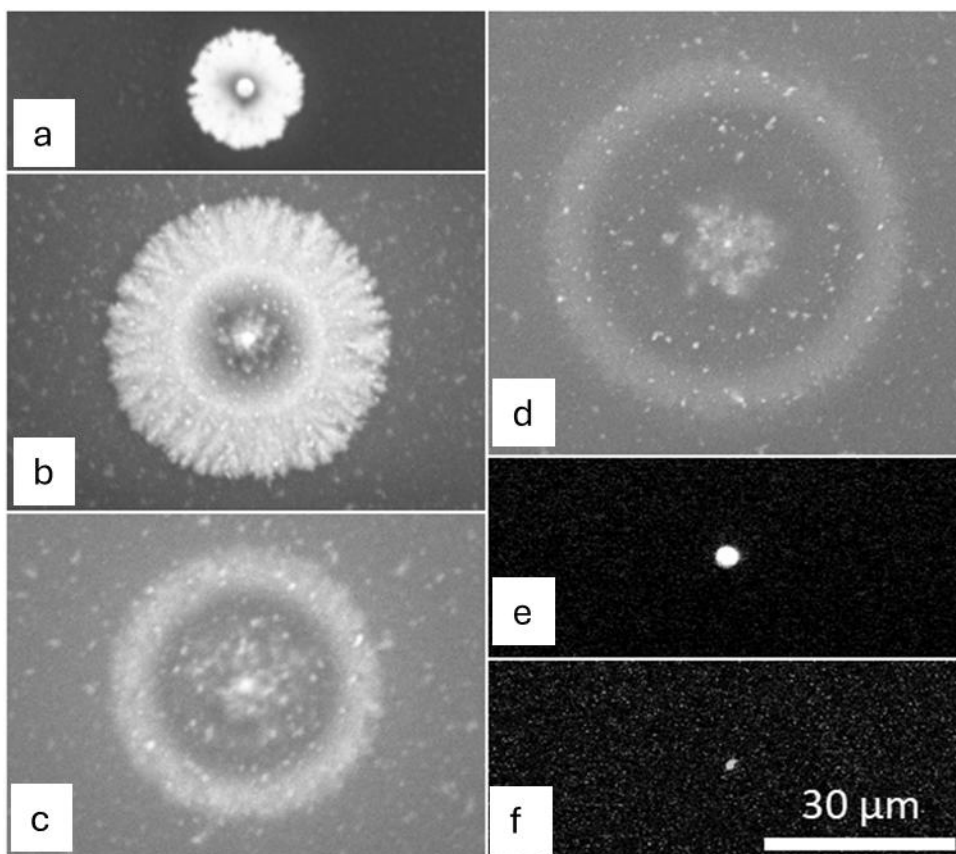


Figure 0.2 Deposition results. Deposition in “spot” mode, (a-d) 1 mM AgNO₃, 30% NH₃ aqueous solution, (e-f) 1mM AgNO₃ aqueous solution. (a) 10 keV, (b) 15 keV, (c) 20 keV, and (d) 30 keV beam energy. A central deposit and small ring are formed. Ring diameter increases with increasing beam energy. At 10 and 15 keV, dendritic structures are formed on ring. (e) 30 keV, neutral pH and (f) 30 keV, pH 12: Deposit created only at the irradiation site. Exposure time is 30 s for all cases. Imaging is performed with a 30 keV, 2 nA electron beam and an Everhart-Thornley secondary electron detector.

1.5.3 *Imaging-Induced Ag Growth*

It is known that imaging with the electron beam in scanning mode is capable of growing solid Ag deposits. However, growth caused by scanning mode imaging is uniformly distributed throughout the area impacted by the electron beam, so it cannot be responsible for producing either the pillar or ring deposits seen in our results. In **Figure 2.3** (a-d), we present images of deposits imaged immediately after deposition and after up to 60 s of continuous imaging under a 30 keV, 2 nA scanning electron beam. There is no noticeable difference caused in the morphology of deposits due to imagin.

After just 10 s (**Figure 2.4** (a)), a pronounced central feature is already established; by 20 s (**Figure 2.4** (b)), a faint peripheral ring begins to emerge, and at 30 s (**Figure 2.4** (c)) this ring becomes distinctly more prominent. These observations are in excellent agreement with our simulations, which predict that ring formation kinetics are significantly slower than those governing the initial central deposit. All imaging was performed in high vacuum mode with an Everhart-Thornley secondary electron (SE) detector. We see that deposition caused by imaging has little impact on the resultant images for our conditions.

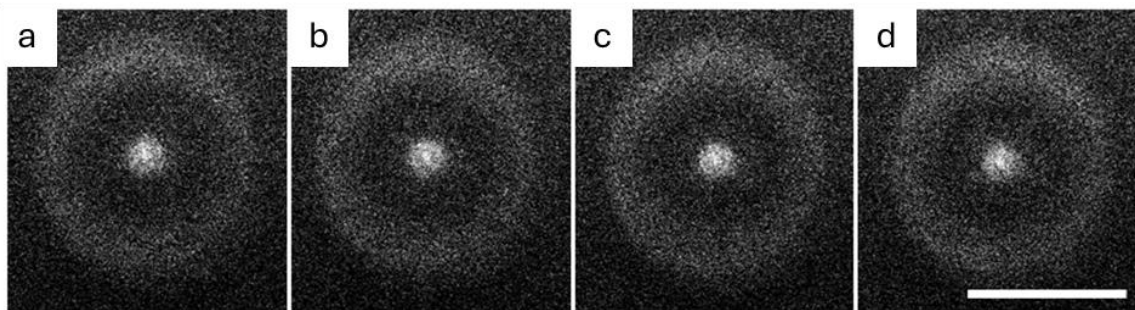


Figure 0.3. Comparison of deposits after (a) 5 s, (b) 23 s, (c) 38 s, and (d) 60 s of imaging exposure using a 30 keV, 2 nA scanning electron beam after deposition. Focused electron beam irradiation is 30 keV for 30 s in all cases. 1 mM $\text{Ag}(\text{NH}_3)_2^+$ in 30% NH_3 . Scale bar is 30 μm . Note that there is no noticeable difference in the deposits due to the imaging.

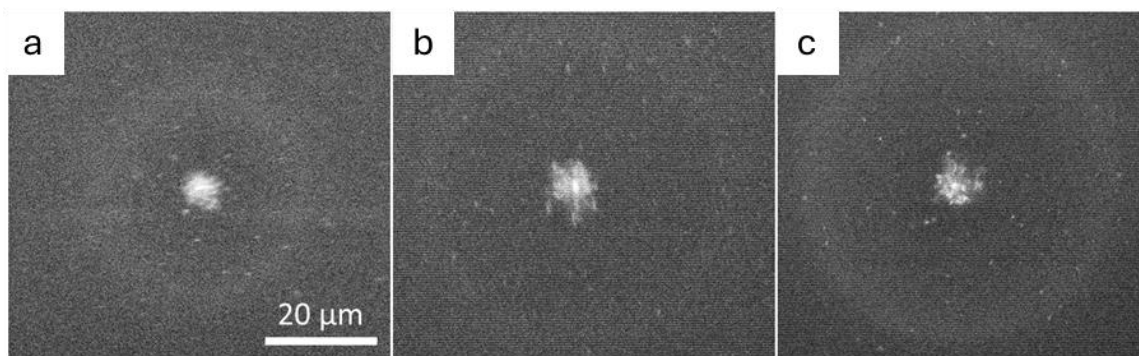


Figure 0.4. Comparison of deposits formed with (a) 10 s, (b) 20 s, and (c) 30 s of irradiation. A central deposit is already recognizable at 10 s. The ring is faintly visible at 20 s and more prominent at 30 s. This confirms our simulated results that ring formation occurs over time scales much longer than the central deposit.

1.6 Simulations

To unravel the chemistry driving silver deposition and the ring-shaped deposit morphologies, we employed a reaction-transport model reflecting the balance of reducing and oxidizing kinetics. Radiolytic species evolution under steady electron-beam irradiation and how ammonia's presence alters key reaction pathways are assessed. By comparing the theoretical predictions with experimental observations, we pinpoint the dominant mechanisms responsible for formation of both the central pillar and peripheral ring deposits.

1.6.1 Model Formulation

The kinetic model has been used to simulate the problem. [56] The reaction-diffusion equation for each relevant species is given by

$$\frac{\partial C_i}{\partial t} = D_i \nabla^2 C_i + \sum_{j,k \neq i} k_{jk} C_j C_k - \sum_j k_{ij} C_i C_j + R_i \quad (0.10)$$

where C_i is the concentration of i^{th} species, k_{ij} is reaction rate and R_i is the source term for creation of radiolysis species. We assume the medium remains stationary throughout the experiments and that temperature variations in the medium are small, so thermophysical properties of the domain will be uniform and constant.

The introduction of large numbers of charged particles (electrons and radiolysis products) raises the question of whether the motion of these particles will be influenced by electric fields. The estimated thickness of the Debye layer $\kappa^{-1} = (\epsilon \epsilon_0 k_b T / 2 \rho_\infty e^2)^{1/2}$ in a 1 mM aqueous solution of AgNO_3 is 10 nm, and the bulk solution outside of the Debye layer can

be considered electrically neutral [65]. The ion migration time $t_{mig} = (\rho / \kappa^2 n_c k_b T)^{1/2}$ governs the time scale over which the Debye layer is established, and for our conditions this time is 190 ns. Since these length and time scales are much shorter than the length and time scales over which species diffusion and deposition occur, electric fields are negligible in the bulk and electromigration effects can be ignored in the context of our experiments. Thus, no significant electroosmotic flow is expected in the capsule. This allows us to use the simple reaction-diffusion equation to model the system behavior.

A Monte Carlo simulation, whose results are exemplified in **Figure 2.6** (d), was used to model electron trajectories and energy loss within the domain. The combined electron energy loss per unit time due to collisions occurring within a cell defines the local dose rate (source term) in the transport equation for the reaction-diffusion simulations.

The number of electrons simulated was 45 million, yielding distribution of electrons and their energy within the simulated liquid-filled cell. In CASINO, the energy loss of an electron traveling through a sample is computed using the stopping power, which is expressed by a modified Bethe equation (Equation 2.11) that accounts for low-energy corrections.^[44] In general, the stopping power is written as:

$$\frac{dE}{dS} = -\frac{K\rho}{E_i} \sum_{j=1}^n \frac{C_j Z_j}{A_j} F_j \left(1.116 \left(\frac{E}{j} + k_j \right) \right) \quad (2.11)$$

Here, E is the electron energy, ρ is the density of the material, C_j is the weight fraction of element j, Z_j is the effective atomic number of element j, A_j is the atomic weight of element

j , F_j and k_j are factors that depend on Z_j , and J_j is the mean excitation potential of element j .

This relation underpins the calculation of inelastic energy losses between two elastic collision events. The energy loss dE/dS is calculated from the stopping power expression and is accumulated as the electron propagates through the sample. To convert the simulated energy deposition into an absolute dose rate (W/kg), we use the experimental electron beam current I_{beam} and the simulated Monte Carlo electrons N_{sim} to define a scaling factor f , using the elemental charge “e” as, $f = \frac{I_{\text{beam}}}{e N_{\text{sim}}}$. The CASINO output is reported in keV, which we convert to Joules using the conversion factor, $1 \text{ keV} = 1.602 \times 10^{-16} \text{ J}$. The mass of each cell of the grid m_{cell} is determined using the density of material ρ , and the volume of cells, V_{cell} , $m_{\text{cell}} \text{ (kg)} = \rho V_{\text{cell}}$. With energy deposited by electrons into each cell of the domain E_{cell} known via CASINO, the dose rate is then calculated by following expression.

$$\text{Dose Rate} \left(\frac{\text{J}}{\text{s} \cdot \text{kg}} \right) = \frac{E_{\text{cell}} \text{ (eV)} \times f \text{ (s}^{-1}\text{)} \times 1.602 \times 10^{-16}}{m_{\text{cell}} \text{ (kg)}} \quad (2.12)$$

If G-value that defines the radiolytic species created for energy deposited is known for species I, the rate of creation of species “i” is given by,

$$R_i \left(\frac{\text{mol}}{\text{m}^3 \cdot \text{s}} \right) = G_i \left(\frac{\text{mol}}{\text{J}} \right) \times \text{Dose Rate} \left(\frac{\text{J}}{\text{s} \cdot \text{kg}} \right) \times \rho \left(\frac{\text{kg}}{\text{m}^3} \right) \quad (2.13)$$

Here, G_i is the solvent-dependent G-value, which quantifies the moles of species i produced per unit energy absorbed from the electron beam.

The chemical equations, reaction rates, diffusivities, and G-values for radiolysis of DI water were taken from [56]. Reduction mechanisms for Ag^+ used are shown below. For all the following reactions the rate constants were obtained from the NIST Chemical Kinetics Database [66], except when specified.

Reducing species	Rate Constant $\text{M}^{-1}\text{s}^{-1}$
e_{sol}^-	4×10^{10}
H^\bullet	1.2×10^{10}

The mechanisms considered for reduction of $\text{Ag}(\text{NH}_3)_2^+$ are

Reducing species	Rate Constant $\text{M}^{-1}\text{s}^{-1}$
e_{sol}^-	3.2×10^{10}
H_2O_2	1×10^9

The oxidation mechanisms considered for Ag as

Oxidizing Agent	Rate Constant $M^{-1}s^{-1}$
O_2	5×10^9
OH^\bullet	5×10^9 *
H_2O_2	3.5×10^9

*estimated

The following additional pathways for water-ammonia system radiolysis were added.

Reaction	Rate Constant
$\text{Ag}^+ + 2\text{NH}_{3(\text{aq})} \rightleftharpoons \text{Ag}(\text{NH}_3)_2^+$	$K_{\text{eq}}=1.6 \times 10^7$
$\text{NH}_{3(\text{aq})} + \text{OH}^\bullet \rightarrow \text{NH}_2^\bullet + \text{H}_2\text{O}$	$9.7 \times 10^7 \text{ M}^{-1}\text{s}^{-1}$
$\text{NH}_2^\bullet + \text{OH}^\bullet \rightarrow \text{NH}_2\text{OH}$	$9.5 \times 10^9 \text{ M}^{-1}\text{s}^{-1}$
$\text{NH}_2^\bullet + \text{H}_2\text{O}_2 \rightarrow \text{NHOH} + \text{H}_2\text{O}$	$9 \times 10^7 \text{ M}^{-1}\text{s}^{-1}$
$\text{NH}_2^\bullet + \text{O}_{2(\text{aq})} \rightarrow \text{NH}_2\text{O}_2$	$9.8 \times 10^8 \text{ M}^{-1}\text{s}^{-1}$
$2\text{NH}_2^\bullet \rightarrow \text{N}_2\text{H}_4$	$2.2 \times 10^9 \text{ M}^{-1}\text{s}^{-1}$
$\text{OH}^\bullet + \text{N}_2\text{H}_4 \rightarrow \text{H}_2\text{O} + \text{N}_2\text{H}_3$	$1 \times 10^{10} \text{ M}^{-1}\text{s}^{-1}$

The G-values used for radiolysis species of aqueous-ammonia system were weight averaged with respect to the weight percentage of NH_3 in aqueous ammonia from G-values of pure water system. The problem was simulated in COMSOL using a transport of diffuse

species module. The dose rate source term was calculated *via* a Monte Carlo simulation using CASINO. This implementation uses the Joy and Luo [67] model for electron stopping power. The software calculates the total energy lost from all electrons passing through each cell of its mesh. We convert these values to a volumetric dose rate distribution and interpolate them onto the COMSOL mesh.

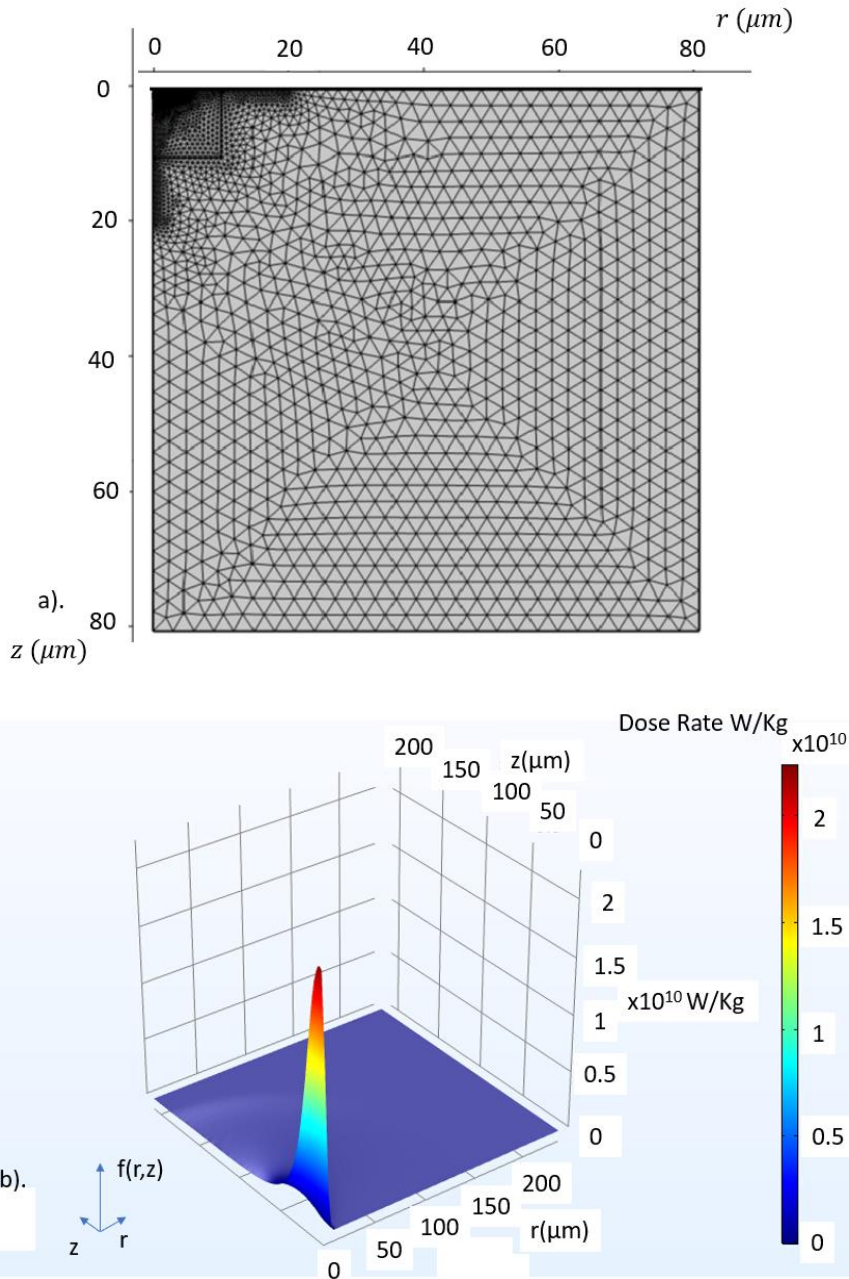


Figure 0.5 (a) Mesh on an axisymmetric domain in COMSOL, electron beam is focused at $r = 0, z = 0$. (b) Dose rate extracted from CASINO for interpolation onto COMSOL mesh for a 30 keV electron beam.

1.6.2 Theoretical Predictions

We model the processes in a 2D axisymmetric domain (**Figure 2.5 (a)**) and solve reaction-diffusion equations (Equation 2.10) for 1mM AgNO₃ in pure water and water-ammonia solvents. The rate constants incorporated in the simulation are taken from [56, 66]. The creation of radiolysis species, their reactions, and transport have been predicted to simulate Ag formation *via* the net effects of reduction and oxidation pathways, as shown in **Figure 2.1**. An electron beam enters the solution through an electron-transparent polyimide membrane. Electrons then undergo a series of elastic and inelastic collisions with molecules in the solution, triggering a process of radiolysis. The extent of the electron beam penetration in the solution depends on the energy and determines the region in which radiolysis takes place. **Figure 2.6 (a-c)**, presented at the same scale, shows the spatial distribution of dose rate for electron beams at 30, 15, and 10 keV energies, respectively. The concentration of radiolysis species is a function of the spatial dose rate and irradiation time. A change in electron energies impacts the spatial and temporal concentrations of radiolysis species, resulting in significant changes in deposition outcomes. **Figure 2.6 (d)** shows the trajectories of electron inside water, for a 30 keV electron beam extracted via Monte Carlo simulation.

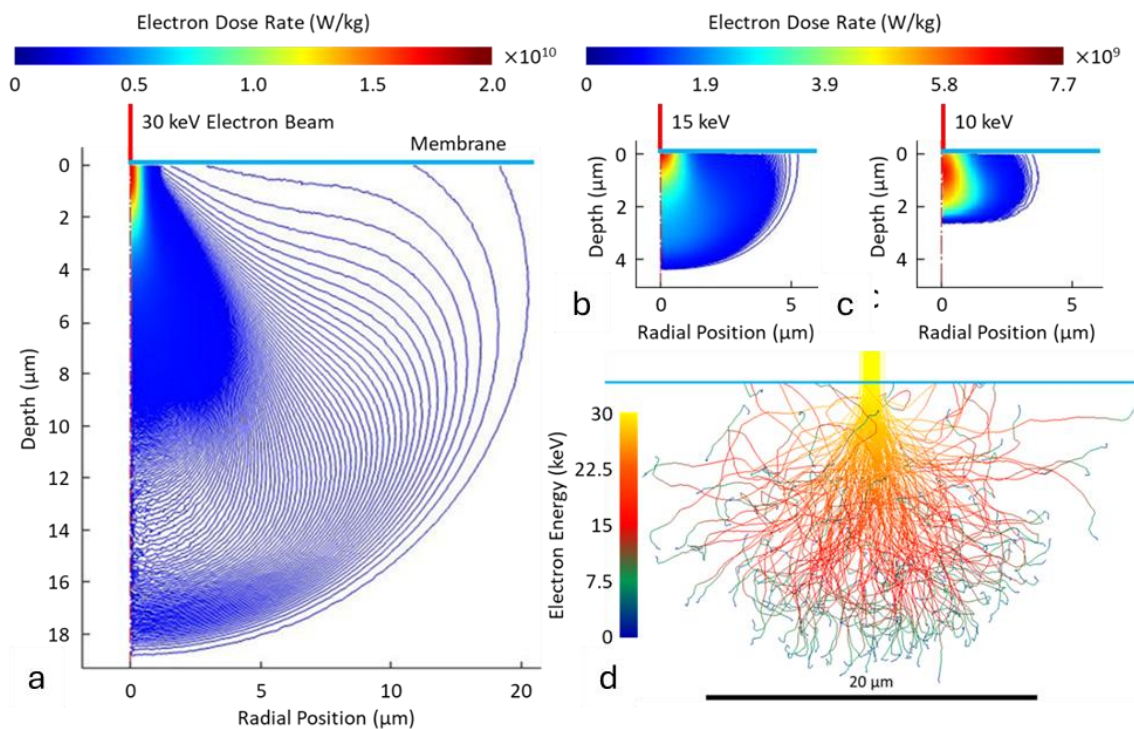


Figure 0.6 Electron beam dose rates. The spatial distribution of dose rate is a function of electron beam energy, with a higher beam energy resulting in a larger region of interaction. 2D-axisymmetric plots of dose rate for beam energies of (a) 30 keV, (b) 15 keV, and (c) 10 keV in 30% NH_3 aqueous solution. (d) Electron trajectories extracted from a Monte-Carlo simulation (30 keV shown) used to calculate dose rates.

Figure 2.7 (a) depicts dose rate variation in the water-ammonia solution at the membrane, where experimental results are obtained (**Figure 2.2**). The radial distribution of the electron dose rate displays three domains—a large peak in the dose rate where the primary electron beam enters the domain (the *beam* region), an extended region of nearly uniform dose rate (the *envelope* region), and a far field region with negligible dose rate. The boundaries between these domains give two length scales important to explaining the experimental results. (For a 30 keV beam, these two length scales are ca. 1 μm and 18 μm , respectively, **Figure 2.7** (a)).

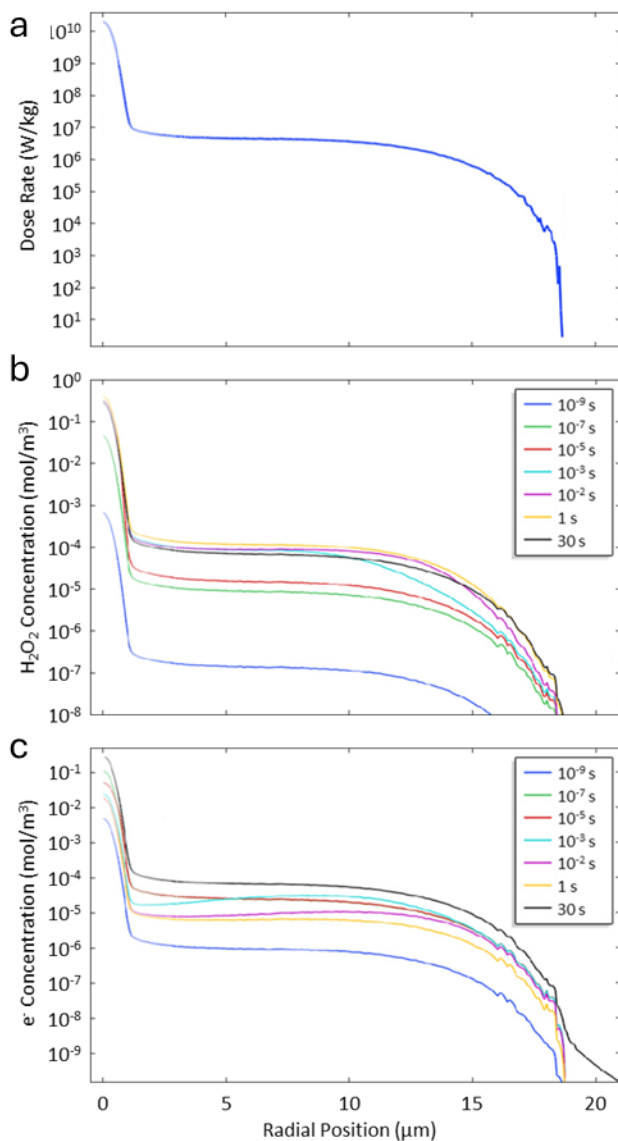


Figure 0.7 E-Beam Irradiation of Water-Ammonia. (a) Dose rate distribution at the membrane for a 30 keV electron beam in 30% aqueous solution. There are two length scales of interest. The first is associated with the region directly irradiated by the electron beam and the second with the extent of electron penetration inside the solution. (b) The concentration profile of H_2O_2 initially follows the dose rate profile. In the beam region, a quasi-steady state concentration is achieved by 10^{-5} s. After attaining its quasi-steady state

concentration in the beam region. H_2O_2 continues diffusing into the envelope region, where it reaches a quasi-steady state concentration by around 1 s. (c) The concentration of e_{sol}^- increases at short times and these high concentrations drive the creation of a central pillar. After 10^{-7} s the concentration of e_{sol}^- in the beam region begins falling.

Figure 2.7 (b-c) shows the spatial and temporal variation in concentration at the membrane of the two most important species for producing Ag: H_2O_2 and e_{sol}^- . On the smaller length scale of the beam region, the H_2O_2 concentration reaches quasi-steady state at approximately 10^{-5} s. In the envelope region, its concentration continues increasing for much longer before reaching a quasi-steady state around 1 s. **Figure 2.7** (c) shows the behavior for e_{sol}^- . Its concentration continually evolves throughout the entire process. The e_{sol}^- concentration in the beam region initially peaks and then falls before increasing again. This lack of quasi-steady state behavior is due to the consumption of e_{sol}^- through secondary radiolysis species which are created on much longer timescales than e_{sol}^- .

To better demonstrate the importance of these length and timescales, the reaction rates for the two key pathways involved in the reduction of $\text{Ag}(\text{NH}_3)_2^+$ in water-ammonia are plotted for a 30 keV beam in **Figure 2.8** (a). $\text{Ag}(\text{NH}_3)_2^+$ is reduced by e_{sol}^- via Equation (2.2) and H_2O_2 via Equation (2.3). The pathways reducing Ag^+ are negligible due to the almost complete conversion of Ag^+ into $\text{Ag}(\text{NH}_3)_2^+$. Initially, e_{sol}^- is the primary reducer of $\text{Ag}(\text{NH}_3)_2^+$ (10^{-7} s, **Figure 2.8** (a)), but this behavior inverts at longer times and reduction by H_2O_2 becomes dominant in the quasi-steady state condition (1-30 s, **Figure 2.8** (a)). **Figure 2.8** (b-c) shows the net Ag creation rate by all mechanisms over time for the water-ammonia and pure water solvents, respectively. In both media we see the presence of a large peak in the beam region, indicating very high rates of net Ag creation. Since e_{sol}^- is the dominant reducing species at very short times, we conclude that the central pillar is produced primarily from Ag^+ (in water) or $\text{Ag}(\text{NH}_3)_2^+$ (in water-ammonia) reduction by e_{sol}^- .

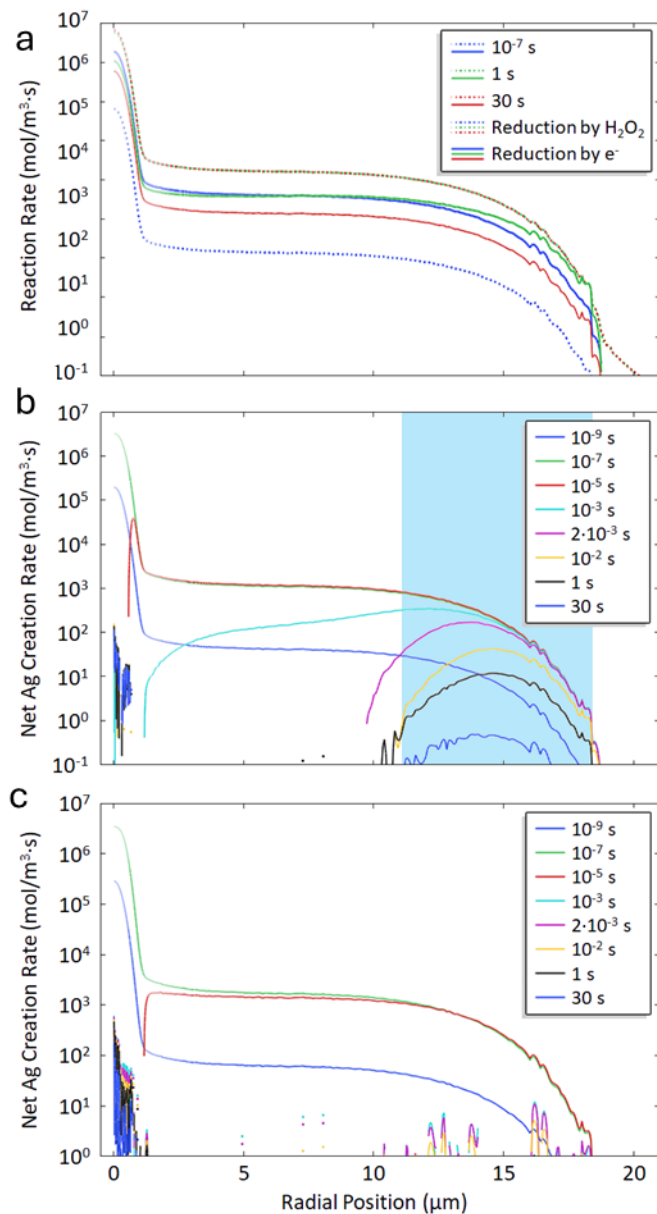


Figure 0.8 Water and Water-Ammonia Deposition Outcomes. (a) Comparison of most important reduction pathways in the creation of Ag in a 30% aqueous solution. At short times, reduction of $\text{Ag}(\text{NH}_3)_2^+$ by e_{sol}^- is dominant, but H_2O_2 becomes dominant at longer times. (b) Net rate of Ag creation at membrane by all pathways in a 30% NH_3 aqueous solution. Two distinct regions of production are seen—one at the center before 10^{-5} s, and one around 15 μm which persists until times >1 s. The shading highlights the region where

ring formation is predicted to occur. (c) Net rate of Ag creation at membrane by all pathways in a purely aqueous solution. No production occurs in the bulk beyond 10^{-5} s. A 30 keV electron beam and 1 mM AgNO_3 are used for all cases.

Outside the beam region, the behaviors of the two solvents significantly diverge. In the pure water system, the net Ag creation rate falls to negligible or negative (oxidizing) values in the entire envelope region. In the water-ammonia system, we see the establishment of a band with well-defined inner and outer edges where the environment remains net-reducing. This can be explained through the interaction of reaction and transport effects. Because the dose rate is highest near the center of the domain, the reducing and oxidizing radiolysis species tend to diffuse outward from the beam region. Consumption of the initial $\text{Ag}(\text{NH}_3)_2^+$ supply in the envelope region causes $\text{Ag}(\text{NH}_3)_2^+$ to diffuse inward from the bulk. These opposing species fluxes interact near the edge of the envelope region, and due to the water-ammonia solvent, the radiolysis species produce a net-reducing effect. This shows that the ring is formed over longer timescales and, as shown in Figure 2.8 (a), H_2O_2 is primarily responsible for its creation, in contrast to the central pillar, which is driven by e_{sol}^- .

Figure 2.9 compares the concentrations of the two main oxidizing species, OH^\bullet and O_2 , in both the pure water and water-ammonia solvents. This demonstrates the effect described schematically in **Figure 2.1**, as NH_3 and NH_2^\bullet scavenge these oxidizing species in the water-ammonia system, suppressing their concentrations compared to the pure water system. This action is key in enabling the reduction of $\text{Ag}(\text{NH}_3)_2^+$ by H_2O_2 away from the beam region, leading to the ring formation observed in experiments.

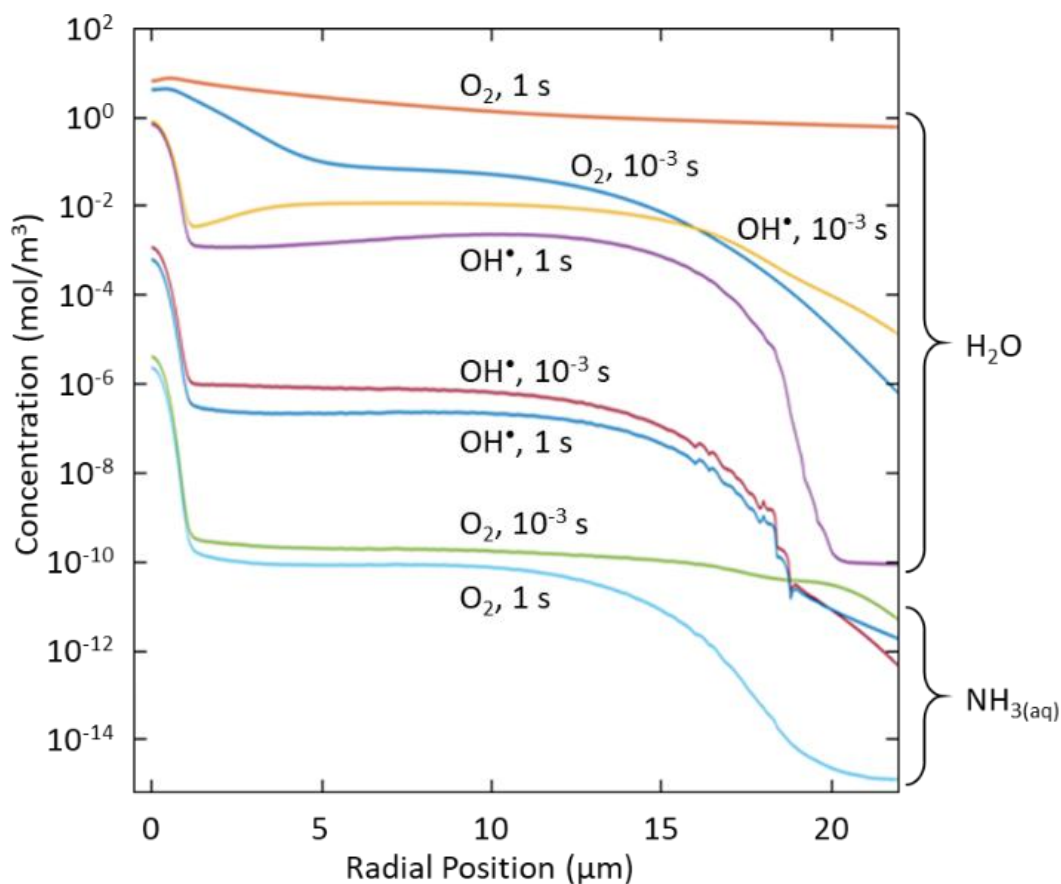


Figure 0.9 Suppression of Oxidizing Species by Ammonia. Concentrations of OH* and O₂ are suppressed in water-ammonia in comparison to pure water due to their scavenging by NH₂* and NH₃. This creates a highly reducing environment, promoting Ag nanomaterial synthesis in the water-ammonia solution.

The physics of the process are three-dimensional. **Figure 2.10** shows a simulation of the net rate of Ag production at 1 s in water-ammonia for a 30 keV beam. The region where Ag is produced at quasi-steady state forms a hemispherical shell. The ring seen in the experimental results of **Figure 2.2** is the manifestation of this shell at the membrane, which acts as a preferential surface for nucleation. However, the rate of Ag production on the shell is highest in the bulk, away from the membrane. This is attributable to the electrons' greater penetration in the axial direction compared to radially, as shown in the teardrop profile the of dose rate in **Figure 2.6** (a). This insight is critical for procedures involving the generation of Ag nanoparticles *via* electron beam interaction, as the region of greatest Ag formation occurs in the bulk solution. creation of a 2D ring as observed in experiments rather than a 3D shell seen in simulations for the water-ammonia system.

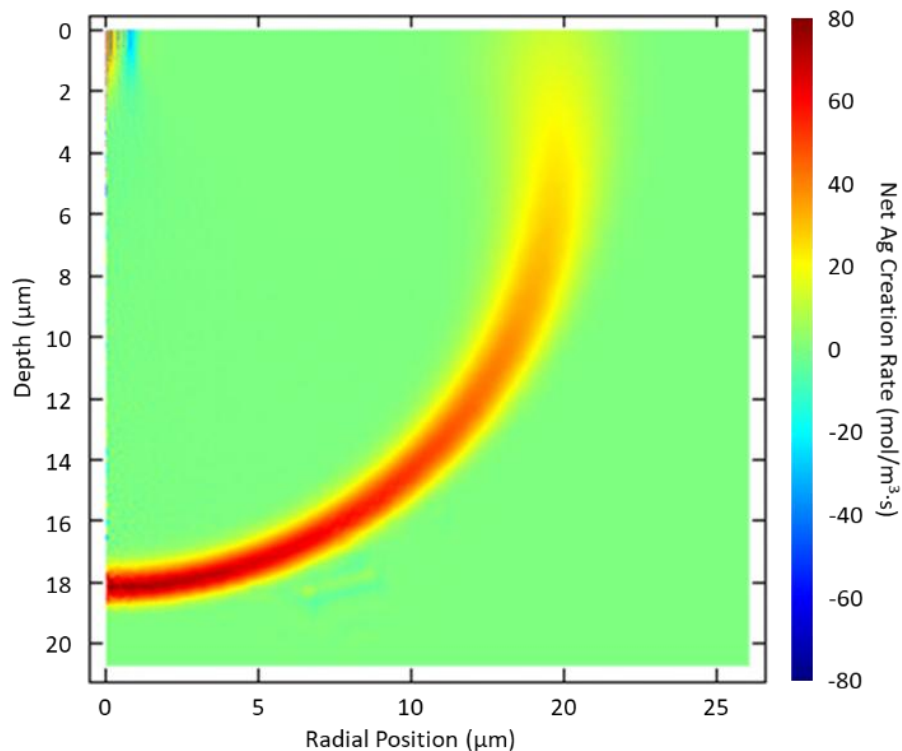


Figure 0.10 Regions of Ag Production in Water-Ammonia. Net rate of creation of Ag (difference between reduction and oxidation rates) with irradiation of a 1mM AgNO₃, 30% NH₃ aqueous solution by a 30 keV electron beam at 1 s shown in a 2D axisymmetric domain. There is a positive rate of Ag production at the point of irradiation and in an approximately hemispherical region of the bulk. The small region of a negative creation rate indicates that at this instant and this location, Ag is being consumed by oxidation at a greater rate than it is being produced by reduction of Ag⁺ or Ag(NH₃)₂⁺. In a water system, only the central deposition region of high net Ag production rate is present. The membrane surface provides a preferential location for solid phase nucleation, which manifests in the creation of a 2D ring as observed in experiments rather than a 3D shell seen in simulations for the water-ammonia system.

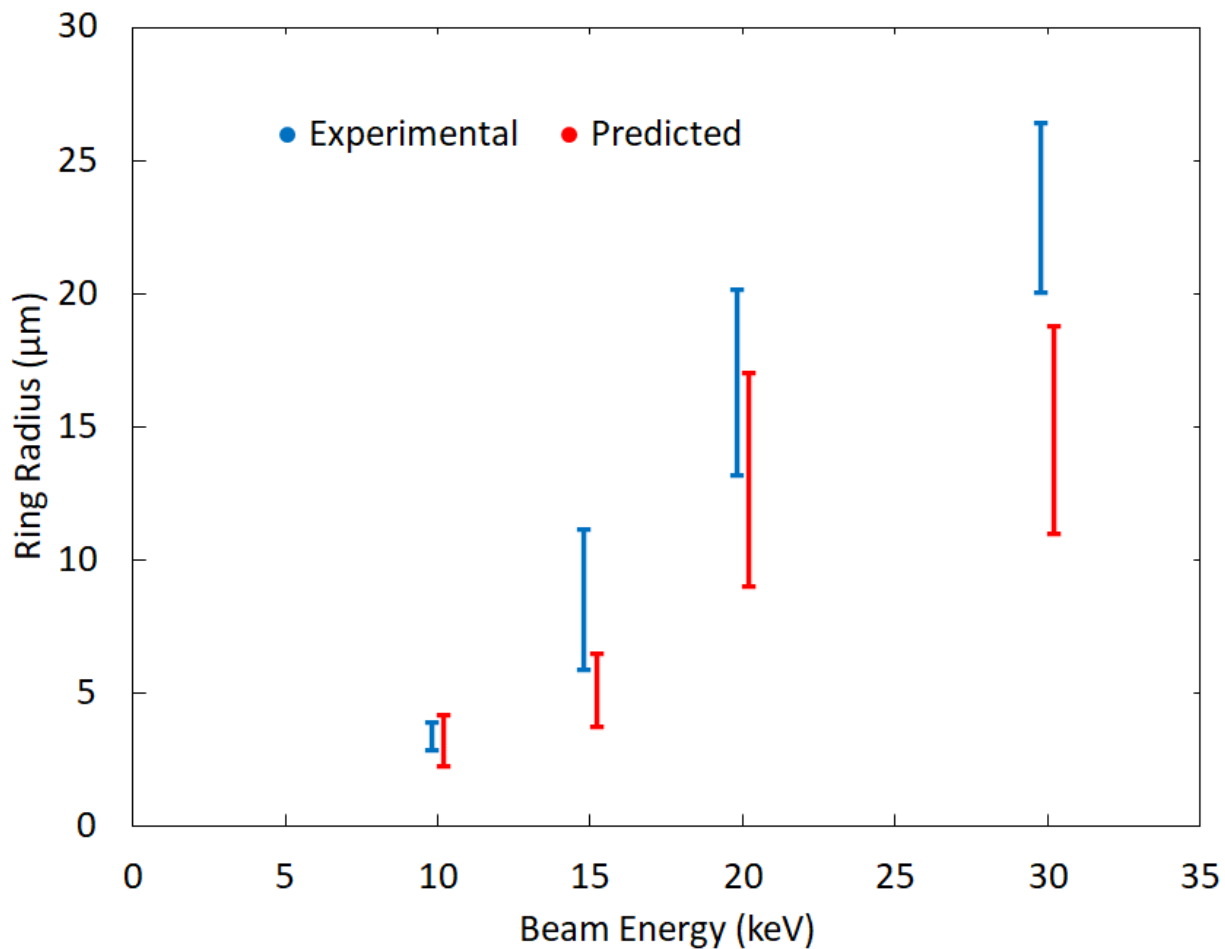


Figure 0.11 Experimental and Computational Ring Sizes. Comparison between the experimental observations for the inner and outer diameters of rings and predictions of ring sizes from simulations of the water-ammonia system. For simulated results, the ranges represent the estimated minimum and maximum radii at which the net rate of solid Ag creation exceeds a nominal value— $1 \text{ mol/m}^3\cdot\text{s}$ —at times of 10 ms or greater. This represents the range of positions over which ring deposition is predicted to occur. The size of the ring grows as the beam energy increases. The disagreement arises from the overprediction of stopping power at low electron energies by the Joy-Luo stopping power model used in the simulations.

The simulation allows us to predict the expected ring size. As electron energy increases, the region of electron penetration expands further into the bulk. This results in the creation of rings with larger radii. **Figure 2.11** compares the estimated ring locations from simulations to the experimentally measured values (**Figure 2.2**). The model correctly predicts the energy-dependence of the ring size. An underprediction of ring size is present, which can largely be attributed to three effects. The first is the electron dose rate distribution. The electron stopping power model available in our Monte Carlo simulation software is known to overpredict electron stopping power [68]. The second is that we neglect heating by the electron beam (see **section 2.3.3**) and convection in the reaction-diffusion simulation. Scaling analysis combined with thermal simulations suggest the mass diffusion Peclet number, Pe , is at most $O(1)$ for the system, meaning thermally induced flow, which would be radially outward from the beam impingement point near the membrane, may have some effect on species distributions [69]. Both an underprediction of electron transport distance and neglect of species advection would result in an underprediction of ring sizes, especially at higher beam energies. Lastly, the electron beam interaction with the membrane introduces a radial electric field [70, 71] that could drive electrokinetic flow in the fluid near the membrane surface. If this flow is of sufficient velocity, this would result in changes in species concentration profiles and therefore deposition rates with implications for the observed ring locations. Further, to achieve complete quantitative agreement between simulation and experiments, one would also need to account for heterogeneous nucleation and solid phase formation and motion, which require multiphase simulations. In this work, our focus is on identifying the dominant

mechanisms which allow one to explain the interplay between reaction chemistry and species transport, allowing us to correctly predict the trend in experimental behavior.

1.6.3 Consideration of Thermal Effects

We have investigated the potential effects of heating by the electron beam. As a limiting case, we consider the scenario in which all the beam energy is converted into thermal energy in the solution, using the calculated dose rate distribution as a volumetric heat generation term. We calculate a maximum temperature rise of 13° C above far field values at the hottest point after 30 s of irradiation. The simulated temperature profile in the domain after 30 s of irradiation with a 30 keV electron beam is shown in **Figure 2.12**.

There are two main means by which temperature changes can affect the system—changes in thermophysical properties of the solution and buoyancy-driven convective flows in the domain. Diffusion coefficients in liquids are linearly proportional to absolute temperature. We investigated the impact of this temperature change on the diffusion coefficients of the dissolved species, which are linearly dependent on absolute temperature, and found that a corresponding increase in diffusion coefficients makes no discernible difference in the predicted ring positions.

For convective effects, we use scaling analysis and thermal simulations to determine whether thermally induced flows may have an effect on species distributions. Thermally induced flows in this configuration would move radially outward from the beam impingement point near the membrane surface and upward from below in the center. The mass diffusion Peclet number, Pe , compares the influence of species advection and to

diffusion within our system. Bejan [69] the Rayleigh number, $Ra = g\beta\Delta TL^3/\nu\alpha$, and Prandtl number are related by, $Pe = \alpha/D(Ra)^{\frac{1}{2}}$.

Where g is the gravitational acceleration, β is the coefficient of thermal expansion, ΔT is the driving temperature difference, L is the length scale across which the temperature difference acts, ν is the kinematic viscosity of the fluid, and α is the thermal diffusivity of the fluid. For our conditions with a 30 keV beam and taking a characteristic length scale of 10 μm , we find Pe is no larger than $O(1)$, which means advective effects are potentially of similar magnitude to diffusive effects. This effect may explain much of the discrepancy we see between predicted and observed results at higher beam energies (**Figure 2.11**), as advection transports reacting species away from the beam impingement point and allows the formation of larger rings.

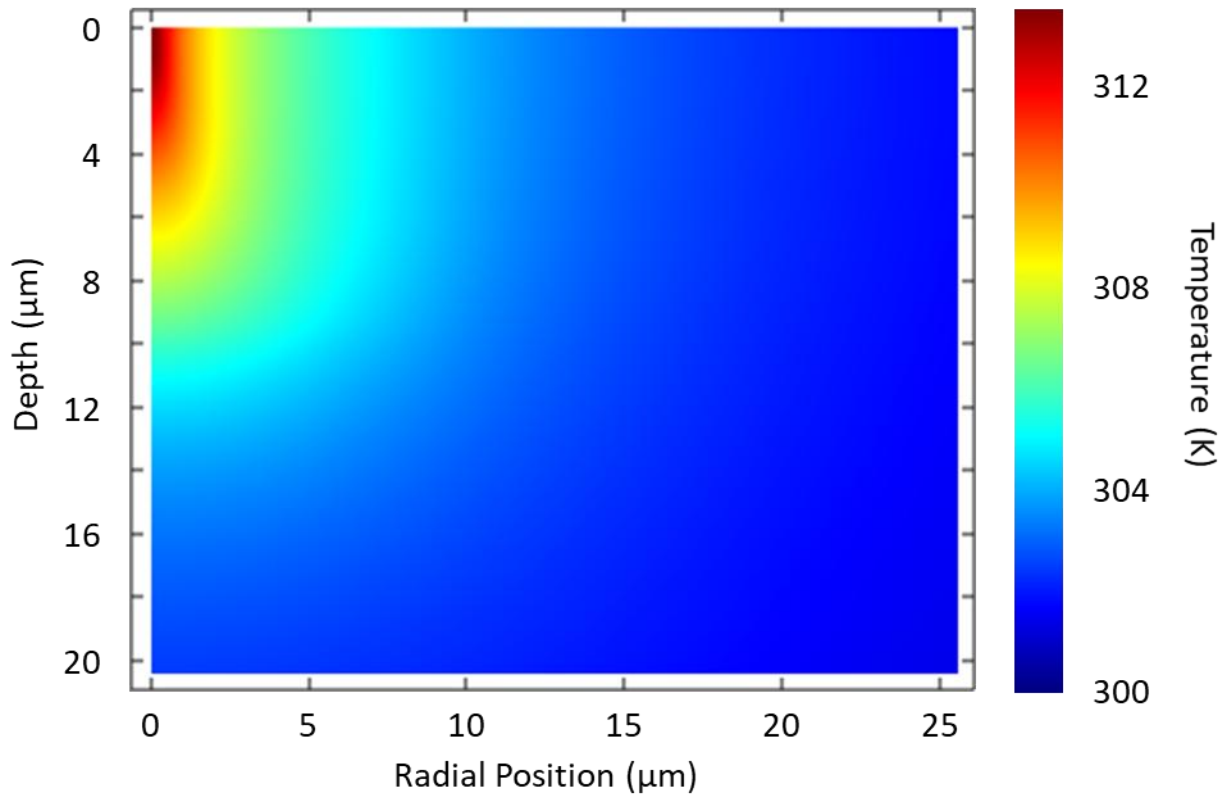


Figure 0.12 Temperature in aqueous environment after 30 s of heating with a 30 keV, 2 nA electron beam. All electron beam energy is assumed to be converted into thermal energy, using a volumetric heat generation rate equal to the spatial dose rate of electron energy loss shown in Figure 2.5 (b).

1.6.4 Time Evolution of Deposition Rates

While points near the central deposit do see very large reaction/net creation (reduction minus oxidation) rates in the water-ammonia simulations, these persist for only very short times. Although the net Ag creation rate at larger radial positions never reaches values as high as those closer to the center, they remain appreciable for much longer. The total amount of deposition at a point is the integral of the net creation rate at that point over the entire exposure time, and our simulation shows that total deposition values in the ring region are two orders of magnitude higher than in the intermediate region (between the pillar and ring) after 30 s of irradiation. This is immediately clear in examining **Figure 2.13**, which compares the net creation rates over time for two radial positions in the 30 keV beam simulation. Almost instantaneously, the net creation rate reaches its maximum at both positions and begins to decay. The rate at the 7 μm radial position is initially higher but falls below that of the 14 μm position in less than 1 ms. At 7 μm , the rate remains negligible for nearly the entirety of the 30 s irradiation time, while at 14 μm , the rate reaches 10 $\text{mol}/\text{m}^3\cdot\text{s}$ within about 1 s and gradually decays to near zero over tens of seconds. It is the slower creation of solid Ag over this time scale that is responsible for the creation of the ring.

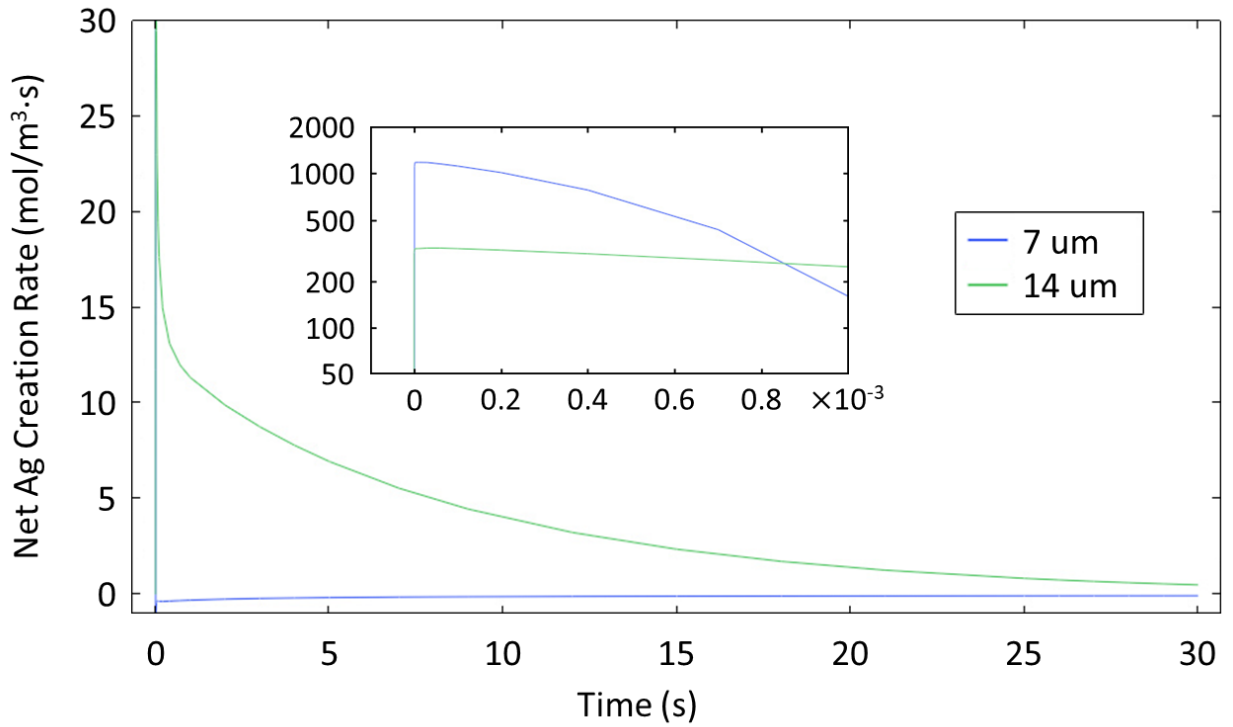


Figure 0.13 Comparison of net Ag creation rates at radial positions $r = 7 \mu\text{m}$, in the intermediate region between the central pillar and the ring, and $r = 14 \mu\text{m}$, at the ring location, in a 30 keV beam simulation in water-ammonia. Note that the rate at $7 \mu\text{m}$ falls off to near zero within milliseconds, while at $14 \mu\text{m}$ it is appreciable for much longer times.

1.7 Concluding Remarks

We discovered the unique behavior of electron beam-induced metal deposition in water-ammonia systems. The mechanisms of radiolytic redox interplay in silver formation from its metal salt solutions are defined through first-principles simulations and supporting experiments. In water-ammonia systems, complex deposition morphologies are observed, with a secondary zone of deposition (ring) created in addition to a commonly observed central pillar at the point of electron beam irradiation. This outcome is attributed to the suppression of oxidizing species in the water-ammonia system *via* scavenging and the addition of a reduction pathway involving H_2O_2 . Simulations highlight the importance of interactions between the dominant reaction pathways and radiolysis species transport for experimentally observed behavior. They show that the central pillar deposition occurs over timescales on the order of microseconds and solvated electrons are the dominant reducing species at this timescale. The ring creation is defined by the extent of the electron penetration region. The dominant reducing species is found to be H_2O_2 for this process, which occurs on a timescale dictated by the diffusion time of reducing species transport towards the edge of the electron penetration region. We also show that the expected region of net positive Ag production in the water-ammonia solvent forms a three-dimensional nearly hemispherical region in the quasi-steady state condition. Due to heterogeneous nucleation at the solution-membrane interface, this is manifested experimentally as a ring attached to the membrane. The proposed model of the process could be further enhanced by accounting for the dependence of radiolysis species generation on electron energies, using an electron stopping power model that is more accurate for our range of energies, modeling the kinetics of heterogeneous reactions, solid phase transport within the liquid

deposition domain, and the solid phase's impact on the dose rate distribution, and considering the effects of buoyancy induced convection on species distributions.

Overall, this chapter establishes that ammonia's ability to extend the reducing environment and suppress oxidation fundamentally changes deposit morphology (central pillars with extended rings). These insights lay the groundwork for Chapter 3, where we harness ammonia's redox-modulating capability to establish the concept of an "electrochemical lensing".

ELECTROCHEMICAL LENSING FOR HIGH-RESOLUTION NANOSTRUCTURE SYNTHESIS

1.8 Introduction

Building on the insights from Chapter 2 regarding ammonia-induced modulation of silver deposition, we now examine a broader principle that exploits this redox phenomenon and introduce the concept of “electrochemical lensing.” The central premise is to create a highly reducing environment at the electron-beam focal spot while maintaining an oxidizing farfield. Such a ‘lens’ amplifies the desired growth at the e-beam focal point, while suppressing unwanted deposition in the far field, leading to rapid and high-resolution nanostructure growth. In this chapter, we establish the theoretical underpinning of electrochemical lensing and validate it through experiments, thereby introducing a new paradigm for accelerating growth rates without sacrificing spatial precision.

The addition of ammonia to an aqueous solution has been shown to promote nanomaterial synthesis due to its ability to make the chemical environment more reducing [36]. The presence of ammonia in water leads to an environment around the primary e-beam irradiation site that is highly reducing for metal cations (favorable for electrochemically induced metal deposition) due to (a) the switching of the behavior of the radiolytically generated hydrogen peroxide from purely oxidizing to dual reducing/oxidizing, and (b) locally depressed concentrations of short-lived oxidizing species from radiolysis consumed by NH_3 and NH_2^\bullet that act as scavengers of oxidizing species [36]. However, high ammonia concentrations can also lead to fast growth of unwanted co-deposits away from the desired

nanostructure formation location. Controlling the spatial distribution of the solid matter deposited in and around the primary electron beam irradiation site is mediated by the species transport and is crucial for achieving high resolution in electron beam nanostructure synthesis for direct-write applications.

A promising strategy in spatial control of electron beam guided synthesis is to take advantage of a water-ammonia solvent that creates a reducing radiolysis environment in the immediate vicinity of primary electron beam impingement, i.e., the location of high electron dose rate (the “near-field” region). At the same time, an oxidizing environment (such as that present when pure water is the solvent) could be established outside of the primary beam impingement site or the “far-field” region. Exploiting the interplay between the redox species transport and reactions in this dual-domain environment enables an 'electrochemical lensing' effect, where the growth of nanostructures is precisely 'focused' and amplified at the near-field, while unwanted growth in the far-field is suppressed.

Uncovering and quantifying the interplay between the reaction and transport of chemical species that yields the electrochemical lensing phenomenon is the focus of this chapter, which is organized as follows. First, NESA-FEBID synthesis is described, focusing on the physicochemical state of the unconfined liquid film exposed to vacuum. Then we describe relevant chemical pathways taking place in the ammonia-water solution with dissolved silver nitrate precursor during electron beam irradiation. A reaction-transport model is presented and insights from simulations are used to reveal the mechanisms resulting in the desired electrochemical lensing effect. Finally, the results of simulation are validated using corroborating experiments and generalized to broader conclusions relevant to other electrochemical synthesis methods.

1.8.1 FEBID Synthesis in NESAs Films

We use a NESAs-FEBID process with ammonia-water as solvent and dissolved silver nitrate (AgNO_3) salt as a source of cations for Ag deposition. The presence of ammonia in the solution leads to a rapid equilibrium between Ag^+ ions and silver diamine ion complexes, $\text{Ag}(\text{NH}_3)_2^+$, Equation (3.1), which favors greater $\text{Ag}(\text{NH}_3)_2^+$ concentrations with increasing ammonia content.



In NESAs-FEBID, **Figure 3.1**, irradiation of the liquid film by the electron beam results in radiolytic production of chemically reactive species. High energy electrons undergo elastic and inelastic collisions with the solvent molecules. This results in a transfer of energy from the electron beam to the liquid and leads to radiolysis, resulting in the creation of primary radiolytic species such as solvated electrons, e_{sol}^- , as well as H^\bullet , H_2O_2 , H_3O^+ , OH^\bullet , HO_2^\bullet , NH_2^\bullet and H_2 [56, 72, 73]. These primary radiolytic species then undergo reactions with each other and the solution, leading to the creation of secondary radiolytic species such as O_2 and N_2H_4 [36, 62]. Both primary and secondary radiolytic species diffuse away from their region of formation to react with the precursor, the solvent, and one another both in the near-field and far-field regions of the film.

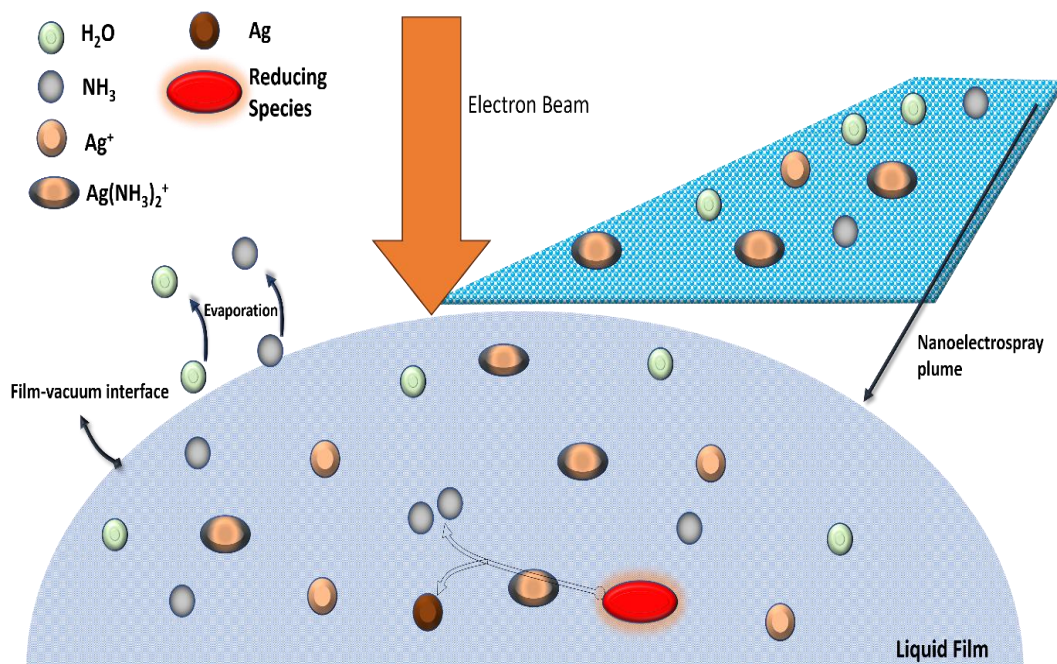


Figure 0.1. The solution of water and ammonia as solvent containing Ag^+ and $\text{Ag}(\text{NH}_3)_2^+$ precursor is nanoelectrosprayed onto the substrate and forms a film. As the solution is supplied to the substrate, the film size increases. Water and ammonia evaporate from the film surface slowing the growth of the film. The film reaches a quasi-steady state size and ammonia concentration as the evaporation balances the addition of solution via nanoelectrospray. The concentrations of non-volatile Ag^+ and $\text{Ag}(\text{NH}_3)_2^+$ precursors increase continuously (i.e., do not achieve a steady state value). The presence of $\text{Ag}(\text{NH}_3)_2^+$ provides an additional source of stored ammonia, as a single $\text{Ag}(\text{NH}_3)_2^+$ ion-complex releases two ammonia molecules if reduced to Ag.

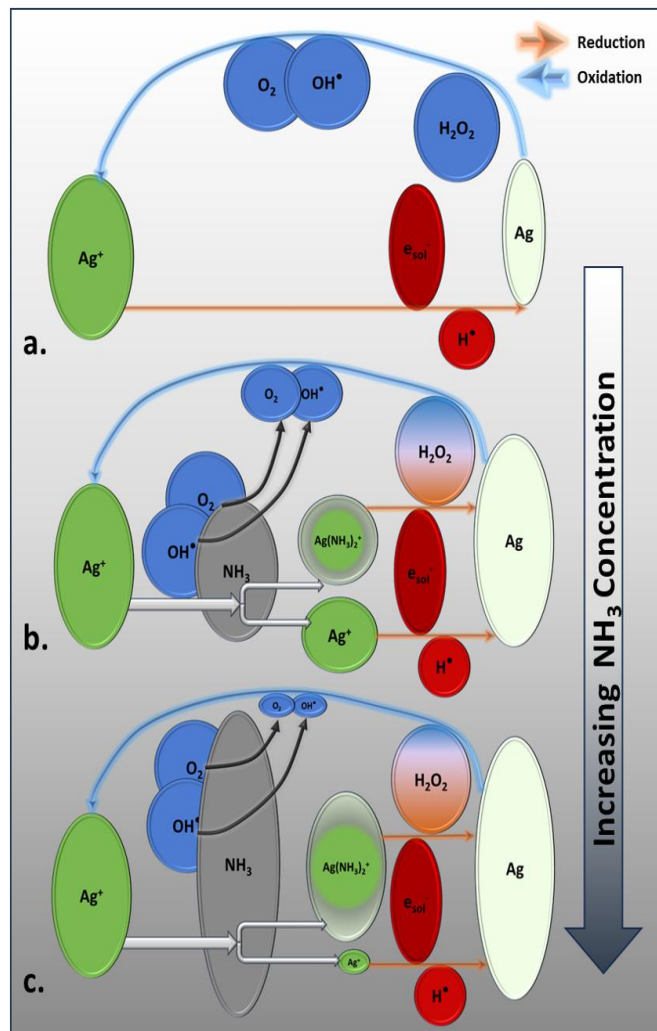


Figure 0.2 Important chemical pathways for silver production in LP-FEBID with an ammonia-water solvent and metal salt precursors (shown in green). The reducing species are illustrated in red and oxidizing species in blue. In the absence of NH₃ (a), the precursor Ag⁺ is converted to Ag via reduction by solvated electrons. The Ag can then be reverted to Ag⁺ via oxidation. The addition of ammonia to the solution (b) leads to partial conversion of Ag⁺ to Ag(NH₃)₂⁺. This adds an additional silver formation pathway as Ag(NH₃)₂⁺ can be reduced to Ag by H₂O₂. The role of H₂O₂ is shifted from purely an oxidizer of Ag to both an oxidizer and reducer. Presence of NH₃ also depletes the concentrations of oxidizing species O₂ and OH[•], making the environment more reducing. Further addition of NH₃ (c) amplifies this effect, leading to the environment becoming even more reducing. The size of each species

1.8.2 Reaction Pathways Essential to Nanomaterial Synthesis

In NESAFEBID of AgNO₃/ammonia-water, silver metal formation occurs through the reactions shown in **Figure 3.2**, which highlights the impact of changing ammonia concentration. In an environment where pure water serves as the solvent (**Figure 3.2 (a)**), an overall oxidative condition prevails, which significantly inhibits the rapid growth of nanomaterials. The species of greatest significance for synthesis of Ag nanomaterials are the ones that either reduce Ag⁺ and Ag(NH₃)₂⁺ to Ag or oxidize Ag to Ag⁺. In the absence of NH₃, the Ag⁺ from dissociated AgNO₃ is reduced to Ag by solvated electrons e_{sol}⁻ and hydrogen radicals H[•]. The Ag formed can then be converted back to Ag⁺ by oxidizing species, H₂O₂, OH[•] and O₂ [74]. The net rate of Ag creation is determined by the difference in rates of silver cation reduction and silver atom (solid phase) oxidation (**Figure 3.2 (a)**). The introduction of ammonia changes the deposition landscape in multiple ways (**Figure 3.2 (b)**).

Firstly, in the presence of ammonia, the silver ions (Ag⁺) are partially converted to silver diamine, Ag(NH₃)₂⁺. This introduces an additional reduction pathway to solid Ag formation, where H₂O₂, a primary radiolytic species, shifts from being exclusively an oxidizer for Ag to also reducing precursor Ag(NH₃)₂⁺ to form silver [75]. Secondly, NH₃ leads to the consumption of the oxidizing species OH[•] and O₂, leading to their diminished concentration [76]. The net effect is a significantly enhanced rate of solid Ag deposit creation, through both an increase in the reduction to Ag and a decrease in oxidation of Ag. Ag(NH₃)₂⁺ also acts as an additional source of ammonia as each ion-complex releases two ammonia molecules into the film upon reduction (**Figure 3.1**). Increasing ammonia concentration further amplifies these effects (**Figure 3.2 (c)**). In fact, at sufficiently high

ammonia concentrations, nearly all dissolved silver precursor is in $\text{Ag}(\text{NH}_3)_2^+$, enhancing the role of H_2O_2 as a reducer, and, as the oxidizing species are highly suppressed, the resulting higher net growth rates of Ag eventually come with a loss of resolution. Reaction-diffusion simulations were used to obtain detailed insights into the processes leading to variation of net reducing versus oxidating behavior as function of spatial location and time and thus identify the conditions in which high growth rate occurs without loss of deposit resolution.

During the NESA-FEBID process, sprayed non-volatile species concentrations will continuously increase, while volatile species concentrations reach a steady state (**Figure 3.1**). We consider two initial silver salt concentrations, 26.5 mM and 265 mM, which are the concentrations occurring at 1 s and 10 s, respectively, within a film of 50 μm radius and 1 μm thickness formed via introduction of a 250 μM AgNO_3 solution at a rate of 3 $\mu\text{L/hr}$. Initial free (not bound in silver diamine) dissolved ammonia concentrations in the film vary from ~ 100 μM up to 3 M, which corresponds to the steady-state concentration achieved assuming evaporation at the kinetic limit to vacuum from a film of 50 μm radius and 1 μm thickness formed via introduction of a 5% to 30% w/w ammonia concentration in water at a rate of 3 $\mu\text{L/hr}$ (typical experimental conditions). The initial concentration of silver ions and silver diamine ions is based on the total initial AgNO_3 concentration, the initial ammonia concentration, and the equilibrium condition, Equation (0.1).

1.9 Simulations

1.9.1 Reaction and Transport Model

A transient mass conservation and species transport model is used to simulate the dynamic interplay between chemical reactions and the diffusion of species within the system. The liquid film, depicted at the top of the diagram in **Figure 3.3** (a), is very thin owing to the nanoelectrospray delivery, such that the rate variations across it could be ignored for a quasi-1D axisymmetric treatment (**Figure 3.3** (b)).

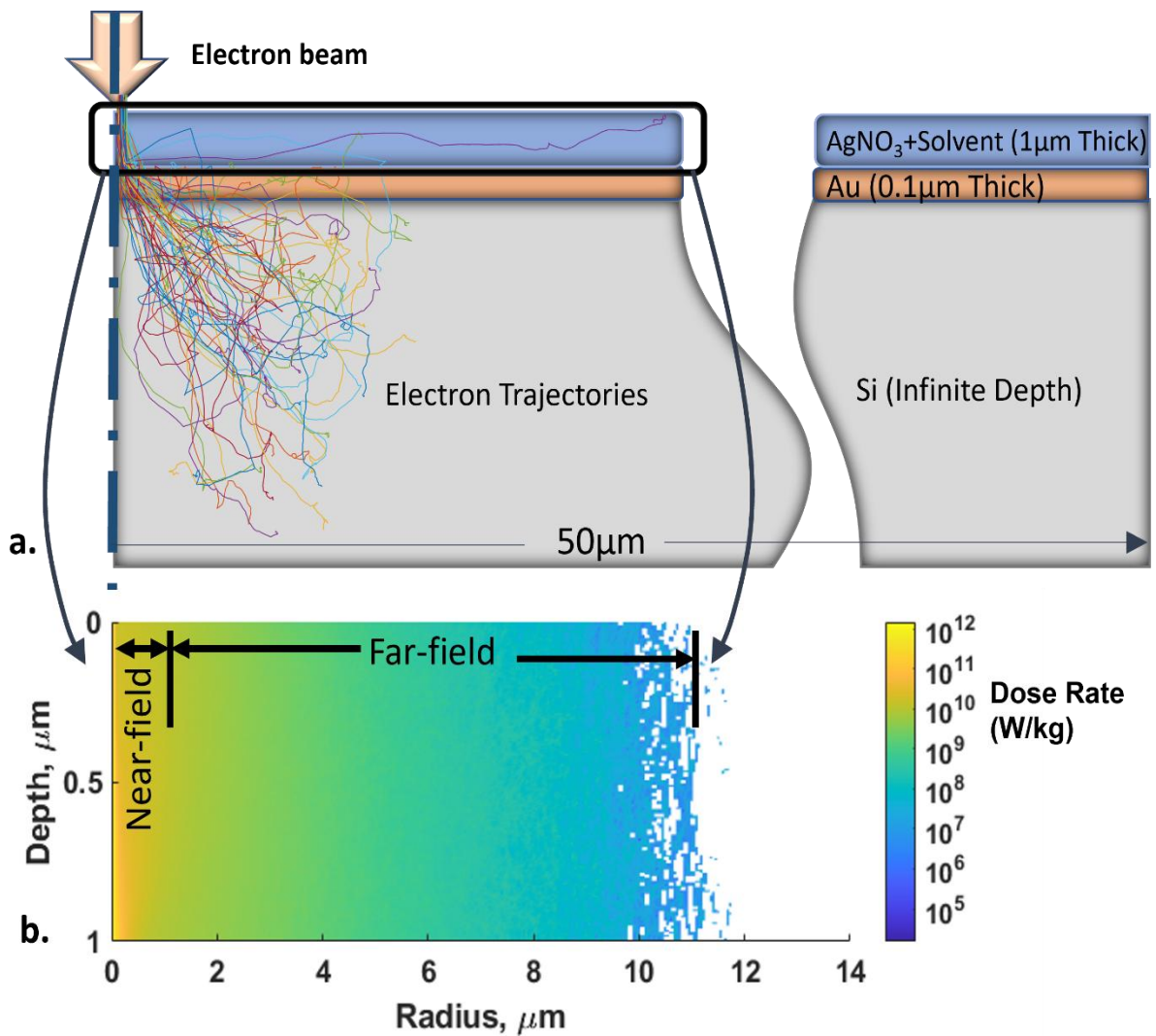


Figure 0.3 Monte-Carlo simulation is used to calculate the dose rate distribution due to a 30 kV, 3 nA electron beam irradiation. (a) The simulation domain - a 1 μm thick liquid film is overlaid on a 0.1 μm gold layer, which is placed on a thick (treated as semi-infinite) silicon substrate. (b) The axisymmetric dose rate distribution within the liquid film. The origin (0,0) is the point of electron beam irradiation, and the axis of symmetry is the vertical line passing through this point. Due to negligible axial variation in dose rate, the problem can be simplified to 1D axisymmetric.

Rather than introduce assumptions regarding the solid phase nucleation process, we use the Ag concentration as a proxy for nanostructure creation [36]. This allows us to treat solid metal reduction and oxidation as homogeneous processes with a correction factor accounting for heterogeneous (confined to the interface) nature of oxidation. Additionally, the effects of advection and electromigration are not considered, and Fickian diffusion is assumed. These assumptions have been shown to accurately capture the key processes and predict electron mediated metallic nanomaterial synthesis [36].

The variation of the concentration of species i , C_i , with time and radial position, t and r , respectively, is given by,

$$\frac{\partial C_i}{\partial t} = D_i \frac{1}{r} \frac{\partial}{\partial r} (r C_i) + S_i + R_i \quad (3.2)$$

D_i is the diffusion coefficient of species i , S_i is the net rate of production/consumption by homogeneous chemical reaction, and R_i is the net rate of production by radiolytic processes. The species production/destruction source terms are treated as the result of reactions (Appendix A), i.e.,

$$S_i = \sum_p k_p \prod_{j \in r_p} C_j^{s_j} - \sum_c k_c \prod_{m \in r_c} C_m^{s_m} \quad (3.3)$$

where, k_p and k_c and the rate constants for the chemical reactions producing species i , r_p , and consuming species i , r_c , respectively.

The exponents s_j and s_m represent the associated stoichiometric coefficients. The source term representing net creation or consumption by radiolysis, R_i , is given by $R_i = G_i \psi$ where the G-value, G_i , is solvent dependent and gives the moles of species i created per

unit energy of electron beam absorbed, and ψ is the local rate of energy deposition from e-beam irradiation, found using azimuthally and axially integrated values from Monte Carlo simulations implemented in CASINO, divided by thickness and circumference to obtain local average values for the 1-D simulations. The chemical reactions, the rate constants and G-values utilized are specified in Appendix A and Appendix B respectively.

The reaction source term, S_i , as given in Equation (3.3), is for homogenous reactions; however, the metallic silver produced by the NESA-FEBID process will eventually nucleate to form a nanostructure, a process that cannot be modeled explicitly in the 1-D formulations. In growing nanostructures, only the Ag present on the solid deposit surface remains exposed and susceptible for oxidation, via heterogeneous reactions. As a solid deposit increases in size its surface-to-volume ratio decreases, as does the proportion of Ag available for oxidation relative to the total amount of Ag locally present. To account for decreased availability of Ag for oxidation after nucleation, while maintaining the simplicity of a homogenous reaction model, we assume that the reaction rate of silver atoms on the surface of deposits follows the same rate expression as in the bulk, but only consider surface atoms as contributing to the concentration of Ag participating in the oxidation reaction. This approach is accomplished by modifying the form of the Ag oxidation expression with a dimensionless prefactor, f , that is a function of silver concentration: $f = \min(C^*/C_{Ag}, 1)$, where the value of the reference concentration C^* is based on the molar density of solid silver and the film thickness (1 μm), $C^* = 38.88 \text{ mol/m}^3$. Zero flux in far field and axial symmetry boundary conditions are used on the two domain boundaries.

We consider two initial silver salt concentrations, 26.5 mM and 265 mM, which are the concentrations occurring at 1 s and 10 s. The concentration was calculated as follows,

$$C_f = \frac{1}{V_f} \int_0^t Q_{es} C_{es} dt \quad (3.4)$$

where C_f is the concentration of $AgNO_3$ in the film, Q_{es} is the flow rate for electrospray, C_{es} is the concentration of $AgNO_3$ in electrosprayed solution and V_f is the volume of the film. For the case under consideration a 250 μM solution of $AgNO_3$ was electrosprayed at a flow rate of 3 $\mu L/hr$ to create a 50 μm radius and 1 μm height film. Using $t=1$ s as an upper limit for the integral, the concentration of $AgNO_3$ in the film is equal to 26.5 mM. For $t=10$ s, the concentration $C_f=265$ mM.

Due to the dynamic and non-linear nature of the process under vacuum conditions, it is very difficult to calculate the corresponding ammonia concentration in the film for a particular input nanoelectrosprayed ammonia concentration. A range of ammonia concentrations in the film was estimated using the kinetic limit to vacuum from a film of 50 μm radius and 1 μm thickness formed via the introduction of a 5% to 30% w/w ammonia concentration in water at a rate of 3 $\mu L/hr$ (typical experimental conditions).

$$\frac{dN_{evap}}{dt} = \alpha \frac{P_{vap}}{\sqrt{\pi MRT}} A_{surf} \quad (3.5)$$

$$\frac{dN_{es}}{dt} = Q_{es} C_{es} \quad (3.6)$$

$$\frac{dN_{H_2O}}{dt} = \frac{dN_{es,H_2O}}{dt} - \frac{dN_{evap,H_2O}}{dt} \quad (3.7)$$

$$\frac{dN_{NH_3}}{dt} = \frac{dN_{es,NH_3}}{dt} - \frac{dN_{evap,NH_3}}{dt} \quad (3.8)$$

The upper and lower limits of the ammonia concentrations in the film were estimated to lie between 0.1 M and 3 M.

The model was implemented in COMSOL Multiphysics software.

1.9.2 Electrochemical Lensing: Insights from Simulations

Electrochemical lensing is the phenomenon in which the transport and reaction interaction result in preferential growth in the near-field while minimizing nanostructure deposition in the far-field, a phenomenon which can be exploited to achieve high resolution deposits as shown schematically in **Figure 3.4** (a) (middle panel).

To demonstrate the effect of ammonia content on deposition, we perform simulations at multiple ammonia concentrations. The key result of simulations is the concentration of Ag, which serves as a proxy for silver nanostructure growth. **Figure 3.4** (b) and **3.4** (c) show the resulting Ag concentrations for various NH_3 initial concentrations after a 1 s exposure of the film to a 30 kV electron beam.

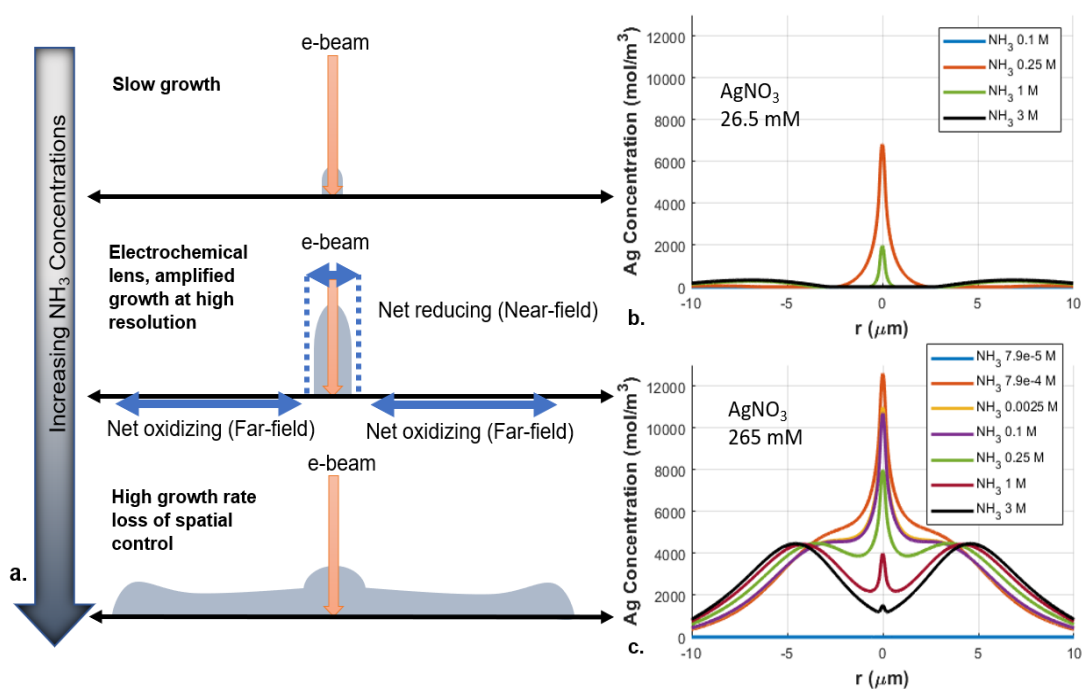


Figure 0.4 (a) Nanostructure deposition in water-ammonia solvents. In pure water or low ammonia, minimal nanostructure formation occurs due to oxidizing conditions. Optimal ammonia concentrations for electrochemical lensing result in focused and rapid nanostructure growth with high resolution, as reducing conditions prevail in the near-field and oxidizing conditions prevent nanostructure formation in the far-field. High ammonia concentrations lead to rapid growth of solid phase throughout the domain with loss of resolution. Panel (b) shows the simulated axisymmetric (mirrored around y-axis) Ag concentration profiles, after 1 second electron beam irradiation across different NH_3 -water solution concentrations AgNO_3 concentration profile in a 26.5 mM AgNO_3 film, highlighting optimal NH_3 concentration for electrochemical lensing at 0.25 M NH_3 . Panel (c) illustrates the 265 mM AgNO_3 scenario, where increased precursor availability leads to substantial far-field deposition even at very small NH_3 concentrations in the film, resulting in

For the lower silver precursor concentration, 26.5 mM, electrochemical lensing is observed at an intermediate ammonia concentration (**Figure 3.4 (b)**). Negligible silver formation is observed after 1 second of beam exposure when the initial free NH_3 concentration is 0.1 M: for this precursor concentration and small initial concentration of free ammonia, the entire domain remains net oxidizing for silver. When the NH_3 concentration is increased to 0.25 M, the near-field environment becomes reducing, and Ag growth commences at the point of electron beam impingement, while the far-field continues to be oxidizing, thus, preventing Ag production away from the e-beam irradiation. This distribution of Ag formation, resulting from creation of a reducing environment in the near-field only, is the hallmark feature of electrochemical lensing. As the NH_3 concentration is further increased to 1 M, both the near-field and far-field environments become reducing, resulting in broadening of the area of net silver reduction. The strongly reducing environment not only leads to a higher rate of conversion of Ag^+ and $\text{Ag}(\text{NH}_3)_2^+$ precursor ions into Ag in the far-field, but also, in turn, decreases the availability of these precursor ions for diffusion towards the near-field. Consequently, the central Ag pillar experiences a precursor shortage, slowing its growth as compared to the rate observed at 0.25 M NH_3 . This effect is even more pronounced for higher concentrations of ammonia: for initial NH_3 of 3 M, significant far-field Ag formation occurs while central deposit formation is very limited.

Electrochemical lensing is not observed for all precursor silver salt concentrations. When initial AgNO_3 is 265 mM, even very small initial concentrations of free ammonia correspond to rapid and widespread Ag formation (**Figure 3.4 (c)**). In part this is due to the presence of significant “bound” ammonia locked in the $\text{Ag}(\text{NH}_3)_2^+$ complex. When silver diamine is reduced, NH_3 enters solution, resulting in an increase of ammonia

concentrations (**Figure 3.1**). Thus, while at extremely low initial free ammonia levels (79 μM), silver growth is negligible, high rates of near-field deposition are achieved even with only 0.79 mM of initial free ammonia. However, the lensing effect that occurs at the lower salt concentration is diminished, with significant net reduction occurring outside the near-field region, as NH_3 released during $\text{Ag}(\text{NH}_3)_2^+$ reduction, diffuses to the far-field. At higher ammonia concentrations (2.5 mM to 3 M), silver growth is even more pronounced in the far-field, leading to formation of volcano-like structures (**Figure 3.4 (c)**).

Simulations reveal the fundamental principles for the observed deposition behavior as a function of ammonia and silver salt concentration. **Figure 3.5** depicts key reaction rates and concentrations in the near-field (center) 1 sec after electron beam irradiation of a 26.5 mM silver nitrate film for four representative initial ammonia concentrations. In addition to the instantaneous rate of silver creation (**Figure 3.5 (a)**), which mirrors the results showing net silver produced in the near-field from **Figure 3.5 (b)**, **Figure 3.5 (b)** depicts the dominant reduction and oxidation reaction rates. Even at the lowest ammonia concentration, 0.1 M, solvated electron reduction of Ag^+ has been supplanted as the dominant Ag production route by H_2O_2 reduction of $\text{Ag}(\text{NH}_3)_2^+$. The higher rate of silver production at 0.25 NH_3 ammonia is not due to higher rates of reduction but a more significant decrease in the rate of oxidation than in the rate of reduction. In particular, the consumption of oxidizing species OH^\bullet and O_2 by NH_3 and radiolytically produced NH_2^\bullet , as evident in **Figure 3.5 (c)**, is responsible for the higher net silver production rate. The diminished Ag production with further increases of NH_3 concentrations to 1 M and 3 M corresponds with a decrease in the concentration of $\text{Ag}(\text{NH}_3)_2^+$ in the near-field, **Figure**

3.5 (d), which is due to consumption of the precursor during far-field silver production which prevents it from being available to diffuse to the center.

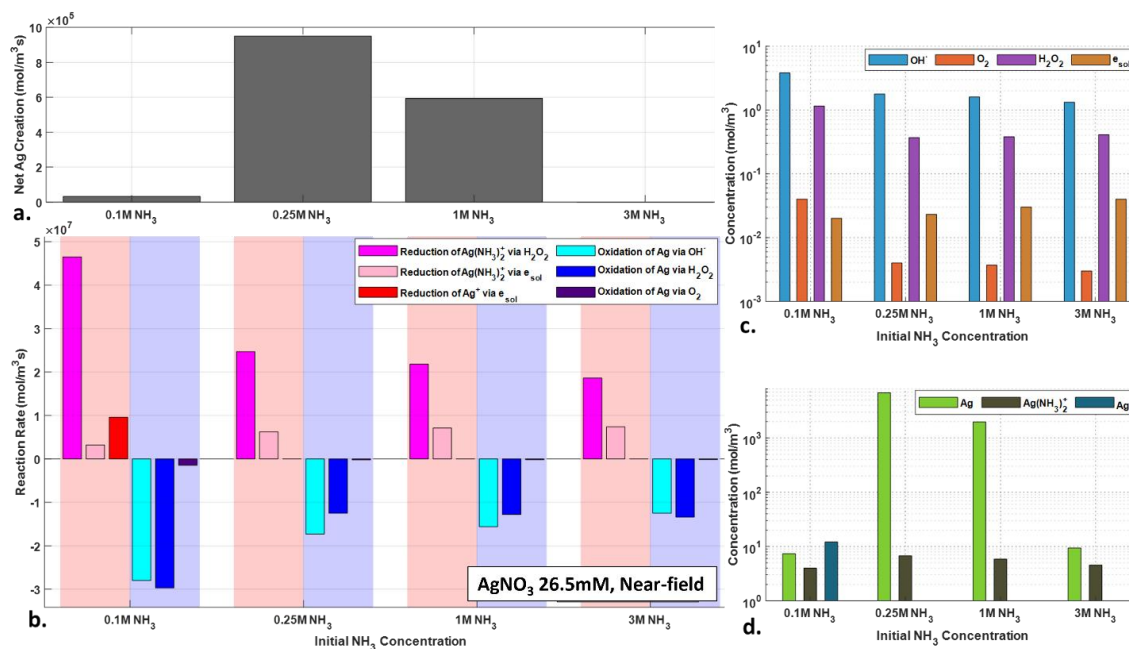


Figure 0.5 Key reaction rates and concentrations in the near-field (center) for a 26.5 mM AgNO₃ solution at NH₃ concentrations of 0.1, 0.25, 1, and 3 M post 1 sec electron beam irradiation. Panel (a) illustrates the net instantaneous rate of silver deposition showing peak Ag creation in the near-field at 0.25 M NH₃. The net Ag silver deposition is the sum of all the reduction and oxidation pathways for precursors and Ag, respectively (b). Concentrations of key oxidizing and reducing species are shown in (c). Concentrations of Ag and the precursor ions are shown in (d), which indicates a partial conversion of Ag⁺ to Ag(NH₃)₂⁺ contributing to a negligible Ag creation at 0.1 M NH₃ (a). Additionally, decreasing precursor concentrations from 0.25 M to 3 M NH₃ in (d) is responsible for the drop in Ag creation.

Figure 3.6 depicts reaction rates and concentrations of key redox-mediating species in the far-field (4.5 μm from the center) for four representative initial ammonia concentrations 1 s after electron beam irradiation of a 26.5mM silver nitrate film. As was seen for moderate ammonia concentrations in the near-field, increasing rates of silver production in the far-field at higher ammonia concentrations (**Figure 3.6 (a)**) are due primarily not to the increased rates of reduction, but as a result of even greater decrease in the rates of oxidation (**Figure 3.6 (b)**). The oxidizing species OH^\bullet and O_2 are formed by radiolytic processes in the near-field and must diffuse to the far-field. As NH_3 concentration is raised, more OH^\bullet and O_2 are scavenged prior to reaching the far-field, **Figure 3.6 (c)**.

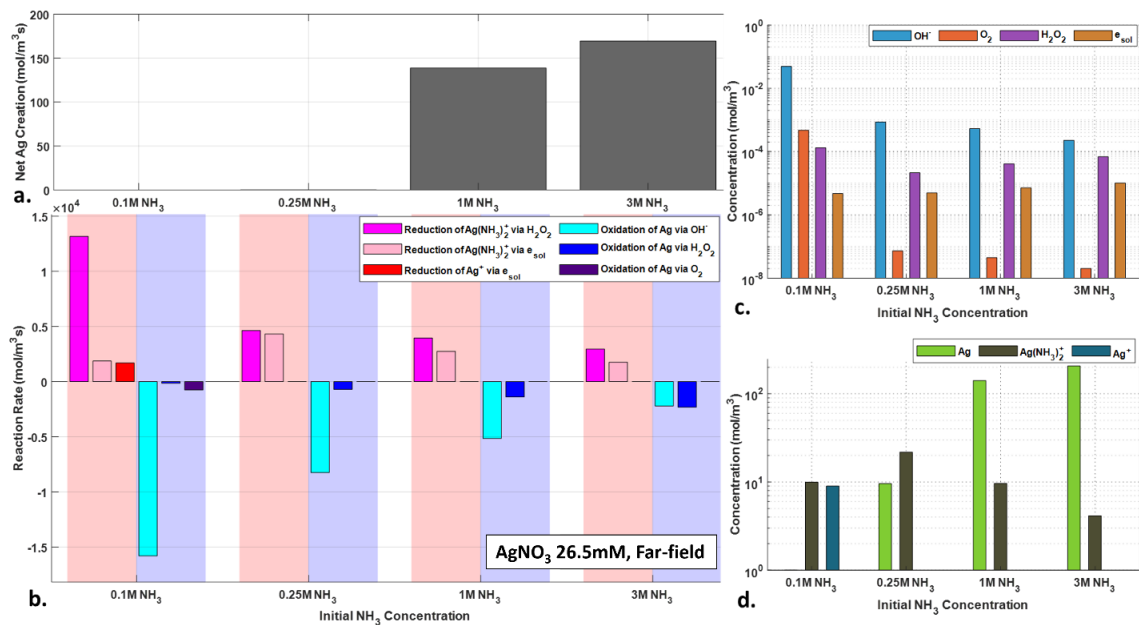


Figure 0.6 Key reaction rates and concentrations for far-field (4.5 μm from the center) silver deposition dynamics under varying NH_3 concentrations in a 26.5 mM AgNO_3 solution following electron beam exposure of 1 sec are shown. The net rate of Ag deposition (a) shows the increase in the rate of Ag creation in the far-field with higher NH_3 concentrations - this rate is the sum of all the reduction and oxidation reaction rates shown in (b). Concentrations of reducing and oxidizing species participating in creation or consumption of Ag is showing in (c). The Ag and precursor ions concentrations (d) show an increase in far-field Ag creation with increased NH_3 , as well as a corresponding drop in the precursor ion concentrations.

This leads to a faster drop in the rates of oxidation with increasing ammonia concentration than in the rates of reduction. As a result, net Ag creation occurs in the far-field for these NH_3 concentrations. The reducing environment in the far-field also leads to a drop in concentration of the precursor $\text{Ag}(\text{NH}_3)_2^+$ as it is consumed in the H_2O_2 mediated reduction reaction, **Figure 3.6** (d). This leads to a decrease in the rate of $\text{Ag}(\text{NH}_3)_2^+$ diffusion into the near-field and a slower growth of Ag in the near-field.

Figure 3.7 depicts in greater detail the role of transport on silver deposition rates at different locations. A film consisting of extremely low (or none) NH_3 , **Figure 3.7** (a), will lead to an overall oxidizing environment. This yields very little or no creation of Ag anywhere. Additionally, very little conversion of Ag^+ and $\text{Ag}(\text{NH}_3)_2^+$ to Ag causes a very small concentration gradient of Ag^+ and $\text{Ag}(\text{NH}_3)_2^+$ and consequently a very small diffusion flux. At optimum NH_3 concentration, **Figure 3.4** (b), reducing conditions are established at the near-field, while conditions at the far-field remain oxidizing. This leads to conversion of precursor, primarily $\text{Ag}(\text{NH}_3)_2^+$, to Ag in the near-field, with precursor supplied to the near-field by diffusion from the far-field. At higher NH_3 concentrations, **Figure 3.7** (c and d), precursor is reduced to Ag both in the near-field and far-field. This leads to growth of Ag in the far-field, as well as slowing down of growth of Ag in near-field by decreasing the diffusion of precursor towards the near-field. The ammonia concentration (0.25 M) associated with the highest magnitude diffusion flux is the one at which electrochemical lensing effect occurs. **Figure 3.7** (e) shows the simulated diffusive flux profiles of $\text{Ag}^+/\text{Ag}(\text{NH}_3)_2^+$ precursor in the domain at 1 s. The highest diffusive flux towards the nearfield is observed at 0.25 M NH_3 . Increasing ammonia to 1 M decreases the precursor flux towards the center resulting in slower central pillar growth. Further increase

to 3 M of NH_3 amplifies this effect. **Figure 3.7 (f)** shows the total amount of the precursor delivered towards the center over 1 s from distance of $0.2 \mu\text{m}$ (a proxy for the deposit size). The greatest precursor diffusion occurs at 0.25 M ammonia concentration, resulting in electrochemical lensing with amplified Ag deposition in the nearfield.

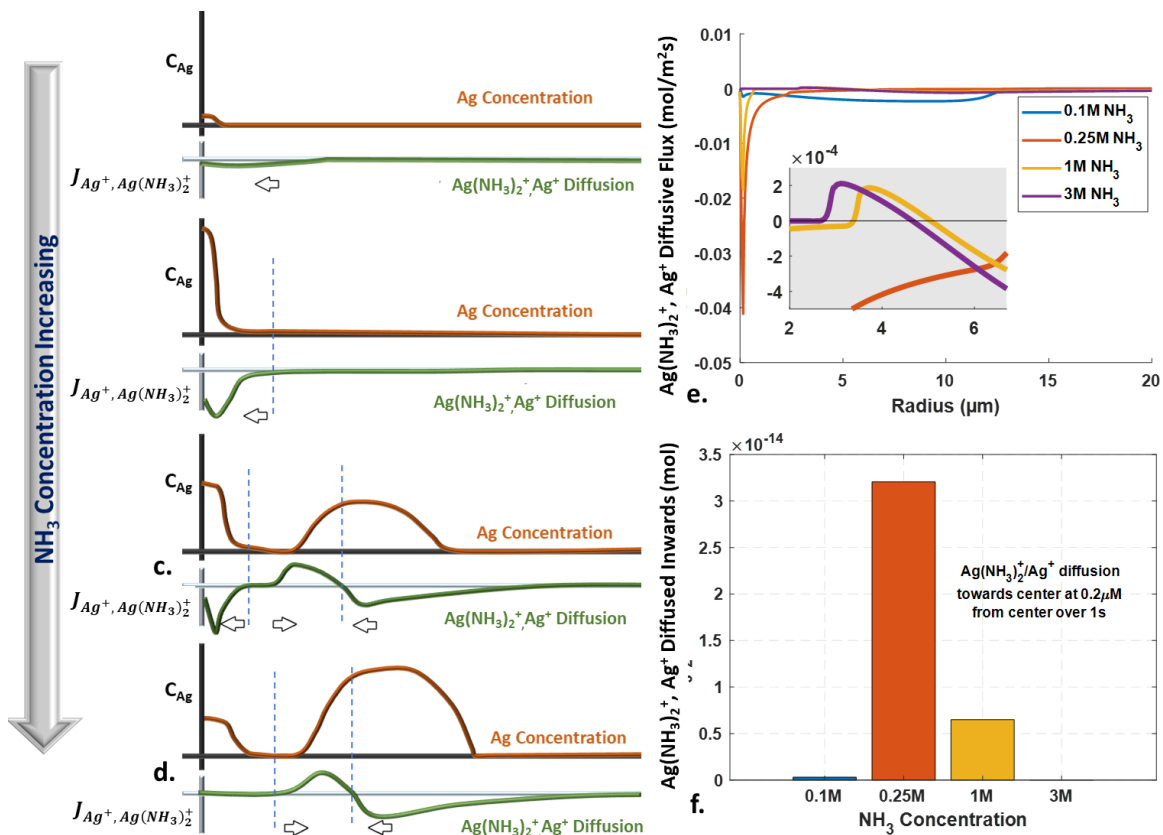


Figure 0.7 Impact of NH_3 concentration on $\text{Ag}^+/\text{Ag}(\text{NH}_3)_2^+$ precursor diffusion and Ag creation. (a-d) schematically illustrate the effect of increasing ammonia concentrations on diffusion of precursor in the domain and resulting Ag creation. In low NH_3 or pure aqueous conditions (a), oxidizing conditions inhibit Ag formation, with minimal precursor diffusion. At optimal NH_3 concentration (b), a reducing environment in the near-field promotes precursor cations Ag^+ and $\text{Ag}(\text{NH}_3)_2^+$ conversion to Ag, while maintaining oxidizing conditions in the far-field, promoting precursor cation diffusion towards the near-field. Higher NH_3 concentrations (c-d) lead to Ag^+ and $\text{Ag}(\text{NH}_3)_2^+$ conversion in both the near-field and far-field, decreasing precursor cations available for diffusion towards near-field and slowing Ag growth. Panel (e) shows the simulated diffusive flux profiles for the precursor over the domain for various NH_3 concentrations

1.10 Experiments

1.10.1 Experimental Sample Preparation

HPLC grade deionized water (Sigma Aldrich) and an HPLC grade water-ammonia solution (Fisher) were used for all experiments. Silver nitrate salt (Sigma Aldrich) was dissolved in water and mixed with water-ammonia to achieve desired concentrations. A TA Hamilton 1750 TLL syringe was used to deliver the solution at 3 $\mu\text{L/hr}$ via a syringe pump. The solution nanoelectrospray was carried out using a fused silica capillary emitter (360 μm outer diameter, 100 μm inner diameter, pulled to a 3 ± 1 μm diameter tip using a Sutter P-2000 Laser-Based Micropipette Puller). The substrate was a 1 cm x 1 cm square Si wafer coupon with a 100 nm gold coating. The capillary to substrate distance is maintained at ~ 200 μm . The negative mode nanoelectrospray was initiated by electrically biasing the solution with -500 V at the metallic union using a SRS 5 kV power supply. Experiments were conducted using the FEI Quanta 200 SEM operated in high vacuum mode ($\sim 10^{-4}$ torr). To distinguish nanostructure deposits from salt precipitates, Nanometer Pattern Generation System (NPGS) exposed the film in a predefined pattern of four 1-second spots, facilitating the formation of discernible nanostructures. Post-deposition, the samples were immersed in water for 2 hours and subsequently dried.

1.10.2 Electrochemical Lensing - Corroborating Experiments

To corroborate our simulation results, we conducted a series of experiments using NESA-FEBID with a 250 μM AgNO_3 solution, under a 30 kV electron beam for 1 second. We explored the effects for varying NH_3 concentrations in the solvent. Attempts to form silver deposits using AgNO_3 dissolved in pure water (no ammonia) were not successful,

supporting the simulation predictions of suppression of Ag growth in a highly oxidizing environment. Line and square arrays of nanostructures (to ensure repeatability) deposited from initial 30%, 25% and 15% ammonia-water NESA-FEBID solutions (corresponding to 3, 1 and 0.25 M ammonia concentrations in the film) were analyzed via Atomic Force Microscopy (AFM). **Figures 3.8 (a) to 3.8 (i)** show both two- and three-dimensional images and the radial profiles of these nanostructures. Bruker Dimension Icon AFM was used for profiling the nanostructures. To compare the experimental results with the simulations, normalized pillar heights from the experiments, **Figure 3.8 (j)**, were

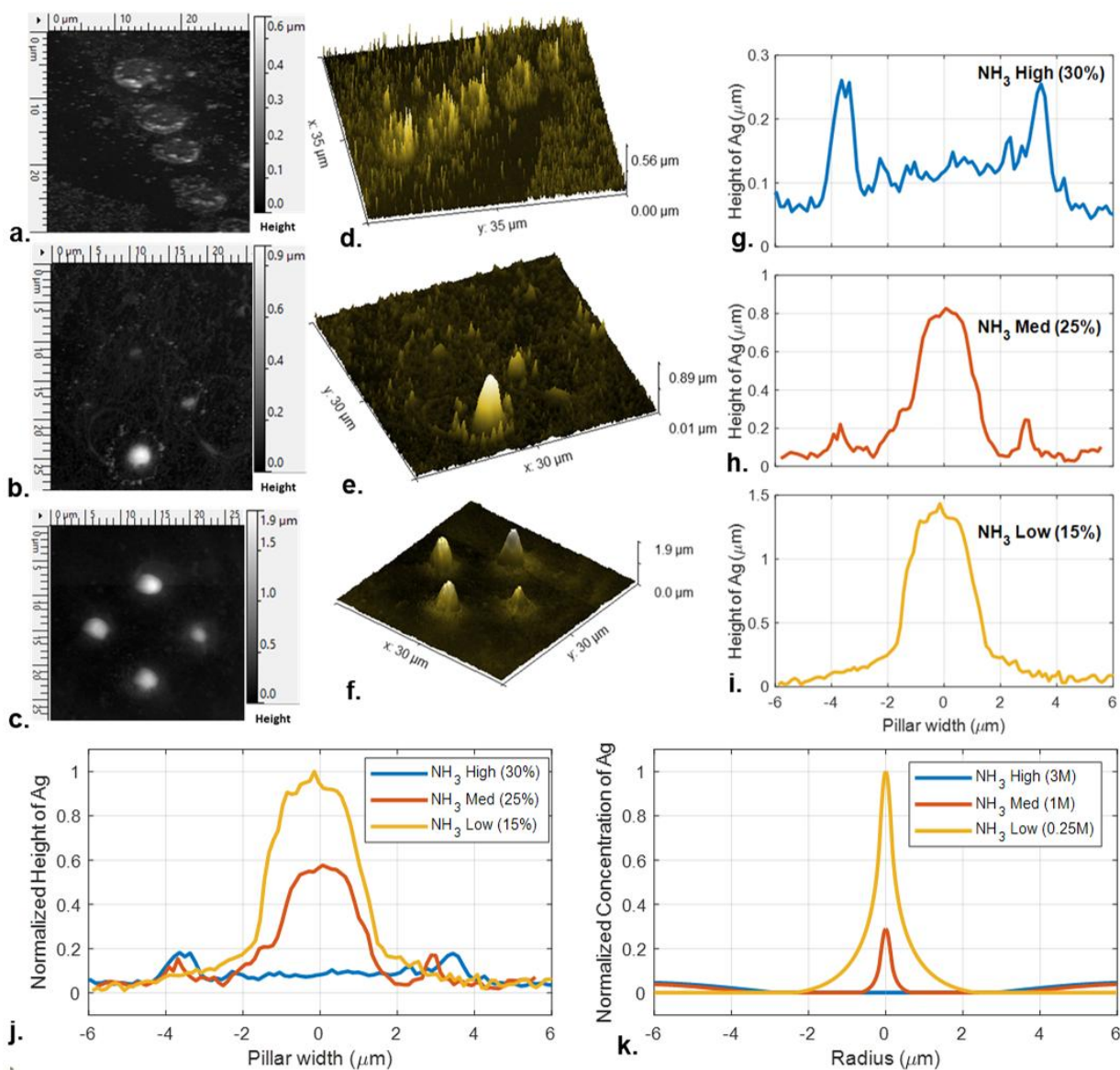


Figure 0.8 AFM images of nanostructures from NESA-FEBID using water-ammonia solutions with 250 μM AgNO_3 at 30%, 25%, and 15% NH_3 concentrations in top-view 2D (a-c) and 3D (d-f) radial profiles (g-i). Nanostructures are created with 1s 30 kV electron beam in 'spot' mode. Ag growth varies with NH_3 concentration, showing focused near-field growth at 15% NH_3 and increased far-field growth at 25% and 30% NH_3 . Normalized experimentally determined pillar profiles (j) are compared to simulated Ag concentration profiles at varying NH_3 levels (k), showing qualitative agreement and presence of an optimal NH_3 concentrations for focused near-field Ag growth, the signature of the electrochemical lensing.

compared to the normalized Ag concentration profiles obtained for different film NH₃ concentrations from the simulations, **Figure 3.8 (k)**.

Experimental silver creation follows the expected behavior with negligible silver growth in pure water, and a silver peak created in the near-field at 15% NH₃ NESA-FEBID solution with very little far-field growth. Increasing the concentration of NH₃ to 25% and 30% in the NESA-FEBID solution led to a higher Ag growth in the far-field and slower Ag growth in the near-field. This trend, predicted by simulations and confirmed by experiments, demonstrates the electrochemical lensing concept obtained when metal precursor cation is converted into its diamine complex enabling radiolytically produced H₂O₂ to act as a dual reducer and oxidizer. This leads to a high growth rate synthesis of high aspect ratio nanostructures in the near-field with corresponding increase in resolution.

1.11 Concluding Remarks

We present an approach to resolving the fundamental tradeoff between the growth rate and resolution in electron beam mediated direct-write nanofabrication through the technique of electrochemical lensing. When deposition processes are governed by systems with a linear behavior, the increase in concentration of a reactant, even locally at the desired deposition location, will result in a broader deposition region due to diffusion. Electrochemical lensing is accomplished via introduction of intentional non-linearity into the system. Metal nanostructure synthesis using FEBID from silver salt in a water-ammonia solution is a demonstration of electrochemical lensing, in which the strong non-linearity of the system's response to changing ammonia concentration comes from the multiple roles played by ammonia in the system: (a) by binding silver cations into diamine silver complexes,

ammonia adds a new reduction pathway involving hydrogen peroxide and provides a mechanism for ammonia storage in the solution; and (b) by using both ammonia and its radiolytic decomposition product NH_2^\bullet to selectively scavenge oxidizing species. Generalization of the approach therefore requires seeking similarly complementary nonlinearities for exploitation either through use of a solvent for forming multiple forms of a cation whose reduction leads to solid formation and/or encoding the redox switchable behavior to one or more transient intermediary species that facilitates the synthesis reaction. Electrochemical lensing as a conceptual model for synthesis improvement could play a significant role in a wide variety of nanomanufacturing applications, offering a scalable, precise, and efficient pathway for the creation of nanostructures with greater control of shape and resolution.

In summary, the electrochemical lensing strategy demonstrates that tuning solvent chemistry, through varying the ammonia concentration, and exploiting the species transport-reaction interaction, we can guide electron-beam-induced growth to achieve superior resolution. In Chapter 4, we extend this redox control framework to 3D copper surface patterning, where no external precursor is used. Specifically, electron beam induced oxidation of the copper surface generates copper ions and ion-complexes that can serve as precursors for deposition. By carefully modulating ammonia levels, we show that the ammonia-mediated FEBIP can enable a dual-mode process, integrating deposition and etching in one framework.

E-BEAM-GUIDED REDOX-CONTROLLED ETCHING AND DEPOSITION

1.12 Introduction

The ammonia-based liquid phase FEBIP approach has thus far been demonstrated with externally supplied metal salt precursors for additive nanofabrication. In this chapter, we show how a metal (copper) surface offers a platform where the substrate itself supplies the necessary copper ions through oxidation. In this system, the electro spray is directly performed on a copper surface, and the copper ions and ion-complexes released by the oxidation of the surface act as precursors for subsequent electron beam driven deposition. By adjusting the ammonia concentration and exploiting the balance between radiolytic oxidizing and reducing reaction rates and locations, we demonstrate that the electron beam can alternate between etching and deposition. This dual-mode capability enables the formation of unique peak-in-valley nanostructures and highlights the versatility of ammonia-mediated processing for direct-write nanofabrication.

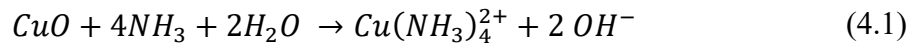
Our previous work revealed that ammonia concentration in aqueous precursors governs redox balance during electron beam processing. At high ammonia concentrations, longer life-times of solvated electrons [50], rapid formation of metal-ammine complexes, and scavenging of radiolytic oxidizers (e.g., OH^\bullet , H_2O_2) establish a reducing environment. [36, 46] Conversely, low ammonia concentrations lead to an oxidizing environment due to abundant radiolytic oxidizers.

Building on these insights, using the interplay between oxidizing and reducing species, we report a technique to spatially control etching or deposition on a metal surface. On exposure to ammonia, metal-amine complex positive ions are released into a solution by heterogeneous oxidation of metal and metal oxide without an electron beam. This combined with the ammonia-driven suppression of radiolytic oxidizing species such as OH^\bullet and H_2O_2 creates a net reducing environment leading to the guided (direct-write) deposition of metal onto the surface after exposure to a focused electron beam. On the other hand, a lower ammonia concentration yields less heterogeneous oxidation of metal and surface metal oxide via metal-amine complexation, as well as less suppression and higher concentration of radiolytic oxidizing species from the e-beam exposure. In turn, this leads to guided (direct-write) etching via oxidation of metal surface upon irradiation by a focused electron beam. With longer e-beam exposures, this e-beam induced oxidation accumulates and leads to a local increase in the concentration of metal and metal amine cations, causing redeposition of metal onto the etched surface, creating peak-in-valley nanostructures.

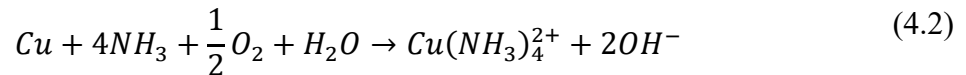
The interplay between competitive generation of reducing vs oxidizing radiolytic species, ammonia solvent-mediated redox balance, and precursor ion transport dynamics is systematically explored through simulations and experiments. This paper is organized as

follows. First, we detail the experimental setup for liquid-phase e-beam processing. Next, we detail the chemical pathways underpinning metal oxidation, metal ion reduction and redeposition, highlighting the critical role of ammonia concentration as the mediator of the dominant reaction pathway. A reaction-transport model is then developed to quantify the spatiotemporal evolution of chemical species, including the proxy representation for relevant reactions. Finally, results from the experiments are discussed through the lens of modeling enabled fundamental insight to establish generalized principles for achieving etching and/or deposition of metal nanostructures via e-beam guided synthesis.

To achieve a stable liquid precursor film in the vacuum environment, we employ a nanoelectrospray-assisted solution delivery system. This system generates an ultra-thin film of a water-ammonia solution on a copper substrate. A thin oxide layer naturally exists on the copper surface due to environmental exposure. This oxide layer reacts with ammonia to produce solvable copper-amine ion complexes, as described by the following reaction [77],

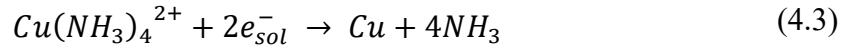


Additionally, the water-ammonia solution contains dissolved oxygen. In the presence of oxygen copper reacts with water-ammonia to form a copper-amine ion complex.^[39]

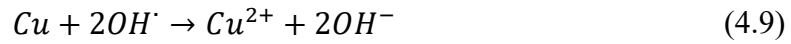
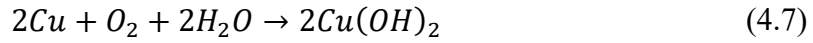


In the second step, the liquid film is exposed to a focused electron beam. The electrons undergo elastic and inelastic collisions with the atoms and molecules of the solution,

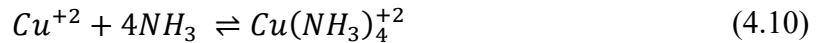
initiating radiolysis. This leads to generation of radiolytic species, including solvated electrons (e^-_{sol}) and OH^\bullet , H_2O_2 , O_2 , H^+ , OH^- , and NH_2^\bullet [36, 72, 73]. For the process in consideration, the radiolytic species can be classified as reducing or oxidizing as per their ability to either reduce copper ions/ion-complexes or oxidize copper. Solvated electrons are reducing due to their ability to carry out the following reactions:



Species such as H_2O_2 and OH^\bullet are oxidizing copper to produce its cationic form.



The cuprous and cupric ions released into the solution rapidly equilibrate with ammonia in the solution forming copper-amine ion complexes. The resulting most dominant ion-complex in the solution is the tetraamine copper, formed via following reaction [78].



The rate of reduction is directly proportional to the product of the concentration of precursor cations (copper ion and ion-complexes). At higher ammonia concentrations, **Figure 4.1** (left), a greater amount of copper is converted into copper-amine ion complexes, Equations (4.1) and (4.2). Additionally, a high concentration of ammonia create conditions for suppression of radiolytic oxidizing species, and a relative increase in the concentration of radiolytic reducing species. This leads to a net reduction of copper ions/ion-complexes, leading to deposition of copper.

The rate of oxidation on the other hand is directly proportional to the concentration of the radiolytic oxidizing species. In case of lower ammonia concentration, the relative concentration

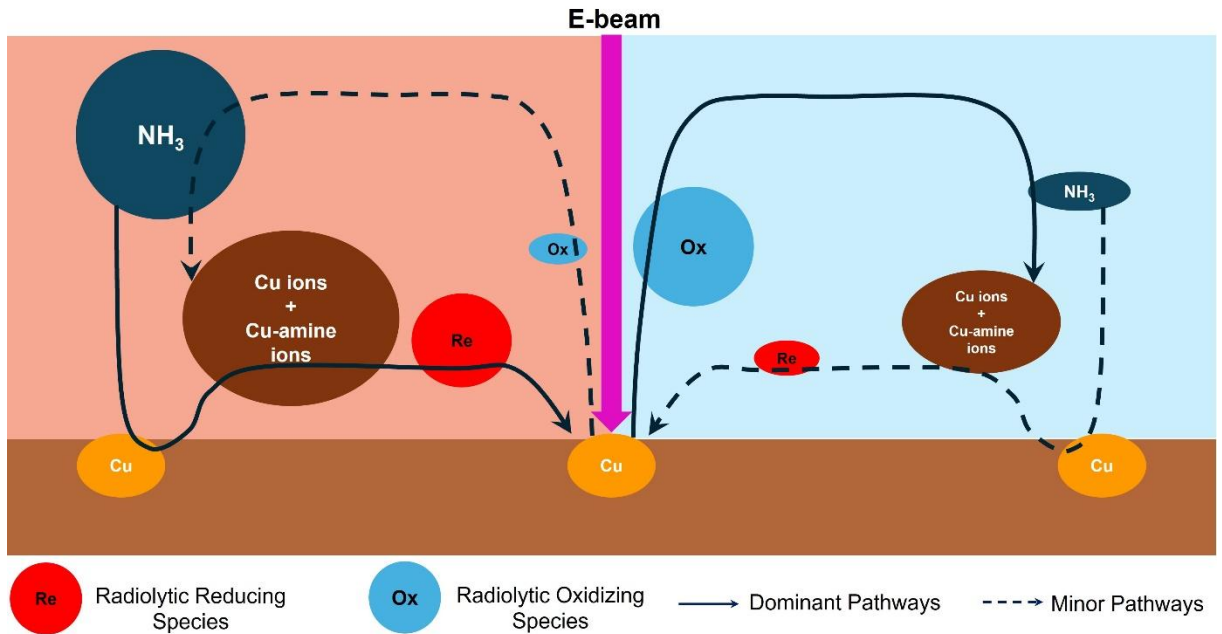


Figure 0.1 Chemical-kinetic pathways illustrating how varying the ammonia concentration affects copper etching or deposition. The relative sizes of each species “balloons” (e.g., ammonia, copper ions/ion-complexes, oxidizing species, reducing species) in the schematic reflect their approximate concentrations. At high ammonia concentration (left), copper-amine complexation is more pronounced and radiolytic reducing species outcompete radiolytic oxidizers, driving copper redeposition. At low ammonia concentration right, less copper-amine complexes form while the radiolytic oxidizing species predominate, leading to net copper etching.

of radiolytic oxidizing species is higher than the radiolytic reducing species, **Figure 4.1** (right). Furthermore, due to a lower concentration of ammonia, the equilibrium conversion to copper-amine ion complexes, Equation (4.1) and (4.2), is suppressed. Upon the electron beam irradiation, the conditions are created for faster rate of copper oxidation in comparison to the reduction of copper ions/ion-complexes, leading to etching of the surface.

1.13 Theoretical Analysis

1.13.1 Simulating Redox Dynamics

To describe the ammonia-mediated spatiotemporal behavior of radiolytic redox species, we have employed transient mass conservation and chemical species transport model. As the liquid film is ultra-thin and e-beam is much smaller in diameter than the film extent, a 1-D axisymmetric model has been used. Diffusion is Fickian and the effects of electromigration and advection have been ignored. No heterogeneous reaction or nucleation of deposits is considered. These simplifications have shown to accurately predict the focused electron beam mediated radiolytic species generation and transport within a liquid film [38]. Whether the process leads to deposition or etching is determined by the dominance of the respective reaction pathways as described in the previous section.

The temporal and spatial variation of chemical species C_i is governed by Equation (4.11).

$$\frac{\partial C_i}{\partial t} = D_i \frac{1}{r} \frac{\partial}{\partial r} (r C_i) + S_i + R_i \quad (4.11)$$

Here, D_i is the diffusion coefficient of species i , S_i represents the net rate of production or consumption of i due to homogeneous chemical reactions and the radiolytic source term is given by R_i . Here, G_i is the solvent-dependent G -value, which quantifies the moles of species i produced per unit energy absorbed from the electron beam. Local 1-D axisymmetric averages of dose rate are calculated by azimuthally and axially integrating the dose rates obtained from Monte Carlo simulations performed in CASINO, divided by circumference and thickness. Description of extraction of dose rate from CASINO results is given in section 2.3.1.

The rate constants are given in Appendix A. The diffusivities are given in Appendix C while the G -values for focused electron beam driven water-ammonia radiolysis are given in Appendix B. Axial symmetry and zero flux (far field) boundary conditions are specified at the two domain boundaries.

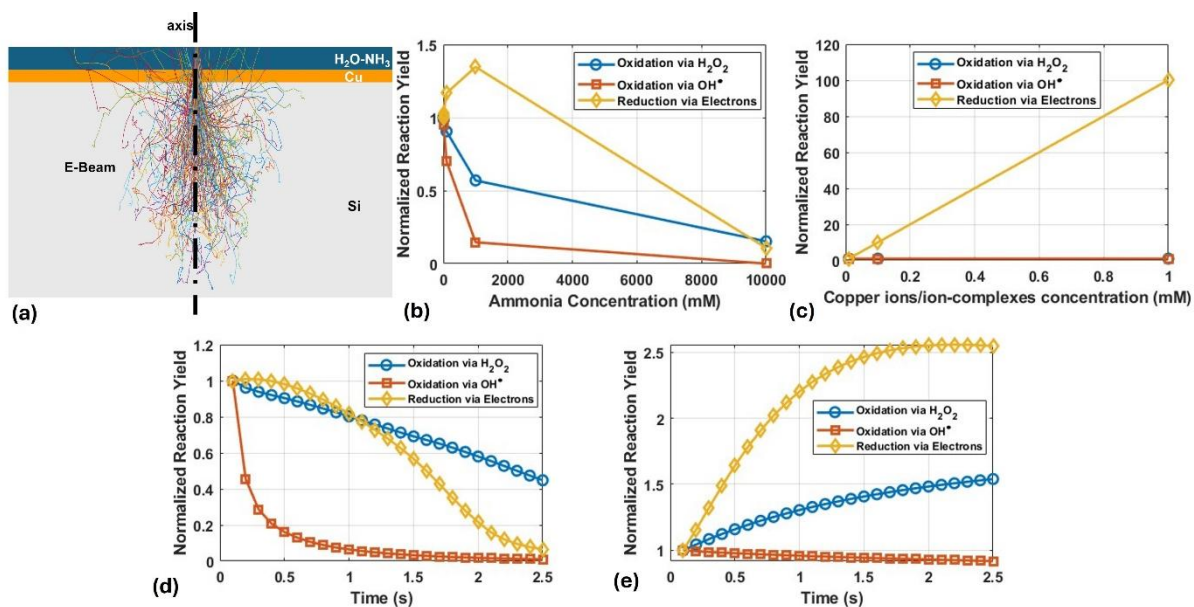


Figure 0.2 Simulations reveal the competition between reduction (deposition) and oxidation (etching) pathways under varying conditions. (a) Monte Carlo simulations are performed to calculate the dose rate for a 20 kV electron beam. A 1 μm water-ammonia film is analyzed atop a 200 nm copper layer, on a thick silicon substrate (treated as semi-infinite). (b) Effect of ammonia concentration at the beam center (2.5 s exposure, 0.1 mM initial deposition precursor copper ion/ion-complexes). Fractional reaction yields for oxidation (proportional to H₂O₂ and OH* concentrations) and reduction (proportional to the product of precursor cations and solvated electrons concentration) are normalized to the 0.1 mM ammonia case. Increasing ammonia lowers radiolytic production of oxidizing species (reducing the rate of etching). There is a spike in reduction rates due to higher precursor availability at lower ammonia concentration. However, with an increase in ammonia concentration >1000 mM, rapid precursor cation depletion, caused by accelerated initial consumption from high reduction rates, ultimately inhibits reduction and deposition. (c) Reaction yields normalized to 0.01 mM precursor concentration (1000 mM

ammonia, 2.5 s exposure). Higher precursor availability increases reduction yields, while oxidation remains unaffected. (d) High ammonia concentration (10,000 mM NH₃, 1 mM initial concentration of precursor cations). High ammonia creates a strongly reducing environment, driving rapid copper deposition initially. However, prolonged electron beam exposure depletes precursor cations through reduction reactions, weakening the reducing effect over time and slowing down deposit growth. (e) Low ammonia concentration (100 mM NH₃, 0.01 mM initial concentration of precursor cations). Low ammonia fosters an oxidizing regime, etching copper initially. With extended exposure, reduction yield rises faster than oxidation yield, slowing etching for longer e-beam exposures.

The water-ammonia solution forms an ultra-thin ($<1 \mu\text{m}$) liquid film on the copper surface (200 nm Cu e-beam evaporated on a Si substrate), as illustrated in **Figure 4.2** (a). This film is irradiated with a 20 kV electron beam, initiating radiolysis. Due to the higher volatility of ammonia compared to water, the ammonia concentration in the film decreases over time. The presence of ammonia in the liquid film interacts with the copper/copper oxide interface and releases copper ions/ion-complexes (Equations 4.1 and 4.2) into a solution, which act as deposition precursors. Because ammonia evaporates more rapidly than water in high-vacuum NESA, the in-film concentration of ammonia is lower than the electrospray stock concentration. Accordingly, hereafter we use “wt %” specifically for the stock solution and “M” specifically for the estimated in-film concentration.

Because water and ammonia evaporate at different rates under high vacuum and oxidation of copper generates copper-amine ion-complexes that consume free ammonia, a one-to-one conversion between electrospray stock concentration (wt %) and in-film molarity (M) is not possible quantitatively. Instead, we use the nominal wt % of ammonia in the electrosprayed solution, which is a measurable quantity that is precisely controlled in experiments, as a relative proxy: higher wt % values reliably correspond to higher in-film ammonia concentrations.

1.13.2 Ammonia Concentration Effects

To systematically probe ammonia’s role in modulating redox pathways, we simulate precursor cation (copper ions/ion-complexes) and radiolytic species dynamics across a broad range of ammonia concentrations (0.1 mM to 10,000 mM), as shown in **Figure 4.2** (b). Reduction reaction yields depend on the product of precursor cation and solvated

electron concentrations, which act as reducing species, while oxidation yields depend on oxidizing species such as H_2O_2 and OH^\bullet . Reaction yields are normalized to the 0.1 mM ammonia case at 2.5 s beam exposure, with an initial precursor cation concentration of 0.1 mM. Increasing ammonia concentration suppresses radiolytic oxidizing species, decreasing normalized oxidation yields. Conversely, normalized reduction yields rise with ammonia concentration due to prolonged solvated electron lifetimes. However, at further increase in the ammonia concentration, rapid precursor cation depletion from rapid early-stage reduction, shifts the regime from reaction-limited to transport-limited, lowering the normalized reduction yields. These trends demonstrate that low ammonia concentrations favor etching of copper (oxidation-dominant), while higher ammonia shifts the balance toward deposition of copper (reduction-dominant).

1.13.3 Release of Cations from Metal Substrate

The concentration of liberated cations (copper ions/ion-complexes) suitable for e-beam reduction and metal deposition is governed by two factors: (a) ammonia-driven dissolution of the copper/copper oxide layer, Equations (4.1) and (4.2), and (b) oxidation of the copper surface by radiolytic oxidizing species during electron beam irradiation, Equations (4.6) and (4.9). Higher ammonia concentrations accelerate precursor cation release via enhanced metal-ammine complexation. Additionally, localized oxidation of the copper surface during initial e-beam exposure releases copper ions into the solution, further increasing precursor cation concentrations. To isolate the influence of released cation concentration, simulations at 1000 mM ammonia and 2.5 s beam exposure were performed, **Figure 4.2** (c). Oxidation and reduction yields are normalized to the 0.01 mM precursor case. Increasing copper cation availability linearly enhances reduction yields, assuming the first

order reaction kinetics, as more cations participate in solvated electron-mediated reduction [Equations (4.3), (4.4) and (4.5)]. Conversely, oxidation yields remain unaffected by cation concentration, as oxidation reactions are exclusively heterogeneous.

1.13.4 Electron Beam Exposure Time Effects

The duration of electron beam exposure also determines the dynamic balance between reduction and oxidation pathways, with the redox environment evolving depending on ammonia and precursor concentrations. Figures 4.2 (d) and 4.2 (e) illustrate these temporal dynamics under high and low ammonia concentrations, respectively.

1.13.4.1 High Ammonia Conditions

For high ammonia concentrations (10,000 mM NH₃, releasing 1 mM precursor cations, **Figure 4.2** (d)), the environment is inherently reduction favorable. Initially, oxidizing species and oxidation rates decline rapidly, amplifying the reducing nature of the system and promotes metal deposition. At longer exposure times (>1 s), precursor depletion shifts the behavior to transport-limited, causing reduction rates to fall faster than oxidation rates. This reversal diminishes the reducing environment, slowing any growth of deposits.

1.13.4.2 Low Ammonia Conditions

For low ammonia concentrations (100 mM NH₃, releasing 0.01 mM precursor cations, **Figure 4.2** (e)), the system operates in an oxidation-dominant regime. Initially, abundant radiolytic oxidizers (OH[•], H₂O₂) will rapidly etch copper. However, as exposure time increases, the reduction rates will increase due to increasing concentrations of solvated

electrons and the net rate of oxidation will diminish with concomitant slow-down of material removal.

1.14 Experiments

1.14.1 Experimental Sample Preparation

HPLC-grade deionized water (Sigma Aldrich) and a water-ammonia solution (Fisher Scientific, 28–30% NH₃) were used as solvents. A 200 nm copper layer was e-beam evaporated on a silicon substrate. Nanoelectrospray-assisted solution delivery was achieved using a pulled fused silica capillary emitter (360 μm outer diameter, 100 μm inner diameter, tip diameter 4.5 ± 1 μm, made using Sutter P-2000 Laser-Based Micropipette Puller). A TA Hamilton 1750 TLL syringe delivered the water-ammonia solution at 15 μL/hr via a syringe pump. The substrate-to-nanoelectrospray capillary emitter distance was maintained at ~200 μm. A negative bias of -600 V (Stanford Research Systems PS325 high-voltage supply) initiated stable nanoelectrospray in high-vacuum mode ($\sim 10^{-4}$ Torr, FEI Quattro S SEM). Focused electron beam exposures (20 kV accelerating voltage, 2.5 nA) were performed using Nanometer Pattern Generation System (NPGS), with irradiation times ranging from 0.5–2.5 s. Substrates were rinsed with 1000 μL of 0.25% phosphoric acid (Sigma Aldrich) to dissolve residual salts, followed by air drying.

1.14.2 Redox-Mediated Etching and Deposition Interplay: Experimental Validation

The system's behavior under varying ammonia concentrations and electron beam exposure times has been evaluated experimentally to assess the fundamental insight from process modeling. Low and high ammonia conditions were represented by 5% and 25% ammonia

solutions, respectively. The substrate was silicon coated with a 200 nm thick layer of evaporatively deposited copper. Electron beam exposure times of 0.5, 1.5, and 2.5 s were used to probe the time-dependent effects. After irradiating the liquid film with the electron beam, the substrate is removed from the SEM and rinsed by dripping 1000 μL of 0.25% phosphoric acid to dissolve residual salt precipitates released from substrate exposure to ammonia.

A nanoelectrospray-formed liquid film is irradiated in spot mode with a 20 kV, 2.5 nA electron beam in a 2×2 pattern. After exposure, the nanoelectrospray emitter is repositioned to create a fresh film on a new substrate region, and the process is repeated, generating multiple 2×2 deposit/etch patterns. Nanostructures were imaged via SEM and EDS (FEI Quattro S). **Figure 4.3** (a) illustrates three examples of nanoelectrosprayed liquid films and their corresponding 2×2 patterned spot arrays produced after e-beam irradiation. To make the film boundaries and patterned regions immediately clear, we have overlaid white, dotted lines that trace the outer edge of the deposited film, and included high-contrast arrows that point directly to each spot pattern. The faint, vertical stripes running through the image are stitching artifacts from the Thermo Scientific MAPS software's tile-mosaic process; they result from merging multiple high-resolution tiles and do not reflect any beam-induced or material features. The spot arrays are placed close to the film edges to target regions with the least film thickness to minimize across the thickness variation of the solution composition and precursor concentration, which would contribute to variability of the process.

Figure 4.3 (b) shows a zoomed in view of a single spot in low-ammonia etch for 0.5 s.

Figure 4.3 (c-d) presents the EDS maps of copper (coating) and silicon (substrate) in the

corresponding region as proxies for material removal at the e-beam exposure site. The etched region is identified by diminished copper (green) signal in **Figure 4.3** (c) and elevated silicon (yellow) signal in **Figure 4.3** (d). The small surface imperfections surrounding the primary etch spot arise from non-electron-beam-mediated ammonia oxidation around pits and cracks of the copper coating and residual salt precipitates remaining after sample rinsing.

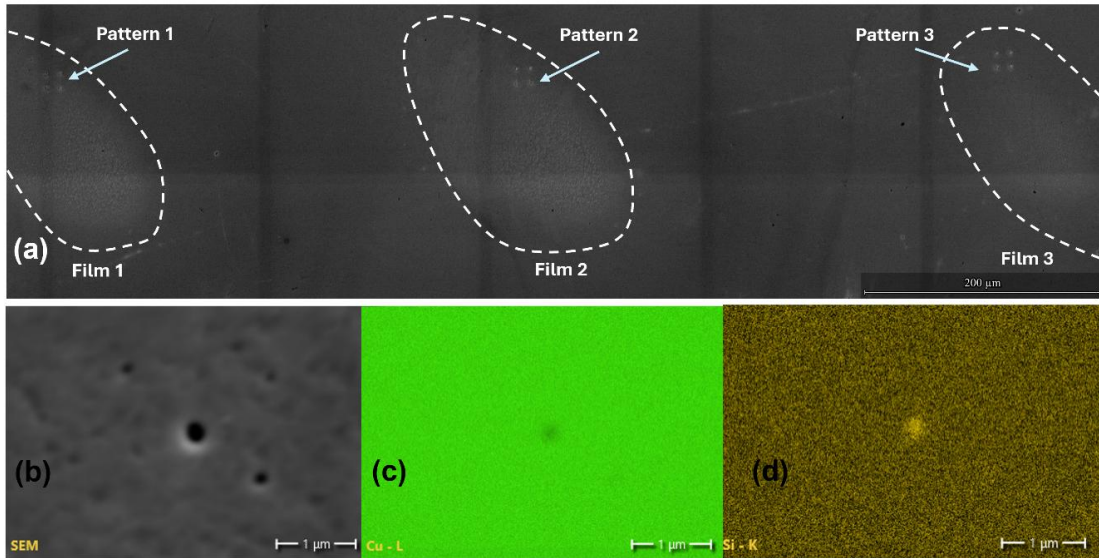


Figure 0.3 Visualization of electron-beam-mediated deposition/etching via SEM imaging and EDS analysis. (a) Zoomed-out SEM image of 2x2 ‘spot’ patterns formed by focused electron beam exposure (20 kV, 2.5 nA) of water-ammonia film. Locations of liquid films are seen as light gray shade domains. (b) Zoomed-in SEM image of a single etched ‘spot’ in 5% ammonia film and 0.5 s exposure time. (c-d) EDS elemental maps: (c) copper signal (green) decreases at etched site, (d) elevated silicon signal (yellow) from the substrate at etch site.

The SEM imaging provides limited insights to quantitative details of surface morphology, and atomic force microscopy (AFM) allows one to quantify etching depths, deposition heights, and lateral feature evolution. **Figure 4.4** presents 2D AFM (Bruker Icon, tapping mode) surface height maps and angularly averaged height profiles that capture the evolution of copper nanostructures under varying ammonia concentrations and irradiation times. At low ammonia (5%) and short exposure (0.5 s), the oxidizing environment etches the copper surface, removing a shallow pit, **Figure 4.4** (a,b). After a longer e-beam irradiation, a release and accumulation of deposition precursor cations into the film occurs via oxidation of the surface (Reactions 1 and 2), increasing the precursor local concentration. Extending irradiation to 1.5 s widens the etch zone via surface oxidation by the diffusing radiolysis species, while also initiating redeposition at the center from reduction of Cu/Cu-complex cation-rich environment, **Figure 4.4** (c,d). This is consistent with the simulation prediction that higher released cation concentration leads to locally reducing conditions, **Figure 4.2**(c). Further exposure (2.5 s) amplifies this effect, widening the etched “valley” and growing the central “peak”, **Figure 4.4** (e,f).

Conversely, high ammonia (25%) and short exposure (0.5 s) yield immediate copper deposition due to a large generation of cations in ammonia-rich environment, **Figure 4.4** (g,h). At 1.5 s, the central pillar grows and there is a creation of a ring-like structure **Figure 4.4** (i,j), attributable to radial diffusion of solvated electrons and precursor ions in opposite directions, a phenomenon explained in our previous work [37, 38]. Prolonged e-beam irradiation (2.5 s) plateaus pillar growth due to local precursor depletion by solvated electron reduction, **Figure 4.4** (k,l). This behavior matches the simulated decline in reduction yields at high ammonia concentration and extended times, **Figure 4.2** (d,e).

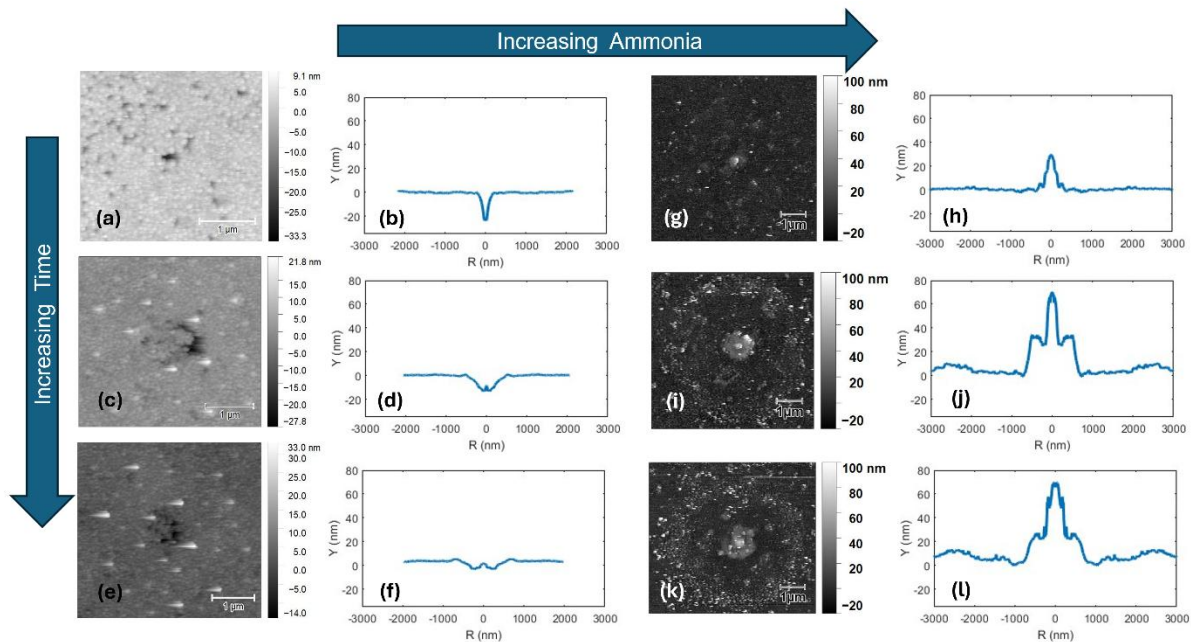


Figure 0.4 AFM images and their corresponding angularly averaged height profiles show the evolution of copper nanostructures under different ammonia concentrations and electron-beam irradiation times. (a,b) At low ammonia (5%) and short irradiation (0.5 s), a predominantly oxidizing environment leads to net copper etching. (c,d) Increasing the irradiation time to 1.5 s under the same low ammonia conditions causes widening of the etch via oxidation. The copper ions/ion-complexes formed due to prior oxidation diffuse towards and redeposit in the center at the e-beam impingement spot, forming the characteristic “peak-in-valley” structure. (e,f) A 2.5 s e-beam exposure at same (5%) ammonia concentration further widens the etched region and grows the redeposited peak. (g,h) At higher ammonia concentration (25%), copper is rapidly deposited even at short (0.5 s) irradiation time from the precursor cations released to the solution from the substrate on contact with ammonia, forming a nanopillar (i,j) At 1.5 s e-beam irradiation exposure, stronger reducing conditions and more copper-amine ion complexation drive rapid copper deposition at the center, but with an additional off-center ring formation. (j,k) Extending

the irradiation to 2.5 s under high ammonia results in a plateau of the deposit height due to local depletion of copper ions/ion-complexes, slowing further pillar growth.

The AFM profiles are in agreement with the simulation predictions, which capture the interplay between ammonia-mediated redox dynamics and time-dependent transition from kinetics to transport limited behavior as function of beam exposure duration. Remarkable is the predictive capability of the model that can be used for tailored design of peak-in-valley nanoarchitectures through solvent chemistry and temporal electron beam-exposure control.

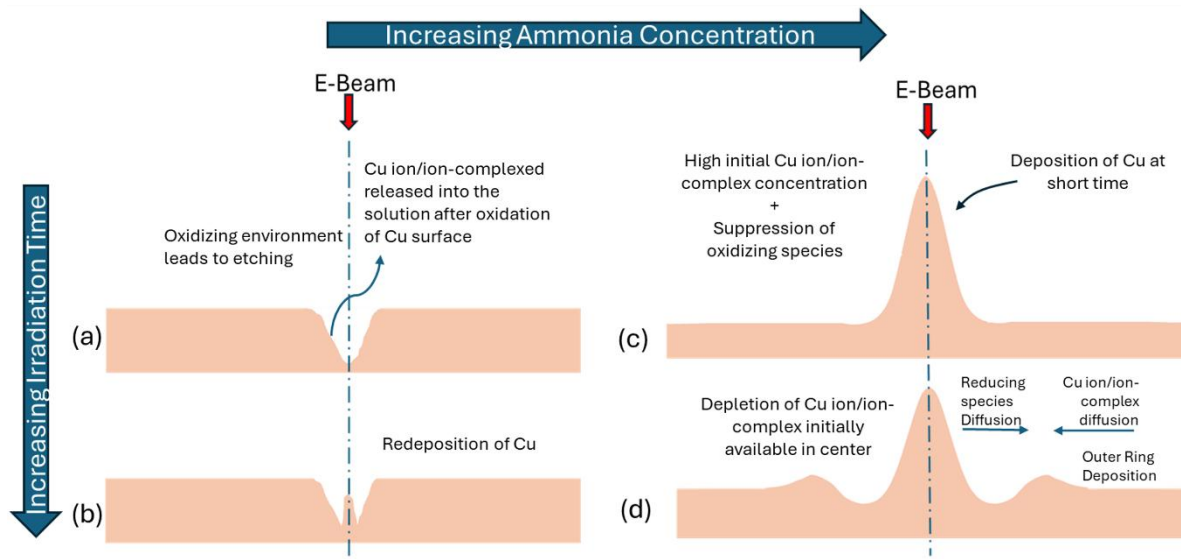


Figure 0.5 Schematic of key mechanisms underlying the process outcomes and deposit/etch evolution at varying ammonia concentrations and irradiation times. (a) At low ammonia and short times, oxidizing species dominate, leading to net copper etching. (b) As irradiation continues under low ammonia, the local concentration of copper ions/ion-complexes rises due to initial copper oxidation, causing redeposition and “peak-in-valley” nanostructure formation. (c) At high ammonia and short times, increased rate of copper-ammine complexation and a reducing environment favor rapid copper redeposition at the beam impingement site. (d) With prolonged exposure under high ammonia, the availability of copper ions/ion-complexes near the center diminishes with deposit growth, while diffusion of precursor cations from the surrounding to the e-beam irradiation site and diffusion of the reducing species outwards from the center drives ring-like structure formation.

The explanation of the system behavior for varying times and ammonia concentration, based on the dominant reaction pathways, is summarized in **Figure 4.5**. For a low-ammonia liquid film exposed to the electron beam, oxidation dominates due to a limited amount of released precursor cations and abundant oxidizing species; thus, short exposures result in surface etching, **Figure 4.5 (a)**. Prolonging the e-beam exposure increases the local concentration by accumulation of precursor cations due to oxidation of copper surface. This shifts the environment to reduction-dominant, triggering redeposition at etched sites by radiolytic solvated electrons, forming “peak-in-valley” nanostructures, **Figure 4.5 (b)**.

Conversely, high ammonia concentration yields abundant precursor cations immediately on film formation and suppresses oxidizing species concentration by ammonia quenching. As a result, even for short e-beam exposure, immediate copper deposition occurs, **Figure 4.5 (c)**. Extended e-beam irradiation depletes precursor ions, plateauing deposit growth, **Figure 4.5 (d)**. Precursor cation diffusion towards the center, coupled with solvated electron diffusion away from the center creates a ring-like deposit with the radius defined by overlap in concentration of interacting species that participate in metal-ion reduction.

To explore the possibility of metal patterning with this NESAFEBIP approach, we performed 1D line-etch experiments on a copper substrate with a 5% ammonia water nanoelectrospray film under 20 kV beam irradiation. Lines were etched by exposing a sequence of discrete spots at two different densities and dwell times. **Figure 4.6 (a)** shows the line nanostructure created by irradiating 3 spots per μm at 0.5 s per spot, and **Figure 4.6 (c)** shows the line nanostructure created by irradiating 10 spots per μm at 0.15 s per spot. Both features were imaged using backscattered electron detector at a 3 KV electron

beam energy. Corresponding AFM height profiles, **Figure. 4.6** (b,d), provide the topological structure of interconnected etched pits. At 3 spots per μm the individual pits remain separated, whereas at 10 spots per μm the pits show an overlap forming a more continuous groove. These results demonstrate that modulating ammonia concentration, spot spacing, and dwell time, we can precisely control nanostructure dimensionality and topology, transitioning from discrete zero-dimensional nano-pits or nano-pillars to continuous, higher-dimensional features.

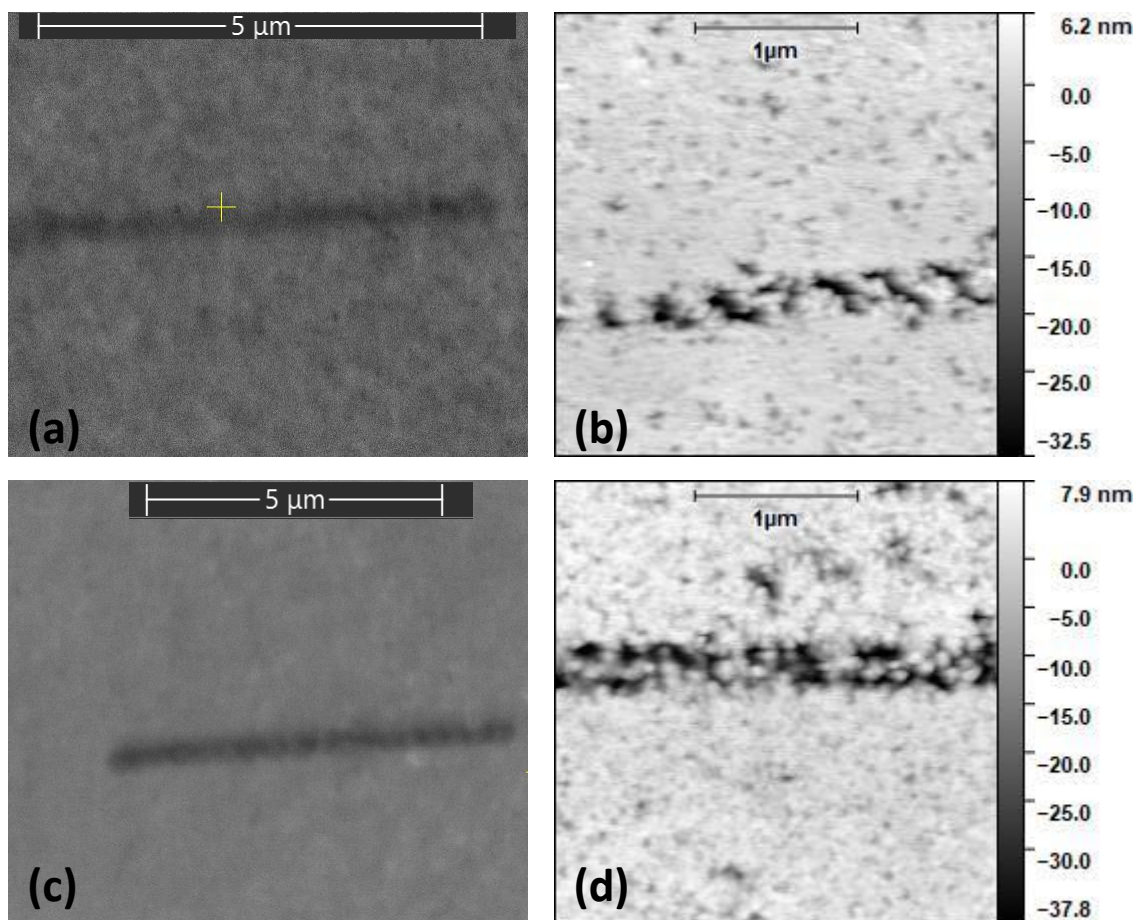


Figure 0.6 Line nanostructures on a copper substrate created with 5% ammonia-water NESAs film, using 20 kV, 2.5 nA electron beam. (a) Backscattered-electron SEM image (3 kV imaging) of a line “written” with 3 spots per μm (0.5 s dwell each). (b) AFM height profile of etched pattern (a), showing a sequence of discrete etch pits that do not fully merge. (c) Backscattered-electron SEM image of a line “written” with 10 spots per μm (0.15 s dwell each). (d) AFM profile of etched pattern (c), illustrating the etch morphology and producing an interconnected etched line.

1.15 Concluding Remarks

We demonstrate the ability to unify etching and deposition within a single electron beam guided framework by exploiting solvent-mediated redox chemistry. The interplay between ammonia concentration, radiolytic species dynamics, and transport processes enables precise spatial control over copper surface nanostructuring. At lower ammonia concentrations, oxidizing radiolytic species from e-beam irradiation dominate the process, etching the substrate, while the subsequent (longer term) accumulation of dissolved copper cations released on interaction of ammonia with copper/copper oxide substrate triggers redeposition, forming the unique peak-in-valley architectures. Conversely, higher ammonia concentration leads to copper-ammine complexation and suppression of oxidizing species, creating a reducing environment that promotes immediate deposition. Reaction-transport simulations systematically reveal how ammonia tunes the spatiotemporal balance between oxidation and reduction, enabling control over nanostructure morphology.

The key to this process lies in ammonia's multifaceted role: (a) it modulates deposition precursor availability by forming soluble copper-ammine ion-complexes, which act as reservoirs for redeposition; (b) it scavenges radiolytic oxidizing species (e.g., OH^\bullet , H_2O_2), shifting redox equilibrium; and (c) it enhances solvated electron lifetimes, favoring reduction. By coupling these effects with beam exposure duration, we establish a generalized paradigm for nanoscale surface engineering. This approach is not limited to copper-ammonia systems but can be extended to other metals and solvents where precursor complexation and selective scavenging of radiolytic intermediates can be engineered. The peak-and-valley nanostructures and their derivatives could find applications in a number

of fields from nanoscale sensing (e.g., AFM tips and AFM-SECM nanoprobes, which integrate a sharp tip for topological imaging with a peripheral ring electrode for electrochemical sensing) [79], to drug/gene delivery (e.g., the functionalized micro/nano-needle arrays for cell surface/skin piercing) [80] and genetic modification of biological cells [81], to vertical electrical interconnects in emerging 3D stacked computer chip architectures [82]. By integrating etching and deposition into a single tunable process, this strategy advances the versatility of electron beam guided nanofabrication, offering a pathway to synthesize tailored surface topographies.

CONCLUSIONS

1.16 Major Contributions and Publications

The presented PhD research explores the role that water-ammonia solvent plays in electron-beam-mediated nanostructure synthesis and modification. By demonstrating how ammonia modulates radiolysis species, each study contributes a critical piece of understanding toward a more comprehensive control and expanding the options of redox chemistry in liquid-phase focused electron beam–induced processes (LP-FEBID).

First contribution is the establishment of the chemical mechanisms how ammonia enables dual functionality of hydrogen peroxide as both the reducer and oxidizer in FEBIP with metal salt precursors by forming stable metal-ammine complexes. Addition of ammonia to water has been shown to shift the kinetics of the process toward reduction. This substantially increases the rate of deposition, relative to the purely aqueous solvent, but expands the region where deposition occurs with impact on nanostructure resolution. These original findings highlight how adjustments to the ammonia concentration can alter reaction pathways between oxidizing and reducing with implications to FEBIP capabilities.

The second contribution is introduction of the concept of an “electrochemical lens,” wherein an optimal ammonia concentration locally enhances reducing conditions in the nearfield to enhance deposition, while simultaneously keeping the farfield oxidizing and suppressing deposition. Thus, adjusting ammonia concentration effectively “focuses” the redox chemistry, allowing for both a rapid growth rate and sub-micrometer resolution.

Such a strategy can be expanded to other metal ions or even mixed-metal systems, thus opening a new promising direction for LP-FEBIP.

The third contribution is the realization of the precursor-free hybrid concept of FEBIP of metal surfaces in which ammonia can yield the simultaneous etching and deposition by electron beam that results in synthesis of unique peak-and-valley 3D nanostructures. The concept is demonstrated using copper as a substrate, which is an important material choice for applications in microelectronics. This dual capacity for localized etching and redeposition via ammonia concentration modulation can lead to greater topological flexibility of electron beam mediated nanostructure synthesis and open new applications. Overall, the result of this PhD research is a robust, versatile platform for nanoscale fabrication, capable of integrating etching and deposition in a controlled manner. The hand-in-hand use of first-principle modeling and experiments produced the fundamental insights into ammonia-mediated redox chemistry and provide a template for expanding LP-FEBID to more complex chemistries and materials, leading to improved functionality, higher throughput, and new modes of control over structure and composition at the nanoscale.

Refereed journal publications:

- Auwais Ahmed, Erik Boyle, Peter Kottke, Andrei G. Fedorov, Radiolytic redox interplay defines nanomaterial synthesis in liquids, *Science Advances*, 7, eabj8751(2021), DOI:10.1126/sciadv.abj8751

- Auwais Ahmed, Peter Kottke, Andrei G. Fedorov, Electrochemical Lensing for High Resolution Nanostructure Synthesis in Liquids, *ACS Applied Nano Materials*, 2024 7 (13), 15438-15445 DOI: 10.1021/acsnm.4c02295
- Auwais Ahmed, Andrei G. Fedorov, Peak-in-Valley Metal Nano-Architectures via E-Beam-Guided Metal Oxide Redox, *Advanced Functional Materials*, e14610(2025), DOI:10.1002/adfm.202514610

Conference Presentations

- Auwais Ahmed, Peter A. Kottke, and Andrei G. Fedorov, Solvent Dependent Metal Nanostructure Synthesis Using Focused Electron Beam, *NNCI Nano+AM Summit*, 2022, Louisville, Kentucky.
- Auwais Ahmed, Peter A. Kottke, and Andrei G. Fedorov, High resolution metal deposition using focused electron beam with redox chemistry control, *EIPBN 2024*, La Jolla, California.
- Auwais Ahmed, Andrei G. Fedorov, Focused E-Beam-Driven Liquid-Phase Surface Modification of Metals, *EIPBN 2025*, Savannah, Georgia.

1.17 Beam-Driven Effects: Key Considerations and Future Directions

1.17.1 Liquid Heating via E-Beam

Prior work has shown that focused electron beams can deposit significant energy locally into micron-scale ‘thick’ liquid films that are placed on low-thermal-conductivity, superhydrophobic surfaces. These films can retain heat and experience substantial temperature rises, when the viewing field is below $\sim 10 \mu\text{m}$ in size [83]. In our LP-FEBIP

experiments, however, the ammonia-water films are inherently much thinner, thanks to the low surface tension of the water-ammonia mixture and the nanoelectrospray delivery instead of condensation. This means that the characteristic film thickness remains below the threshold for severe beam-induced heating. Moreover, the NESA-FEBIP films used rest directly on a gold or copper coated substrate with a high thermal conductivity thus enabling heat dissipation through the substrate. Simultaneously, the continual replenishment of solution via electrospray maintains the film in a quasi-isothermal state, effectively suppressing any significant temperature increases under the beam. As a result, ignoring e-beam driven liquid heating in NESA-FEBIP is a reasonable approximation.

1.17.2 Solid Deposit Heating via E-Beam

The possibility of heating by the electron beam of the growing solid deposit itself is considered here. The electron beam can lead to high temperature gradients at atomistic scales (length-scale of inelastic mean-free path). The time-scale analysis for electron beam heating of solids, as detailed by [84], provides a quantitative framework for assessing this effect using copper as an example. The regime of heating is determined by comparing the characteristic time between electron arrivals, $\tau_s=e/I$ (where e is the elementary charge and I is the beam current), with the intrinsic relaxation times of the material's heat carriers (e.g., electron-phonon scattering time, τ_{ec-ph} , and phonon-phonon scattering time, τ_{ph}).

- If $\tau_s > \tau_{ph}$, heating is negligible.
- If $\tau_s \sim \tau_{ph}$, moderate, uniform heating occurs.
- If $\tau_s < \tau_{ec-ph}$, significant non-equilibrium heating occurs.

Applying this analysis to the experimental conditions of the dissertation reveals that the processes operate squarely within the moderate heating regime, where thermal effects due to electron beam heating of solid deposit (such thermally induced annealing and microstructure change) are expected to be minimal.

Beam Current (I)	Source Time Scale ($\tau_s=e/I$)	Material Relaxation Times
2 nA	8.0×10^{-11} s	$\tau_{ph} \sim 1.5 \times 10^{-12}$ s, $\tau_{ec-ph} \sim 2.5 \times 10^{-14}$ s

1.17.3 Axial (Across the Film) Temperature Gradients in the Liquid Film

Although evaporative cooling at the liquid–vacuum interface can, in principle, drive a temperature gradient across thicker films, our ammonia–water films remain sufficiently thin ($\Delta x \sim 1 \mu\text{m}$). To place an upper bound on the film’s temperature gradient, we begin with the Hertz–Knudsen expression for the maximum mass flux of pure water evaporating into vacuum:

$$\dot{m}''_{max} \approx p_{sat} \sqrt{\frac{M}{2\pi RT}} = 2.5 \frac{kg}{m^2 s} \quad (5.1)$$

Multiplying by the latent heat of vaporization $\Delta H_{vap} \approx 2.26 \times 10^6$ J/kg yields a maximum cooling flux,

$$q_{max} = \dot{m}''_{max} \Delta H_{vap} \approx 5.7 \times 10^6 \text{ W/m}^2 \quad (5.2)$$

$$\Delta T = \frac{q_{max}\Delta x}{k} \approx 9.5 \text{ K} \quad (5.3)$$

The temperature difference calculated in Equation 5.3 is the maximum possible axial temperature gradient that can exist in our film. In reality, the evaporation is accompanied by a constant addition of nanoelectrospray liquid, that tends to make the film quasi-isothermal. This together with the high thermal conductivity substrate (copper or gold) that dissipates heat rapidly, makes it reasonable to assume that the axial (across the film) temperature gradients in the film are negligible.

1.17.4 Electric Field Effects

In the reaction-transport model we assume bulk electroneutrality, based on the fact that any charge imbalance generated by beam-induced radiolysis is confined to a thin Debye screening layer at the solid-liquid interface. The Debye length is given by Equation 5.4,

$$\lambda_D = \sqrt{\frac{\epsilon_r \epsilon_0 k_B T}{2 N_A e^2 I}} \quad (5.4)$$

λ_D scales inversely with the square root of the ionic strength I . For our films (ionic strength $I \approx 1$ mM at 293 K, relative permittivity $\epsilon_r \approx 80$, we find $\lambda_D \lesssim 10$ nm, more than two orders of magnitude smaller than the film thickness or lateral feature sizes. Beyond this nanoscopic layer, local net charge is effectively zero and electric-field-driven migration (electromigration) can be neglected.

To get a more detailed view of electric field effects we can model the electric field with Poisson's equation. The charge density ρ is a function of the charge number, and the concentration of the species i , Equation 5.6.

$$\nabla \cdot (\epsilon \nabla \phi) = -\rho \quad (5.5)$$

$$\rho = F \sum_i z_i C_i \quad (5.6)$$

With the addition of the electric field, Equation 5.7 has to be added to the governing equation. Here, μ_i represents the electromobility of the species i .

$$J_{em} = -\mu_i z_i C_i \nabla \phi \quad (5.7)$$

1.17.5 Effects of the solid deposit presence

One important effect not yet incorporated into our model is the influence of the growing solid deposit itself on the electron-beam trajectory and resulting dose distribution. As the solid deposit nucleates, backscattering and inelastic scattering within the deposit will alter the local dose. Accurate dose calculations therefore require Monte Carlo simulations that explicitly include the evolving three-dimensional geometry and material composition of the deposit, rather than assuming a liquid medium throughout the process. Moreover, the deposit hosts non-equilibrium electrons generated by the e-beam, which can give rise to spatially varying electric potentials within the solid and at its surface. These potential gradients in turn modulate the local driving force for electrochemical reactions. Finally, as the growth on the solid surface proceeds heterogeneously, the kinetics of electron-transfer-limited metal reduction should be modeled using Marcus theory of electron transfer [85].

1.17.6 Soret (Thermophoresis) Effect

A temperature gradient within the liquid film can, in principle, induce directed motion of dissolved species, a phenomenon known as the Soret effect or thermophoresis. In this process, a concentration flux,

$$J_{i,soret} = -D S_T C_i \nabla T \quad (5.8)$$

drives species from hotter to cooler regions (for most aqueous ions, $S_T > 0$). Here, D is the molecular diffusion coefficient, C the local concentration, and S_T is the Soret coefficient. The value of S_T is typically $10^{-2} - 10^{-3} \text{ K}^{-1}$ in electrolyte [86].

To assess its significance, consider a temperature drop $\Delta T \approx 10 \text{ K}$ across a length scale of $1 \mu\text{m}$ ($\nabla T \approx 10^7 \text{ K m}^{-1}$). With $D \sim 10^{-9} \text{ m}^2/\text{s}$ at $S_T \sim 10^{-2} \text{ K}^{-1}$, the thermophoretic velocity comes out as,

$$u_T = \frac{J_{soret}}{C} = D S_T \nabla T \approx 10^{-4} \text{ m/s} \quad (5.9)$$

Using the thermophoretic velocity in a ‘Peclet-like’ number,

$$Pe_T = \frac{u_T L}{D} = 10^{-1} \quad (5.10)$$

This suggests that the Fickian diffusion dominates the transport and the thermophoretic mass transfer can be safely ignored.

1.17.7 Temperature Dependent Kinetics and Transport

Throughout this work, we have adopted a strictly isothermal domain, thereby neglecting any temperature dependence of reaction kinetics or molecular transport. Both the diffusion coefficient D and the chemical rate constants k obey Arrhenius-type relationships,

$$D(T) = D_0 \exp\left(-\frac{E_{a,diffusion}}{k_B T}\right) \quad (5.11)$$

$$k(T) = k_0 \exp\left(-\frac{E_{a,kinetics}}{k_B T}\right) \quad (5.12)$$

Here $E_{a,diffusion}$ and $E_{a,kinetics}$ are the activation energies for diffusion and kinetics, respectively. Considering heating of liquid due to the electron beam, the temperature is highest at the center of electron beam exposure. This means that the kinetics and diffusion would be fastest in the near field. As we move away, the temperature gradients become smaller, causing temperature dependent effects of kinetics and diffusion in the farfield to be negligible. A study incorporating the effects of liquid heating would need to consider temperature dependent behavior of kinetics and diffusion. This would be particularly relevant if the substrate material is substantially heated or cooled down to the cryogenic temperatures to facilitate the changes in the material synthesis conditions.

1.17.8 Growth-Rate and Deposit Crystallinity

The rate at which the deposit grows during LP-FEBIP not only dictates feature dimensions but also the atomic ordering. When the growth proceeds under the rapid, reaction-limited regime (as in the initial growth of the central pillar), atoms are generated faster than they can explore available lattice sites, leading to amorphous structures. In contrast, the slower, transport-limited growth of the peripheral ring allows the atoms sufficient time for rearrangement into low-energy configurations, yielding crystalline deposits. This link between growth rate and crystallinity was noted in our group's work on crystalline metal nanomonoliths formed by e-beam reduction of electrified nanojets [60]. In the study positive electro spray modes, containing a larger metal cation concentration and associated

with faster reduction rates, led to creation of amorphous deposits. The negative electro spray jets, containing lower concentrations of metal cations and associated with lower reduction rates, led to the creation of crystalline deposits. Potentially, the change of the substrate temperature during synthesis could be used to modulate the kinetics of the growth and induce desirable phase transformation and microstructure change.

1.18 Recommendations for future work

This dissertation establishes a roadmap for the broader application of ammonia-modulated LP-FEBID in diverse material systems. Although FEBIP with silver salt and copper exemplify two distinct behaviors, the underlying chemistry, anchored by the pivotal role of ammonia, can prove equally relevant for other precursor species. Identifying other precursor material chemistries with redox behavior modulated by ammonia (and other) solvents that follow similar competitive transport-kinetics pathways towards preferential reduction/deposition or oxidation/etching is a promising area for further inquiry.

Although the reaction-diffusion models employed for simulations in this dissertation successfully captures the main trends in liquid-phase electron-beam processing, several simplifying assumptions limit their quantitative prediction capabilities. Homogeneous reactions are used to represent both solution-phase and surface-mediated processes via an approximate proxy representation, and localized heating, fluid flow, and nucleation kinetics are neglected. While these choices allow for simulations that qualitatively capture experimental outcomes, incorporating thermal transport, more detailed surface reaction rates, and potential electric-field or flow effects would bring the theoretical framework closer to the complex realities of liquid-phase FEBIP. This would be especially useful

when LP-FEBIP reaches the level of maturity and use in applications that high fidelity CAD tools become essential for broad adaptation in industry.

APPENDIX A. KINETIC RATE CONSTANTS

Reaction	Rate Constant
$NH_3 + OH^\bullet \rightarrow NH_2^\bullet + H_2O$	$9.7 \times 10^7 \text{ M}^{-1}\text{s}^{-1}$ [87]
$NH_2^\bullet + OH^\bullet \rightarrow NH_2OH$	$9.5 \times 10^9 \text{ M}^{-1}\text{s}^{-1}$ [88]
$NH_2^\bullet + H_2O_2 \rightarrow NHOH + H_2O$	$9 \times 10^7 \text{ M}^{-1}\text{s}^{-1}$ [88]
$NH_2^\bullet + O_2 \rightarrow NH_2O_2$	$9.8 \times 10^8 \text{ M}^{-1}\text{s}^{-1}$ [76]
$2NH_2^\bullet \rightarrow N_2H_4$	$2.2 \times 10^9 \text{ M}^{-1}\text{s}^{-1}$ [88]
$N_2H_4 + OH^\bullet \rightarrow H_2O + N_2H_3$	$1 \times 10^{10} \text{ M}^{-1}\text{s}^{-1}$ [89]
$Ag^+ + 2NH_3 \rightleftharpoons Ag(NH_3)_2^+$	$K_{eq} = 1.6 \times 10^7$ [90]
$Ag^+ + e^- \rightarrow Ag$	$4 \times 10^{10} \text{ M}^{-1}\text{s}^{-1}$ [91]
$Ag(NH_3)_2^+ + e^- \rightarrow Ag + 2NH_3$	$3.2 \times 10^{10} \text{ M}^{-1}\text{s}^{-1}$ [92]
$Ag + O_2 \rightarrow Ag^+ + O_2^{\bullet -}$	$5 \times 10^9 \text{ M}^{-1}\text{s}^{-1}$ [74]
$Ag + OH^\bullet \rightarrow Ag^+ + OH^-$	$5 \times 10^9 \text{ M}^{-1}\text{s}^{-1}$ *
$Ag + H_2O_2 \rightarrow Ag^+ + 2OH^-$	$3.5 \times 10^9 \text{ M}^{-1}\text{s}^{-1}$ [74]
$Ag(NH_3)_2^+ + H_2O_2 \rightarrow Ag + 2NH_3 + H_2O + 1/2O_2$	1×10^9 [74]
$Cu^{+2} + 4NH_3 \rightleftharpoons Cu(NH_3)_4^{2+}$	$K_{eq} = 1 \times 10^{12.9}$ [78]
$Cu(NH_3)_4^{2+} + e^- \rightarrow Cu(NH_3)_4^+$	$1.8 \times 10^{10} \text{ M}^{-1}\text{s}^{-1}$ [93]
$Cu(NH_3)_4^+ + e^- \rightarrow Cu + 4NH_3$	$1.8 \times 10^{10} \text{ M}^{-1}\text{s}^{-1}$ *

$Cu^{+2} + e^{-} \rightarrow Cu^{+}$	$3.1 \times 10^{10} \text{ M}^{-1}\text{s}^{-1}$ [93]
$Cu^{+} + e^{-} \rightarrow Cu$	$2.7 \times 10^{10} \text{ M}^{-1}\text{s}^{-1}$ [93]
$e^{-} + H_2O \rightarrow H^{\bullet} + OH^{-}$	$1.9 \times 10^1 \text{ M}^{-1}\text{s}^{-1}$ [93]
$e^{-} + OH^{\bullet} \rightarrow OH^{-}$	$3 \times 10^{10} \text{ M}^{-1}\text{s}^{-1}$ [93]
$e^{-} + O^{\bullet-} \rightarrow 2OH^{-}$	$2.2 \times 10^{10} \text{ M}^{-1}\text{s}^{-1}$ [93]
$e^{-} + H_2O_2 \rightarrow OH^{-} + OH^{\bullet}$	$1.1 \times 10^{10} \text{ M}^{-1}\text{s}^{-1}$ [93]
$e^{-} + HO_2^{\bullet} \rightarrow OH^{-} + O^{\bullet-}$	$3.5 \times 10^9 \text{ M}^{-1}\text{s}^{-1}$ [93]
$e^{-} + O_2 \rightarrow O_2^{\bullet-}$	$1.9 \times 10^{10} \text{ M}^{-1}\text{s}^{-1}$ [93]
$e^{-} + O_2^{\bullet-} \rightarrow O_2^{\bullet 2-}$	$1.3 \times 10^{10} \text{ M}^{-1}\text{s}^{-1}$ [93]
$H^{\bullet} + H_2O \rightarrow H_2 + OH^{\bullet}$	$1.1 \times 10^1 \text{ M}^{-1}\text{s}^{-1}$ [93]
$H^{\bullet} + H^{\bullet} \rightarrow H_2$	$2k=1.55 \times 10^{10} \text{ M}^{-1}\text{s}^{-1}$ [93]
$H^{\bullet} + OH^{\bullet} \rightarrow H_2O$	$7 \times 10^9 \text{ M}^{-1}\text{s}^{-1}$ [93]
$H^{\bullet} + H_2O_2 \rightarrow OH^{\bullet} + H_2O$	$9 \times 10^7 \text{ M}^{-1}\text{s}^{-1}$ [93]
$H^{\bullet} + O_2 \rightarrow HO_2^{\bullet}$	$2.1 \times 10^{10} \text{ M}^{-1}\text{s}^{-1}$ [93]
$H^{\bullet} + HO_2^{\bullet} \rightarrow H_2O_2$	$1 \times 10^{10} \text{ M}^{-1}\text{s}^{-1}$ [93]
$OH^{\bullet} + OH^{\bullet} \rightarrow H_2O_2$	$2k=1.1 \times 10^{10} \text{ M}^{-1}\text{s}^{-1}$ [93]
$OH^{\bullet} + O^{\bullet-} \rightarrow HO_2^{-}$	$2 \times 10^{10} \text{ M}^{-1}\text{s}^{-1}$ [93]
$OH^{\bullet} + H_2 \rightarrow H^{\bullet} + H_2O$	$4.2 \times 10^7 \text{ M}^{-1}\text{s}^{-1}$ [93]
$OH^{\bullet} + OH^{-} \rightarrow O^{\bullet-} + H_2O$	$1.3 \times 10^{10} \text{ M}^{-1}\text{s}^{-1}$ [93]

$OH^\bullet + HO_2^\bullet \rightarrow H_2O + O_2^\bullet$	$6 \times 10^9 \text{ M}^{-1}\text{s}^{-1}$ [93]
$OH^\bullet + O_2^{\bullet-} \rightarrow OH^- + O_2$	$8 \times 10^9 \text{ M}^{-1}\text{s}^{-1}$ [93]
$O^{\bullet-} + H_2 \rightarrow H^\bullet + OH^-$	$8 \times 10^7 \text{ M}^{-1}\text{s}^{-1}$ [93]
$O^{\bullet-} + H_2O_2 \rightarrow O_2^{\bullet-} + H_2O$	$5 \times 10^8 \text{ M}^{-1}\text{s}^{-1}$ [93]
$O^{\bullet-} + HO_2^- \rightarrow O_2^{\bullet-} + OH^-$	$4 \times 10^8 \text{ M}^{-1}\text{s}^{-1}$ [93]
$O^{\bullet-} + O_2 \rightarrow O_3^-$	$3.6 \times 10^9 \text{ M}^{-1}\text{s}^{-1}$ [93]
$O^{\bullet-} + O_2^{\bullet-} \rightarrow 2OH^- + O_2$	$6 \times 10^8 \text{ M}^{-1}\text{s}^{-1}$ [93]
$O_3 + OH^\bullet \rightarrow HO_2^\bullet + O_2$	$1.1 \times 10^9 \text{ M}^{-1}\text{s}^{-1}$ [94]
$O_3 + e^- \rightarrow O_3^{\bullet-}$	$3.6 \times 10^{10} \text{ M}^{-1}\text{s}^{-1}$ [95]
$OH^\bullet + H_2O_2 \rightarrow OH^- + O_2^{\bullet-}$	$2.7 \times 10^7 \text{ M}^{-1}\text{s}^{-1}$ [93]
$OH^- + H_2O_2 \rightarrow OH^- + O_2^{\bullet-}$	$1.3 \times 10^{10} \text{ M}^{-1}\text{s}^{-1}$ *
$O_3 + H^\bullet \rightarrow O_2 + OH^\bullet$	$1.2 \times 10^{10} \text{ M}^{-1}\text{s}^{-1}$ [95]
$O_2 + H^\bullet \rightarrow O_2 + OH^\bullet$	$2.1 \times 10^{10} \text{ M}^{-1}\text{s}^{-1}$ [96]
$HO_2^\bullet + H^\bullet \rightarrow H_2O_2$	$1 \times 10^{10} \text{ M}^{-1}\text{s}^{-1}$ [97]
$H^+ + OH^- \rightleftharpoons H_2O$	$K_w = 1 \times 10^{-14}$ [98]
$H^+ + HO_2^- \rightleftharpoons H_2O_2$	$K_a = 2.2 \times 10^{-12}$ [98]
$H^+ + O^- \rightleftharpoons OH$	$K_a = 1.3 \times 10^{-12}$ [98]
$H^+ + e^- \rightleftharpoons H$	$K_a = 1.7 \times 10^{-10}$ [98]
$H^+ + O_2^- \rightleftharpoons HO_2$	$K_a = 2.7 \times 10^{-5}$ [98]

$HO_2^- + H^\bullet \rightarrow OH^- + OH^\bullet$	$1.2 \times 10^9 \text{ M}^{-1} \text{ s}^{-1}$ [96]
$HO_2^\bullet + HO_2^\bullet \rightarrow O_2 + H_2O_2$	$8.3 \times 10^5 \text{ M}^{-1} \text{ s}^{-1}$ [99]
$H_2O + O^{\bullet -} \rightarrow OH^- + OH^\bullet$	$9.3 \times 10^7 \text{ M}^{-1} \text{ s}^{-1}$ [100]
$O^{\bullet -} + H_2 \rightarrow e^- + H_2O$	$1.8 \times 10^8 \text{ M}^{-1} \text{ s}^{-1}$ [101]

*Estimate

APPENDIX B.G-VALUES

G-Values Water

The G-Values for pure water [56] are given below in units of molecules created per 100 eV energy deposited.

Species	G-Value (molecules/ 100 eV)
e_{sol}^-	3.47
H^\bullet	1.00
OH^\bullet	3.63
H_2O_2	0.47
H_2	0.17
HO_2^\bullet	0.08
H_3O^+	4.42
OH^-	0.95

G-Values Ammonia

The G-Values of ammonia [102] are given below,

Species	G-Value (molecules/ 100 eV)
NH_2^\bullet	4.80
H^\bullet	4.80

H ₂	3.58
N ₂	1.00
N ₂ H ₄	0.58

For a w_{NH_3} ammonia mass fraction in the solution, G-values used for radiolysis species i of aqueous-ammonia system were calculated as follows,

$$G_i(solution) = (1 - w_{NH_3})G_i^{water} + (w_{NH_3})G_i^{NH_3}$$

APPENDIX C. DIFFUSION COEFFICIENTS

Diffusion coefficients extracted from [56], unless specified otherwise.

Species	D (m ² /s)
e_{sol}^-	4.5×10^{-9}
OH^-	5×10^{-9}
H_2O_2	1.4×10^{-9}
HO_2^-	1.4×10^{-9}
H^\bullet	7×10^{-9}
OH^\bullet	2.8×10^{-9}
HO_2^\bullet	2×10^{-9}
$O_2^{\bullet-}$	2.1×10^{-9}
$O^{\bullet-}$	2.8×10^{-9}
O_3	1.89×10^{-9}
NH_2^\bullet	$1.5 \times 10^{-9} *$
NH_3	1.5×10^{-9} [103]

Ag^+	1.65×10^{-9} [104]
$Ag(NH_3)_2^+$	1.5×10^{-9} [105]
$Cu(NH_3)_4^+$	2.09×10^{-9} [106]

*Estimate

REFERENCES

- [1] V. Reisecker, R. Winkler, and H. Plank, "A Review on Direct-Write Nanoprinting of Functional 3D Structures with Focused Electron Beams," *Advanced Functional Materials*, vol. 34, no. 46, p. 2407567, 2024, doi: <https://doi.org/10.1002/adfm.202407567>.
- [2] S. Kim and A. G. Fedorov, "FEBIP for functional nanolithography of 2D," in *Nanofabrication: Nanolithography techniques and their applications*: IOP Publishing Ltd, 2020, pp. 12-1 to 12-26.
- [3] A. G. Fedorov, S. Kim, M. Henry, D. Kulkarni, and V. V. Tsukruk, "Focused-electron-beam-induced processing (FEBIP) for emerging applications in carbon nanoelectronics," *Applied Physics A*, vol. 117, no. 4, pp. 1659-1674, 2014.
- [4] S. Jesse *et al.*, "Directing Matter: Toward Atomic-Scale 3D Nanofabrication," *ACS Nano*, vol. 10, no. 6, pp. 5600-5618, 2016/06/28 2016, doi: [10.1021/acsnano.6b02489](https://doi.org/10.1021/acsnano.6b02489).
- [5] R. Winkler, J. D. Fowlkes, P. D. Rack, and H. Plank, "3D nanoprinting via focused electron beams," *Journal of Applied Physics*, vol. 125, no. 21, p. 210901, 2019, Art no. 210901, doi: [10.1063/1.5092372](https://doi.org/10.1063/1.5092372).
- [6] I. Utke, S. Moshkalev, and P. Russell, *Nanofabrication using focused ion and electron beams: principles and applications*. Oxford University Press, 2012.
- [7] X. Wei, M. S. Wang, Y. Bando, and D. Golberg, "Electron-beam-induced substitutional carbon doping of boron nitride nanosheets, nanoribbons, and nanotubes," (in eng), *ACS Nano*, vol. 5, no. 4, pp. 2916-22, Apr 26 2011, doi: [10.1021/nn103548r](https://doi.org/10.1021/nn103548r).
- [8] S. Kim *et al.*, "Dynamic modulation of electronic properties of graphene by localized carbon doping using focused electron beam induced deposition," *Nanoscale*, [10.1039/C5NR04063A](https://doi.org/10.1039/C5NR04063A) vol. 7, no. 36, pp. 14946-14952, 2015, doi: [10.1039/C5NR04063A](https://doi.org/10.1039/C5NR04063A).
- [9] S. Du *et al.*, "Strain lithography for two-dimensional materials by electron irradiation," *Applied Physics Letters*, vol. 120, no. 9, 2022, doi: [10.1063/5.0082556](https://doi.org/10.1063/5.0082556).
- [10] A. Antony *et al.*, "Defect engineering, microstructural examination and improvement of ultrafast third harmonic generation in GaZnO nanostructures: a study of e-beam irradiation," *Physical Chemistry Chemical Physics*, [10.1039/C9CP06323D](https://doi.org/10.1039/C9CP06323D) vol. 22, no. 7, pp. 4252-4265, 2020, doi: [10.1039/C9CP06323D](https://doi.org/10.1039/C9CP06323D).

- [11] C. Magén, J. Pablo-Navarro, and J. M. De Teresa, "Focused-Electron-Beam Engineering of 3D Magnetic Nanowires," *Nanomaterials*, vol. 11, no. 2, p. 402, 2021. [Online]. Available: <https://www.mdpi.com/2079-4991/11/2/402>.
- [12] I. Utke and A. Götzhäuser, "Small, Minimally Invasive, Direct: Electrons Induce Local Reactions of Adsorbed Functional Molecules on the Nanoscale," *Angewandte Chemie International Edition*, vol. 49, no. 49, pp. 9328-9330, 2010, doi: <https://doi.org/10.1002/anie.201002677>.
- [13] F. P. Michael Huth, Christian Schwalb, Marcel Winhold, Roland Sachser, Maja Dukic, Jonathan Adams, Georg Fantner, "Focused electron beam induced deposition: A perspective," *Beilstein J. Nanotechnology*, vol. 3, pp. 597–619, 2012.
- [14] S. Randolph, J. Fowlkes, and P. Rack, "Focused, nanoscale electron-beam-induced deposition and etching," *Critical reviews in solid state and materials sciences*, vol. 31, no. 3, pp. 55-89, 2006.
- [15] I. Utke *et al.*, "Coordination and organometallic precursors of group 10 and 11: Focused electron beam induced deposition of metals and insight gained from chemical vapour deposition, atomic layer deposition, and fundamental surface and gas phase studies," *Coordination Chemistry Reviews*, vol. 458, p. 213851, 2022/05/01/ 2022, doi: <https://doi.org/10.1016/j.ccr.2021.213851>.
- [16] R. Winkler *et al.*, "Additive Manufacturing of Co(3)Fe Nano-Probes for Magnetic Force Microscopy," (in eng), *Nanomaterials (Basel)*, vol. 13, no. 7, Mar 29 2023, doi: [10.3390/nano13071217](https://doi.org/10.3390/nano13071217).
- [17] S. Barth *et al.*, "Nanoscale, surface-confined phase separation by electron beam induced oxidation," *Nanoscale*, vol. 16, 06/26 2024, doi: [10.1039/D4NR01650E](https://doi.org/10.1039/D4NR01650E).
- [18] K. Rykaczewski, A. Marshall, W. B. White, and A. G. Fedorov, "Dynamic growth of carbon nanopillars and microrings in electron beam induced dissociation of residual hydrocarbons," *Ultramicroscopy*, vol. 108, no. 9, pp. 989-992, 2008/08/01/ 2008, doi: <https://doi.org/10.1016/j.ultramic.2008.04.006>.
- [19] M. M. Shawrav *et al.*, "Mask-free prototyping of metal-oxide-semiconductor devices utilizing focused electron beam induced deposition," *physica status solidi (a)*, vol. 211, no. 2, pp. 375-381, 2014, doi: <https://doi.org/10.1002/pssa.201330133>.
- [20] M. R. Henry and A. G. Fedorov, "Adaptive simulations enable computational design of electron beam processing of nanomaterials with supersonic micro-jet precursor," *Computational Materials Science*, vol. 186, p. 109993, 2021.
- [21] S. Kim, M. Henry, Y. H. Moon, and A. G. Fedorov, "Multimode jetting unlocks a trade-off between nanostructure morphology and composition in focused electron beam induced deposition," *Materials Today Communications*, vol. 21, p. 100645, 2019.

- [22] M. R. Henry, S. Kim, and A. G. Fedorov, "Non-equilibrium adatom thermal state enables rapid additive nanomanufacturing," *Physical Chemistry Chemical Physics*, vol. 21, no. 20, pp. 10449-10456, 2019.
- [23] J. Pablo-Navarro, S. Sangiao, C. Magén, and J. M. De Teresa, "Focused electron beam induced deposition," *Nanofabrication*: IOP Publishing, 2020, pp. 4-1-4-39. [Online]. Available: <https://dx.doi.org/10.1088/978-0-7503-2608-7ch4>
- [24] K. Höflich *et al.*, "Direct Electron Beam Writing of Silver-Based Nanostructures," *ACS Applied Materials & Interfaces*, vol. 9, no. 28, pp. 24071-24077, 2017/07/19 2017, doi: 10.1021/acsami.7b04353.
- [25] L. Berger *et al.*, "Gas-assisted silver deposition with a focused electron beam," *Beilstein J Nanotechnol*, vol. 9, pp. 224-232, // 2018, doi: 10.3762/bjnano.9.24.
- [26] J. Lasseter, P. D. Rack, and S. J. Randolph, "Selected Area Deposition of High Purity Gold for Functional 3D Architectures," *Nanomaterials*, vol. 13, no. 4, p. 757, 2023. [Online]. Available: <https://www.mdpi.com/2079-4991/13/4/757>.
- [27] C. Haverkamp *et al.*, "A novel copper precursor for electron beam induced deposition," *Beilstein J Nanotechnol*, vol. 9, pp. 1220-1227, // 2018, doi: 10.3762/bjnano.9.113.
- [28] J. Jurczyk *et al.*, "Focused Electron Beam-Induced Deposition and Post-Growth Purification Using the Heteroleptic Ru Complex ($\eta^3\text{-C}_3\text{H}_5$)Ru(CO)₃Br," *ACS Applied Materials & Interfaces*, vol. 11, no. 31, pp. 28164-28171, 2019/08/07 2019, doi: 10.1021/acsami.9b07634.
- [29] F. Schoenaker *et al.*, "Focused electron beam induced etching of titanium with XeF₂," *Nanotechnology*, vol. 22, no. 26, p. 265304, 2011.
- [30] A. Ganczarczyk, M. Geller, and A. Lorke, "XeF₂ gas-assisted focused-electron-beam-induced etching of GaAs with 30 nm resolution," *Nanotechnology*, vol. 22, p. 045301, 01/28 2011, doi: 10.1088/0957-4484/22/4/045301.
- [31] P. Roediger, G. Hochleitner, E. Bertagnolli, H. Wanzenboeck, and W. Buehler, "Focused electron beam induced etching of silicon using chlorine," *Nanotechnology*, vol. 21, no. 28, p. 285306, 2010.
- [32] R. Winkler *et al.*, "Direct-Write 3D Nanoprinting of Plasmonic Structures," *ACS Applied Materials & Interfaces*, vol. 9, no. 9, pp. 8233-8240, 2017/03/08 2017, doi: 10.1021/acsami.6b13062.
- [33] D. Kuhness *et al.*, "High-Fidelity 3D Nanoprinting of Plasmonic Gold Nanoantennas," *ACS Applied Materials & Interfaces*, vol. 13, 12/29 2020, doi: 10.1021/acsami.0c17030.

- [34] P. H. I Utke, J Melngailis, "Gas-assisted focused electron beam and ion beam processing and fabrication," *Journal of Vacuum Science & Technology B: Microelectronics and Nanometer Structures Processing*, vol. 26, 2008.
- [35] P. A. K. J.S.Fisher, A.G.Fedorov, "Synthesis of crystalline metal nanomonoliths by e-beam reduction of negatively electrified jets," *Materials Today Physics*, vol. 5, 2018.
- [36] A. Ahmed, E. C. Boyle, P. A. Kottke, and A. G. Fedorov, "Radiolytic redox interplay defines nanomaterial synthesis in liquids," *Science Advances*, vol. 7, no. 51, p. eabj8751, 2021, doi: doi:10.1126/sciadv.abj8751.
- [37] T. Gupta, N. M. Schneider, J. H. Park, D. Steingart, and F. M. Ross, "Spatially dependent dose rate in liquid cell transmission electron microscopy," *Nanoscale*, 10.1039/C8NR01935E vol. 10, no. 16, pp. 7702-7710, 2018, doi: 10.1039/C8NR01935E.
- [38] N. Áde Jonge, "Electron beam induced chemistry of gold nanoparticles in saline solution," *Chemical Communications*, vol. 51, no. 91, pp. 16393-16396, 2015.
- [39] L. E. Ocola *et al.*, "Growth characterization of electron-beam-induced silver deposition from liquid precursor," *Journal of Vacuum Science & Technology B*, vol. 30, no. 6, p. 06FF08, 2012, doi: 10.1116/1.4765629.
- [40] E. U. Donev and J. T. Hastings, "Electron-Beam-Induced Deposition of Platinum from a Liquid Precursor," *Nano Letters*, vol. 9, no. 7, pp. 2715-2718, 2009/07/08 2009, doi: 10.1021/nl9012216.
- [41] M. Bresin, A. Chamberlain, E. U. Donev, C. B. Samantaray, G. S. Schardien, and J. T. Hastings, "Electron-beam-induced deposition of bimetallic nanostructures from bulk liquids," *Angewandte Chemie*, vol. 125, no. 31, pp. 8162-8165, 2013.
- [42] S. Esfandiarpour, L. Boehme, and J. T. Hastings, "Focused electron beam induced deposition of copper with high resolution and purity from aqueous solutions," *Nanotechnology*, vol. 28, no. 12, p. 125301, 2017.
- [43] M. Bresin, A. Botman, S. J. Randolph, M. Straw, and J. T. Hastings, "Liquid Phase Electron-Beam-Induced Deposition on Bulk Substrates Using Environmental Scanning Electron Microscopy," *Microscopy and Microanalysis*, vol. 20, no. 2, pp. 376-384, 2014, doi: 10.1017/s1431927614000117.
- [44] S. J. Randolph, A. Botman, and M. Toth, "Capsule-free fluid delivery and beam-induced electrodeposition in a scanning electron microscope," *RSC advances*, vol. 3, no. 43, pp. 20016-20023, 2013.
- [45] P. A. K. Jeffrey S. Fisher, Songkil Kim, and Andrei G. Fedorov, "Rapid Electron Beam Writing of Topologically Complex 3D Nanostructures Using Liquid Phase Precursor," *Nano Letters*, vol. 15, no. 12, 2015.

- [46] A. Ahmed, P. A. Kottke, and A. G. Fedorov, "Electrochemical Lensing for High Resolution Nanostructure Synthesis in Liquids," *ACS Applied Nano Materials*, vol. 7, no. 13, pp. 15438-15445, 2024/07/12 2024, doi: 10.1021/acsanm.4c02295.
- [47] S. K. Lami, A. P. Kaphle, N. J. Briot, A. Botman, and J. T. Hastings, "Nanoscale focused electron beam induced etching of nickel using a liquid reactant," *Nanotechnology*, vol. 31, no. 42, p. 425301, 2020.
- [48] S. K. Lami, G. Smith, E. Cao, and J. T. Hastings, "The radiation chemistry of focused electron-beam induced etching of copper in liquids," *Nanoscale*, vol. 11, no. 24, pp. 11550-11561, 2019.
- [49] L. Boehme, M. Bresin, A. Botman, J. Ranney, and J. T. Hastings, "Focused electron beam induced etching of copper in sulfuric acid solutions," *Nanotechnology*, vol. 26, no. 49, p. 495301, 2015/11/16 2015, doi: 10.1088/0957-4484/26/49/495301.
- [50] T. Buttersack *et al.*, "Photoelectron spectra of alkali metal–ammonia microjets: From blue electrolyte to bronze metal," *Science*, vol. 368, no. 6495, p. 1086, 2020, doi: 10.1126/science.aaz7607.
- [51] U. Schindewolf and P. Wünschel, "Comparison of solvated electron reaction rates in water and ammonia," 1977.
- [52] I. G. Gonzalez-Martinez *et al.*, "Electron-beam induced synthesis of nanostructures: a review," *Nanoscale*, 10.1039/C6NR01941B vol. 8, no. 22, pp. 11340-11362, 2016, doi: 10.1039/C6NR01941B.
- [53] E. Longo, W. Avansi, J. Bettini, J. Andrés, and L. Gracia, "In situ Transmission Electron Microscopy observation of Ag nanocrystal evolution by surfactant free electron-driven synthesis," *Scientific Reports*, vol. 6, no. 1, p. 21498, 2016/03/16 2016, doi: 10.1038/srep21498.
- [54] Z. Wang *et al.*, "Catalyst Preparation with Plasmas: How Does It Work?," *ACS Catalysis*, vol. 8, no. 3, pp. 2093-2110, 2018/03/02 2018, doi: 10.1021/acscatal.7b03723.
- [55] J. S. Fisher, P. A. Kottke, S. Kim, and A. G. Fedorov, "Rapid Electron Beam Writing of Topologically Complex 3D Nanostructures Using Liquid Phase Precursor," *Nano Letters*, vol. 15, no. 12, pp. 8385-8391, 2015/12/09 2015, doi: 10.1021/acs.nanolett.5b04225.
- [56] N. M. Schneider, M. M. Norton, B. J. Mendel, J. M. Grogan, F. M. Ross, and H. H. Bau, "Electron–Water Interactions and Implications for Liquid Cell Electron Microscopy," *The Journal of Physical Chemistry C*, vol. 118, no. 38, pp. 22373-22382, 2014/09/25 2014, doi: 10.1021/jp507400n.
- [57] M. Bresin, A. Chamberlain, E. U. Donev, C. B. Samantaray, G. S. Schardien, and J. T. Hastings, "Electron-Beam-Induced Deposition of Bimetallic Nanostructures

- from Bulk Liquids," *Angewandte Chemie International Edition*, vol. 52, no. 31, pp. 8004-8007, 2013, doi: <https://doi.org/10.1002/anie.201303740>.
- [58] G. Schardein, E. Donev, and J. Hastings, "Electron-beam-induced deposition of gold from aqueous solutions," *Nanotechnology*, vol. 22, p. 015301, 01/07 2011, doi: 10.1088/0957-4484/22/1/015301.
- [59] U. Schindewolf and P. Wünschel, "Comparison of solvated electron reaction rates in water and ammonia," *Canadian Journal of Chemistry*, vol. 55, no. 11, pp. 2159-2164, 1977, doi: 10.1139/v77-299.
- [60] J. S. Fisher, P. A. Kottke, and A. G. Fedorov, "Synthesis of crystalline metal nanomaterials by e-beam reduction of negatively electrified jets," *Materials Today Physics*, vol. 5, pp. 87-92, 2018/06/01/ 2018, doi: <https://doi.org/10.1016/j.mtphys.2018.06.006>.
- [61] J. Hermannsdörfer, N. de Jonge, and A. Verch, "Electron beam induced chemistry of gold nanoparticles in saline solution," *Chemical Communications*, 10.1039/C5CC06812F vol. 51, no. 91, pp. 16393-16396, 2015, doi: 10.1039/C5CC06812F.
- [62] T. J. Woehl and P. Abellan, "Defining the radiation chemistry during liquid cell electron microscopy to enable visualization of nanomaterial growth and degradation dynamics," *Journal of Microscopy*, <https://doi.org/10.1111/jmi.12508> vol. 265, no. 2, pp. 135-147, 2017/02/01 2017, doi: <https://doi.org/10.1111/jmi.12508>.
- [63] T. Kraus and N. de Jonge, "Dendritic Gold Nanowire Growth Observed in Liquid with Transmission Electron Microscopy," *Langmuir*, vol. 29, no. 26, pp. 8427-8432, 2013/07/02 2013, doi: 10.1021/la401584z.
- [64] W. W. Mullins and R. F. Sekerka, "Morphological Stability of a Particle Growing by Diffusion or Heat Flow," *Journal of Applied Physics*, vol. 34, no. 2, pp. 323-329, 1963, doi: 10.1063/1.1702607.
- [65] T.-H. Fan and A. G. Fedorov, "Electrohydrodynamics and Surface Force Analysis in AFM Imaging of a Charged, Deformable Biological Membrane in a Dilute Electrolyte Solution," *Langmuir*, vol. 19, no. 26, pp. 10930-10939, 2003/12/01 2003, doi: 10.1021/la035663j.
- [66] R. E. H. J. A. Manion, R. D. Levin, D. R. Burgess Jr., V. L. Orkin, W. Tsang, W. S. McGivern, J. W. Hudgens, V. D. Knyazev, D. B. Atkinson, E. Chai, A. M. Tereza, C.-Y. Lin, T. C. Allison, W. G. Mallard, F. Westley, J. T. Herron, R. F. Hampson, and D. H. Frizzell, "NIST Chemical Kinetics Database," in *NIST Standard Reference Database 17* vol. Version 7.0 (Web Version), Release 1.6.8, Data version 2015.09, ed. Web address: <https://kinetics.nist.gov/>: National Institute of Standards and Technology, Gaithersburg, Maryland, 20899-8320. .

- [67] D. C. Joy and S. Luo, "An empirical stopping power relationship for low-energy electrons," *Scanning*, vol. 11, no. 4, pp. 176-180, 1989, doi: <https://doi.org/10.1002/sca.4950110404>.
- [68] H. T. Nguyen-Truong, "Modified Bethe formula for low-energy electron stopping power without fitting parameters," *Ultramicroscopy*, vol. 149, pp. 26-33, 2015/02/01/ 2015, doi: <https://doi.org/10.1016/j.ultramic.2014.11.003>.
- [69] A. Bejan, "Convection Heat Transfer," in *Convection Heat Transfer*, 2 ed.: John Wiley & Sons, 1994.
- [70] J. Cazaux, "Some considerations on the electric field induced in insulators by electron bombardment," *Journal of Applied Physics*, vol. 59, no. 5, pp. 1418-1430, 1986, doi: 10.1063/1.336493.
- [71] E. Strelcov *et al.*, "Nanoscale Mapping of the Double Layer Potential at the Graphene–Electrolyte Interface," *Nano Letters*, vol. 20, no. 2, pp. 1336-1344, 2020/02/12 2020, doi: 10.1021/acs.nanolett.9b04823.
- [72] G. Buxton, "The radiation chemistry of liquid water: principles and applications," in *Charged particle and photon interactions with matter*: CRC Press, 2003, pp. 338-370.
- [73] V. A. Grachev and A. B. Sazonov, "Radiolysis of Aqueous Ammonia Solutions: Mathematical Modeling," *High Energy Chemistry*, vol. 55, no. 6, pp. 472-481, 2021/11/01 2021, doi: 10.1134/S0018143921060072.
- [74] R. Tausch-Treml, A. Henglein, and J. Lilie, "Reactivity of Silver Atoms in Aqueous Solution II. A Pulse Radiolysis Study," *Berichte der Bunsengesellschaft für physikalische Chemie*, vol. 82, no. 12, pp. 1335-1343, 1978, doi: <https://doi.org/10.1002/bbpc.19780821213>.
- [75] M. Nishimoto, S. Abe, and T. Yonezawa, "Preparation of Ag nanoparticles using hydrogen peroxide as a reducing agent," *New Journal of Chemistry*, 10.1039/C8NJ01747F vol. 42, no. 17, pp. 14493-14501, 2018, doi: 10.1039/C8NJ01747F.
- [76] V. B. Men'kin, I. E. Makarov, and A. K. Pikaev, "Pulse radiolysis study of reaction rates of OH and O- radicals with ammonia in aqueous solutions," *High Energy Chemistry (English Translation)*, vol. 22, no. 5, pp. 333-336, 1989. [Online]. Available: http://inis.iaea.org/search/search.aspx?orig_q=RN:21034982.
- [77] R. W. Lane and H. J. McDonald, "Kinetics of the Reaction between Copper and Aqueous Ammonia1," *Journal of the American Chemical Society*, vol. 68, no. 9, pp. 1699-1704, 1946/09/01 1946, doi: 10.1021/ja01213a005.
- [78] J. Vazquez-Arenas, I. Lazaro, and R. Cruz, "Electrochemical study of binary and ternary copper complexes in ammonia-chloride medium," *Electrochimica Acta*,

vol. 52, no. 20, pp. 6106-6117, 2007/06/10/ 2007, doi: <https://doi.org/10.1016/j.electacta.2007.03.062>.

- [79] J. Velmurugan, A. Agrawal, S. An, E. Choudhary, and V. A. Szalai, "Fabrication of Scanning Electrochemical Microscopy-Atomic Force Microscopy Probes to Image Surface Topography and Reactivity at the Nanoscale," *Analytical Chemistry*, vol. 89, no. 5, pp. 2687-2691, 2017/03/07 2017, doi: 10.1021/acs.analchem.7b00210.
- [80] V. Alimardani *et al.*, "Microneedle Arrays Combined with Nanomedicine Approaches for Transdermal Delivery of Therapeutics," *Journal of Clinical Medicine*, vol. 10, no. 2, p. 181, 2021. [Online]. Available: <https://www.mdpi.com/2077-0383/10/2/181>.
- [81] K. J. Yee Mon *et al.*, "Functionalized nanowires for miRNA-mediated therapeutic programming of naïve T cells," *Nature Nanotechnology*, vol. 19, no. 8, pp. 1190-1202, 2024/08/01 2024, doi: 10.1038/s41565-024-01649-7.
- [82] W. Saeed *et al.*, "Nanostructured compliant interconnections for advanced Micro-Electronic packaging," *Materials & Design*, vol. 244, p. 113166, 2024/08/01/ 2024, doi: <https://doi.org/10.1016/j.matdes.2024.113166>.
- [83] K. Rykaczewski, J. H. J. Scott, and A. G. Fedorov, "Electron beam heating effects during environmental scanning electron microscopy imaging of water condensation on superhydrophobic surfaces," *Applied Physics Letters*, vol. 98, no. 9, 2011, doi: 10.1063/1.3560443.
- [84] A. G. Fedorov, K. Rykaczewski, and W. B. White, "Transport issues in focused electron beam chemical vapor deposition," *Surface and Coatings Technology*, vol. 201, no. 22, pp. 8808-8812, 2007/09/25/ 2007, doi: <https://doi.org/10.1016/j.surfcoat.2007.04.031>.
- [85] T. P. Silverstein, "Marcus Theory: Thermodynamics CAN Control the Kinetics of Electron Transfer Reactions," *Journal of Chemical Education*, vol. 89, no. 9, pp. 1159-1167, 2012/08/14 2012, doi: 10.1021/ed1007712.
- [86] H. Xie, C. Zhang, M. Sedighi, H. R. Thomas, and Y. Chen, "An analytical model for diffusion of chemicals under thermal effects in semi-infinite porous media," *Computers and Geotechnics*, vol. 69, pp. 329-337, 2015/09/01/ 2015, doi: <https://doi.org/10.1016/j.compgeo.2015.06.012>.
- [87] B. Hickel and K. Sehested, "Reaction of hydroxyl radicals with ammonia in liquid water at elevated temperatures," *International Journal of Radiation Applications and Instrumentation. Part C. Radiation Physics and Chemistry*, vol. 39, no. 4, pp. 355-357, 1992/04/01/ 1992, doi: [https://doi.org/10.1016/1359-0197\(92\)90244-A](https://doi.org/10.1016/1359-0197(92)90244-A).
- [88] P. B. Pagsberg, "Investigation of the NH₂ radical produced by pulse radiolysis of ammonia in aqueous solution," *Aspects of Research at Risø*, vol. 5, p. 209, 1972.

- [89] G. V. Buxton and C. R. Stuart, "Radiation chemistry of aqueous solutions of hydrazine at elevated temperatures. Part 1.—Oxygen-free solutions," *Journal of the Chemical Society, Faraday Transactions*, vol. 92, no. 9, pp. 1519-1525, 1996.
- [90] "CRC Handbook of Chemistry and Physics, 88th ed Editor-in-Chief: David R. Lide (National Institute of Standards and Technology) CRC Press/Taylor & Francis Group: Boca Raton, FL. 2007. 2640 pp. \$139.95. ISBN 0-8493-0488-1," *Journal of the American Chemical Society*, vol. 130, no. 1, pp. 382-382, 2008/01/01 2008, doi: 10.1021/ja077011d.
- [91] R. Chen, Y. Avotinsh, and G. R. Freeman, "Solvent effects on the reactivity of solvated electrons with ions in isobutanol/water mixed solvents," *Canadian Journal of Chemistry*, vol. 72, no. 4, pp. 1083-1093, 1994, doi: 10.1139/v94-137.
- [92] J. Pukies and W. Roebke, "Pulsradiolytische Untersuchung der Reduktion des Ag⁺-Ions in ammoniakalischer Lösung," *Berichte der Bunsengesellschaft für physikalische Chemie*, vol. 72, no. 9-10, pp. 1101-1105, 1968, doi: <https://doi.org/10.1002/bbpc.19680720909>.
- [93] G. V. Buxton, C. L. Greenstock, W. P. Helman, and A. B. Ross, "Critical Review of rate constants for reactions of hydrated electrons, hydrogen atoms and hydroxyl radicals ($\cdot\text{OH}/\cdot\text{O}^-$ in Aqueous Solution)," *Journal of Physical and Chemical Reference Data*, vol. 17, no. 2, pp. 513-886, 1988, doi: 10.1063/1.555805.
- [94] K. Sehested, J. Holcman, E. Bjergbakke, and E. J. Hart, "A pulse radiolytic study of the reaction hydroxyl + ozone in aqueous medium," *The Journal of Physical Chemistry*, vol. 88, no. 18, pp. 4144-4147, 1984/08/01 1984, doi: 10.1021/j150662a058.
- [95] K. Sehested, J. Holcman, and E. J. Hart, "Rate constants and products of the reactions of e⁻aq, dioxide(1-) (O₂⁻) and proton with ozone in aqueous solutions," *The Journal of Physical Chemistry*, vol. 87, no. 11, pp. 1951-1954, 1983/05/01 1983, doi: 10.1021/j100234a024.
- [96] S. Gordon, E. J. Hart, and J. K. Thomas, "The Ultraviolet Spectra of Transients Produced in the Radiolysis of Aqueous Solutions¹," *The Journal of Physical Chemistry*, vol. 68, no. 5, pp. 1262-1264, 1964/05/01 1964, doi: 10.1021/j100787a520.
- [97] J. K. Thomas, "THE RATE CONSTANTS FOR H ATOM REACTIONS IN AQUEOUS SOLUTIONS¹," *The Journal of Physical Chemistry*, vol. 67, no. 12, pp. 2593-2595, 1963/12/01 1963, doi: 10.1021/j100806a022.
- [98] A. J. Elliot, and Atomic Energy of Canada Ltd., Chalk River, ON (Canada). Chalk River Nuclear Labs., "Rate Constants and G-values for the Simulation of the Radiolysis of Light Water over the Range 0-300 Deg C," 1994.

- [99] B. H. J. Bielski, D. E. Cabelli, R. L. Arudi, and A. B. Ross, "Reactivity of HO₂/O⁻² Radicals in Aqueous Solution," *Journal of Physical and Chemical Reference Data*, vol. 14, no. 4, pp. 1041-1100, 1985, doi: 10.1063/1.555739.
- [100] G. V. Buxton, "Pulse radiolysis of aqueous solutions. Rate of reaction of OH with OH⁻," *Transactions of the Faraday Society*, vol. 66, pp. 1656-1660, 1970.
- [101] B. Hickel and K. Sehested, "Activation energies for the reactions oxide+ hydrogen and oxide+ deuterium in aqueous solution," *The Journal of Physical Chemistry*, vol. 95, no. 2, pp. 744-747, 1991.
- [102] C. Willis, A. W. Boyd, and O. A. Miller, "Primary yields and mechanism in the radiolysis of gaseous ammonia," *Canadian Journal of Chemistry*, vol. 47, no. 16, pp. 3007-3016, 1969, doi: 10.1139/v69-499.
- [103] R. Rives, D. Salavera, J. Campos, and A. Coronas, "Development of optical digital interferometry for visualizing and modelling the mass diffusion of ammonia in water in an absorption process," *Experimental Thermal and Fluid Science*, vol. 130, p. 110509, 2022/01/01/ 2022, doi: <https://doi.org/10.1016/j.expthermflusci.2021.110509>.
- [104] P. Vanýsek, "Ionic conductivity and diffusion at infinite dilution," *CRC handbook of chemistry and physics*, vol. 94, 1993.
- [105] M. Palomar-Pardavé, M. T. Ramírez, I. González, A. Serruya, and B. R. Scharifker, "Silver Electrocrystallization on Vitreous Carbon from Ammonium Hydroxide Solutions," *Journal of The Electrochemical Society*, vol. 143, no. 5, p. 1551, 1996/05/01 1996, doi: 10.1149/1.1836678.
- [106] D. Grujicic and B. Pesic, "Reaction and nucleation mechanisms of copper electrodeposition from ammoniacal solutions on vitreous carbon," *Electrochimica Acta*, vol. 50, no. 22, pp. 4426-4443, 2005/08/10/ 2005, doi: <https://doi.org/10.1016/j.electacta.2005.02.012>.